FACHBEREICH PHYSIK
BERGISCHE UNIVERSITÄT
GESAMTHOCHSCHULE WUPPERTAL

Production of π^+, K^+ and p in light and heavy quark hadronic Z decays

Dissertation
zur Erlangung des Doktorgrades des Fachbereichs Physik
der Bergischen Universität Wuppertal

Mario Reale

Bergische Universität - GHS Wuppertal

WUB-DIS 96-24
December 1996

Abstract

The differential production cross section for $\pi^{\pm}$, $K^{\pm}$ and $p\overline{p}$ have been measured in light (u,d,s) quark and heavy (b) quark Z decays into hadrons.
About 1.1 million $e^+e^- \rightarrow Z \rightarrow hadrons$ events, collected by the DELPHI experiment at CERN during 1994, have been used to study the inclusive hadronic production with respect to momentum, rapidity and the transverse momenta inside and outside the event plane.

The average particle multiplicity for $\pi^{\pm}$, $K^{\pm}$ and $p\overline{p}$ per hadronic event has been measured in light quark events to be $< n_{\pi^{\pm}} >_{uds} = 16.8 \pm 0.4$, $< n_{K^{\pm}} >_{uds} = 2.22 \pm 0.07$ and $< n_{p/\bar{p}} >_{uds} = 1.02 \pm 0.05$, and in heavy quark events to be $< n_{\pi^{\pm}} >_{b} = 18.2 \pm 0.5$, $< n_{K^{\pm}} >_{b} = 2.66 \pm 0.10$ and $< n_{p/\bar{p}} >_{b} = 0.87 \pm 0.10$.

The ξ_p^* values (maximum of the differential cross sections as a function of $\xi_p = \ln(1/x_p)$) were found to be $\xi_{\pi^{\pm}}^{*,uds} = 3.88 \pm 0.08$, $\xi_{K^{\pm}}^{*,uds} = 2.86 \pm 0.09$ and $\xi_{p\bar{p}}^{*,uds} = 2.77 \pm 0.09$ in light quark events and $\xi_{\pi^{\pm}}^{*,b} = 3.71 \pm 0.08$, $\xi_{K^{\pm}}^{*,b} = 2.54 \pm 0.16$ and $\xi_{p\bar{p}}^{*,b} = 2.95 \pm 0.16$ in b quark events.
This confirms, in both categories of events, a shift between the kaon and proton values, as it has been observed in the inclusive $Z \rightarrow q\overline{q} \rightarrow hadrons$ case (all quark flavors) ([66]). The results are in disagreement with the predictions of the local parton-hadron duality assumption in the modified leading logarithmic approximation about the subject of the observed ξ^* dependence on the hadron mass at $\sqrt{s} = M_Z = 91.19\ GeV$.

Charged particle identification has been performed using the energy loss measured by the DELPHI Time Projection Chamber and the Cherenkov angle measurement performed by the Ring Imaging Cherenkov Detector (RICH). The b quark tagging has been provided by the information coming from the DELPHI Microvertex Detector.

The results have been compared to three different Monte-Carlo generators, JETSET 7.4, HERWIG 5.8 C and ARIADNE 4.08 with the most recently available DELPHI tunings. HERWIG 5.8 C is not able to describe the measured proton spectra in both classes of events, being, especially in the high momentum region, non compatible with the data.
All the models forsee softer p_t^{out} spectra than the measured ones in both classes of events.

Grau, teurer Freund, ist alle Theorie und grün des Lebens goldner Baum (W.Goethe)

dedicato a Davide Sannino.

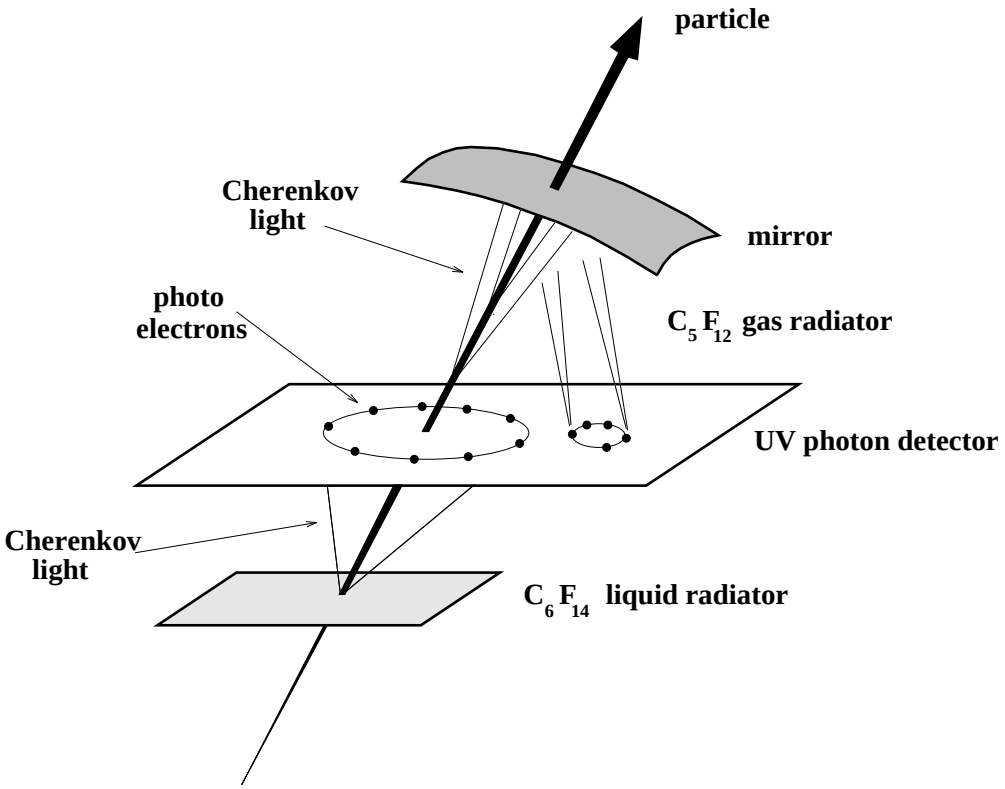

Für Sabine,
Professor Luciano Paoluzi,
Padre Luigi Canesso,
und Stefano Bernardini.

Contents

List of Tables

List of Figures

Chapter 1

Introduction

The Z gauge boson was discovered in 1983 at the SPS proton-antiproton collider of CERN. Its existence was foreseen 15 years before by the unified approach to electromagnetic and weak interactions, in the Glashow-Salam-Weinberg Theory.
Since then, four big experiments have been mounted at the Large Electron-Positron Collider of CERN, to produce Z bosons and study their decays.
A large amount of new experimental data has been collected in the years 1991-1995 by the four LEP collaborations.
During the past four years I had the opportunity to be involved in the experimental activity of a group of physicists from the University GHS Wuppertal at CERN, in the DELPHI collaboration.
My contribution was mainly concentrated on the study of the hadronic decays of the Z, to compare the experimental results to the existing predictions describing the processes of fragmentation: charged pion (π^+), kaon (K^+) and proton (p) productions were investigated in a heavy (b) and a light (u,d,s) quark enriched sample of events, giving experimental information on the meson and baryon production mechanism with respect to the original quark flavour.
This analysis refers to the data taken by the DELPHI collaboration in 1994, about 1.1 Million hadronic decays of the Z, from which b-tagged and light-quark tagged events have been selected.
The high performances of the Time Projection Chamber and the Ring Imaging Cherenkov Detector of DELPHI allowed particle identification on a wide momentum range, extended from 0.3 to 30 GeV/c, therefore providing a reliable extraction of pion, kaon and proton multiplicities in hadronic events.

1.1 Summary of this Thesis

In chapter two a general description of the theoretical mainframe today describing the fundamental forces and particles of nature, the so called "Standard Model", is given.

In chapter three the DELPHI Detector is described in detail, focusing on the characteristics of its subdetectors and on their general performances.

Chapter four describes the main detector used for this analysis : the Ring Imaging Cherenkov

detectors, who provided particle identification by means of the Cherenkov effect in two different radiators.

In chapter five the DELPHI Time Projection Chamber (TPC) is described. The TPC is the "tracking heart of DELPHI", reconstructing space points to provide the measurement of the position of the particle trajectories.
In this Work the information on the Specific Ionization (dE/dx) for charged tracks measured in the TPC has been used to perform particle identification.

In chapter six an overview of Particle Identification for Charged Hadrons in DELPHI is given. The main available algorithms to perform particle tagging based on the The Cherenkov Angle (θ_C) and the (dE/dx) information based main tagging programs are described.

Chapter seven is concerned by the method of the Analysis, the description of both the hadronic flavour tagging and the b quark flavour tagging programs. An overview of the particle identification tools performances is given, together with a general description of the b tag algorithm in DELPHI.

Chapter eight describes the results of my original contribution to the measurement of the inclusive hadronic content of Z decays in light quarks and b-quark tagged events, showing the momenta distribution for the identified hadrons in light and heavy quark events. It also reports the results of the fits to extract further experimental information from the measured distributions and the error analysis.

Chapter nine summarizes the Results and sketches the Conclusions of this work.

Chapter 2

Theoretical Mainframe

In this chapter the general theoretical mainframe behind the Standard Model of the fundamental strong and electroweak interactions is described.

2.1 Short Presentation of the Standard Model

By Standard Model we mean the most commonly accepted model describing the laws of physics at the very small scale of the subatomic world. At this scale the effects of gravity can be neglected with respect to the effects of the other three fundamental forces of nature, the electromagnetic, weak and strong forces. The Standard Model explains forces viewing them as the exchange of gauge bosons between fermions, the ultimate matter building blocks. Due to the substantially different nature of the interactions, the Standard Model is based on the electroweak interaction theory and on the theory of quarks and gluons dynamics, the so called QCD.

2.1.1 Electromagnetism and Weak Forces : The Electroweak Unification

The great progress of physics in the last decades has been the extension, in the theory of fields, of the gauge transformations concept from the classical electromagnetism to all kinds of fields in nature.
Gauge invariance is one of the most important properties of the electromagnetic field: it is well known that in this simple, very important case, transformations of the wave function ψ of an electron (charge $-e$) in an electromagnetic field ($\vec{A}$,Φ), like

$$\psi(x) \rightarrow \psi(x)' = e^{ie\alpha(x)}\psi(x) \qquad x = (\vec{x}, t) \tag{2.1}$$

leave the wave equation unchanged of the electron, as a consequence of the gauge transformation

$$\vec{A} \rightarrow \vec{A}'(x) = \vec{A} + \frac{1}{e}g\vec{r}ad(\alpha) \qquad \Phi \rightarrow \Phi' = \Phi + \frac{1}{e}\frac{\partial\alpha}{\partial t} \tag{2.2}$$

Phase transformation like eq. 2.1 form an abelian group U_1 of 1×1 unitary matrices; the physical interpretation of this mathematical property of the field is that it is possible to describe charged particles in space-time by wavefunctions with arbitrary phases only if charges are coupled to a (long range) field.
In 1954 Yang and Mills [1] proposed that the gauge theory of the electromagnetic field could be generalized to non abelian groups and, as matter of fact, they chose the SU_2 group of isospin.
Their starting point was that isospin invariance in strong interactions implies its invariance under isospin rotation

$$\psi \rightarrow \psi' = e^{ig\vec{\tau}\cdot\vec{\Lambda}}\psi \tag{2.3}$$

together with the request that the rotation axis vector, $\vec{\Lambda}$, in the isospin space could be chosen arbitrarily at different $x = (\vec{x}, t)$. Here $\vec{\tau}$ are the Pauli matrices, g is a constant.
Unfortunately the corresponding gauge field was a massless isovector field (just like the photon), so that the isospin symmetry did not give a correct result because no massless charged particle exists in nature.
Further attempts in this direction were done by Glashow [2] and Salam and Ward [3]. In the years 1967-68 Weinberg and Salam [4] proposed a (renormalizable) gauge theory based on the SU_2 group of a *weak isospin* and U_1 group of a *weak hypercharge* Y.
This was the famous W-S standard gauge theory unifying weak and electromagnetic interactions

$$(SU_2)_L \otimes U_1 \tag{2.4}$$

The main ideas underlying in the W-S theory were that :

- a) only left handed fermions (and their right handed antiparticles) all undergo weak interactions.
- b) they appear in definite pairings in the currents.

These remarks make plausible that the relevant symmetry underlying the weak force must be given by $(SU_2)_L \otimes U_1$, where left handed fermions form doublets and right handed form singlets.
To give a mass to the gauge bosons (as suggested by the point contact Fermi weak interaction observed at low energy) they recurred to the so called *Higgs mechanism*, which requires *spontaneous symmetry breaking*, saving anyway the renormalizability of the theory.
Spontaneous breaking of a symmetry occurs when the Lagrangian contains a symmetry which is not more present in the lowest energy state of the system. Goldstone has proven that the spontaneous breaking of a global symmetry is always associated with massless scalar particles, the so called *Goldstone bosons* [5].
Higgs [6] made the important theoretical discovery that, only for gauge field theories, gauge bosons and scalar bosons mix together to generate massive vector bosons.
In other words, the initial massless weak gauge bosons have only two helicity states like the

photon, but through the Higgs mechanism they acquire a zero helicity state and a mass, *absorbing a Golstone boson.*
The fundamental vector bosons are a massless isovector triplet W^+,W^-, W^0 from gauging SU_2 and a massless isosinglet neutral boson B^0 from U_1; eventually, by the effect of the Higgs mechanism, we are left with a set of three massive field mesons

$$W^+, W^-, \quad Z = W^0 cos(\theta_W) - B^0 sin(\theta_W) \qquad (2.5)$$

and a massless photon

$$A = W^0 sin(\theta_W) + B^0 cos(\theta_W) \qquad (2.6)$$

The WS theory foresees different coupling strengths for $W^\pm$ bosons to fermions (they couple exclusively to left handed fermions and right handed anti fermions) and for the Z boson to fermions (field bosons can also couple together at three or four boson vertices). The results for the two (vector and axial) couplings of the Z boson is given by

$$v_f = \frac{T_3^f \ - 2Q_f \ sin^2(\theta_W)}{2 \ sin(\theta_W) \ cos(\theta_W)} \qquad (2.7)$$

$$a_f = \frac{T_3^f}{2 \ sin(\theta_W) \ cos(\theta_W)} \qquad (2.8)$$

where θ_W is the Weinberg angle (weak mixing angle), and T_3^f ,Y the third component of the weak isotopic spin and weak charge respectively : (Q^f is the fermion electric charge divided by e)

$$Q = T_3^f + \frac{Y}{2} \qquad (2.9)$$

The W-S theory makes many predictions in terms of the single parameter θ_W.
One prediction was the existence of a weak neutral current, observed experimentally in 1973 [7];
the second very important prediction was the existence of the massive $W^\pm$ and Z bosons, found in 1983. [22].

2.1.2 Quantum Chromodynamics

In 1964 the quark model proposed by Gell-Mann ([9]) and Zweig ([10]) suggested that all baryons and mesons (which at that time were already amounting to hundreds particles and antiparticles) could be made by (3 flavors at that time) spin 1/2 substructures, u, d and s quarks. In particular, in the arrangement corresponding to

$$mesons = (q\overline{q}), \qquad baryons = (qqq) \qquad (2.10)$$

the quark quantum numbers could be properly combined to give spin, charge, strong isospin, baryon number, strangeness of all known particles, then arranged in meson and baryon

multiplets of different angular momenta and parities.
From the point of view of Lie Groups theory it was suggested that the three quarks (and the 3 antiquarks) were to be considered as the 3 state base vectors of two inequivalent fundamental representations 3 (and $\overline{3}$) of SU_3 group of transformations (9-1=8 generators, with typical triangular weight diagrams);
In the meanwhile ([11]) deep inelastic lepton-nucleon scattering experiments at SLAC and CERN had shown that a nucleon contains point-like constituents (as evidenced by the scale invariance of the structure functions) with spin 1/2 (partons) [14], and that e-m and weak cross sections are compatible with the fractional charge of quarks : the identification of quarks and partons was immediate.
Several other quark flavors were discovered in the last years and now we know up to 6 quark flavors; (u, d, s, c, t, b) many of them were expected for theoretical reasons.
Already in 1965 it was recognized that in the quark model of hadrons and in lepton-quark interactions a new quantum number was needed, the *colour* charge, as an extra degree of freedom for quarks : three values of colour charge, say red, green and blue for each quark, so that each quark occurs in three different states.
The existence of colour was postulated by Han and Nambu [13] in 1965. They assumed all hadrons to be colour singlets, therefore overcoming the problem of existence of baryons with a total symmetric wavefunction (according to the originary quark model), like the observed $\Delta^{++}(uuu)$ or the $\Omega^{-}(sss)$ who seemed to clash with the Pauli exclusion principle for fermions and the spin-statistic ansatz.
The introduction of colour antisymmetrized correctly the wavefunctions of these fermions ([15]) and increasead by a factor 3 the expected e^+e^- to hadrons cross section making it compatible with the experimental results ([16])) at PETRA.
Quantum Chromodynamics (QCD) is at this stage a gauge theory of the strong interaction among quarks; the theory responsible for the quark and gluons colour (strong) interaction dynamics, one of the components of the $SU_3 \otimes SU_2 \otimes U_1$ Standard Model.
The interaction is assumed to be invariant under colour interchange, i.e. under rotations in colour space with three colour base states (for each quark), so that it is described by a local SU_3^{col} symmetry group.
The complete QCD Lagrangian is composed by different terms, corresponding to the different couplings : the free quarks term, the quark-gluon coupling, the gluon self-interaction term (which includes the gluon field kinetic energy term).

$$\mathcal{L}_{QCD} = -\frac{1}{4} G^{(a)}_{\mu\nu} G^{(a)\ \mu\nu} + i \sum_q \overline{\psi^i_q} \gamma^\mu (D_\mu)_{ij} \psi^i_q - \sum_q m_q \overline{\psi^i_q} \psi_{qi} \tag{2.11}$$

Here the various terms include the Lorentz indices (μ, ν..) and the colour indices (a, b..)
In this formula the Field tensor is given by

$$G^a_{\mu\nu} \equiv \partial_\mu A^a_\nu - \partial_\nu A^a_\mu + g_s f_{abc} A^b_\mu A^c_\nu \tag{2.12}$$

and the covariant SU_3 derivative is defined as

$$(D_\mu)_{i,j} = \delta_{ij} \partial_\mu - i g_s \sum_a \frac{\lambda^a_{i,j}}{2} A^a_\mu \tag{2.13}$$

In these formulae g_s is the QCD coupling constant ($\alpha_s = g_s^2/4\pi$), f_{abc} are the SU_3 group structure constants, whereas the λ_i are the SU_3 group generators. While acting on a representation of dimension 3, they are represented by the well known 8 traceless Gell-Mann matrices.

The SU_3 generators obey the following commutation and anticommutation relations :

$$[\lambda_a, \lambda_b] \equiv \lambda_a\lambda_b - \lambda_b\lambda_a = 2if_{abc}\lambda_c \tag{2.14}$$

$$\{\lambda_a, \lambda_b\} \equiv \lambda_a\lambda_b + \lambda_b\lambda_a = \frac{4}{3}\delta_{ab}I + 2d_{abc}\lambda_c \tag{2.15}$$

The f_{abc} are odd under permutation of any pair of indices, while the d_{abc} are even ([18]) . I is the identity 3×3 matrix. The $\psi_q^i(x)$ are the 4-components Dirac spinors associated to each quark field of the 3 colours (i) and flavour (q). Quarks belong to the (3) triplet representation of SU_3^{col}, antiquarks to the $(\overline{3})$.
The gauge bosons (gluons), mediating the q-q interaction, belong to an octet representation of SU_3^{col}.
In Quantum Electro Dynamics (QED) we have only two source charges and an uncharged photon exchanged between the two, but in QCD, while observable particles are colorless, we have 6 types of charges (3 colours r,g,b and 3 anticolors, $\overline{r}$, $\overline{g}$, $\overline{b}$) for the source particles, i.e.quarks, and $9 - 1 = 8$ colour charged gluons (8 colour-anticolor $r\overline{r}$,$r\overline{g}$, $r\overline{b}$ .... states) as mediating vector bosons.
These conclusions are based by imposing invariance of the Dirac equation for quarks under infinitesimal local transformation, with a value g_s for the colour charge. From the gauge invariance it can be deduced that gluons are massless, and because gluon field energy density contains cubic and quartic terms in the field, three or four gluons can interact at a point x. Gluons interact with quarks but also with each other.

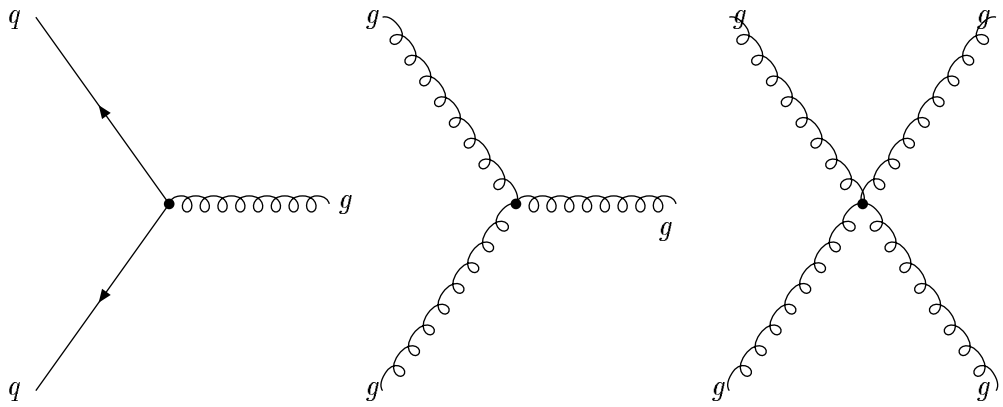

Figure 2.1: *Fundamental QCD couplings*

The three fundamental QCD couplings are shown in picture 2.1. Despite the well defined form of the QCD Lagrangian and the understanding of the origin of its different terms we have at our disposal today (which could remind us of QED), still to derive exact and precise physical

predictions for observable quantities is however a very hard task because of the peculiarities of the strong interactions. Some of them are explained in the next section.

2.1.3 The QCD running coupling constant

In principle, having at our disposal a theory for the strong interactions, by applying a set of rules similar to those for Feynman diagrams in QED, it could seem that one could get the amplitude of any process involving quarks.
In QCD, however, we are faced with many difficulties : at low energy the coupling constant g_s must be much larger than the electromagnetic constant (quarks are bound in nucleons and hadronic cross sections are much higher than the e.-m. ones) while, as we know, at very high momentum transfer they behave like free partons.
Politzer [17] and Gross and Wilczek [19] have proved that at very large momentum transfer, i.e. ,at small distances, the coupling constant strength g_s goes to zero (*asymptotic freedom*); this result related to the colour polarization of the vacuum, is similar (but not identical) to the QED problem of absorbing the divergent contribution of loop diagrams by the renormalizing of the coupling constant.
In QCD the renormalized effective coupling constant has a dependence on the four momentum transfer Q governed by the β function :

$$\mu\frac{\partial\alpha_s}{\partial\mu} = -\frac{\beta_0}{2\pi}\alpha_s^2 - \frac{\beta_1}{4\pi^2}\alpha_s^3 - \frac{\beta_2}{64\pi^3}\alpha_s^4 - .... \tag{2.16}$$

where the β coefficients are given by

$$\begin{aligned}\beta_0 &= 11 - \frac{2}{3}N_f \\ \beta_1 &= 51 - \frac{19}{3}N_f \\ \beta_2 &= 2857 - \frac{5033}{9}N_f + \frac{325}{27}N_f^2\end{aligned} \tag{2.17}$$

At the lowest order in α_s the scaling law is of the type

$$\alpha_s(Q^2) = \frac{\alpha_s(\mu^2)}{1 + B\alpha_s(\mu^2)\ ln(\frac{|Q^2|}{\mu^2})} \tag{2.18}$$

where

$$B = \frac{\beta_0}{4\pi} = \frac{(11 - 2N_f/3)}{4\pi} \tag{2.19}$$

where N_f is the number of flavors and μ is a reference momentum (energy) scale. For $N_f = 6$

$$\alpha_s(Q^2) \to 0 \qquad as \quad Q^2 \to \infty \tag{2.20}$$

which corresponds to QCD property of *asymptotic freedom.*
To avoid the arbitrarity of the energy scale μ expressed by the transformation

$$\frac{1}{\alpha_s(\mu^2)} = \frac{1}{\alpha_s(\mu'^2)} + \ ln(\frac{\mu'^2}{\mu^2}) \tag{2.21}$$

it is convenient to introduce a dimensional parameter Λ, defined as

$$ln(\Lambda^2) = ln(\mu^2) - \frac{4\pi}{\beta_0 \ \alpha_s(\mu^2)} \tag{2.22}$$

able to fix the α_s dependence on Q^2 as

$$\alpha_s(Q^2) = \frac{4\pi}{\beta_0 \ ln(\frac{Q^2}{\Lambda^2})} \tag{2.23}$$

At the next order in the expansion, the correct expression for α_s is given, in the so called *Modified Minimal Subtraction* ($\overline{MS}$) renormalization scheme, by the expression

$$\alpha_s(Q^2) = \frac{12\pi}{(33-2N_f)\ln(\frac{Q^2}{\Lambda^2_{\overline{MS}}})}\left(1 - 6\frac{153-19N_f}{(33-2N_f)^2}\frac{\ln(\ln(\frac{Q^2}{\Lambda^2_{\overline{MS}}}))}{\ln(\frac{Q^2}{\Lambda^2_{\overline{MS}}})} + \mathcal{O}(\alpha_s^3)\right). \tag{2.24}$$

The parameter Λ, at a finite order calculation, depends on the given renormalization scheme, but any dependence of the physical observables on the renormalization scheme and on the reference energy scale μ has to vanish if all orders would be taken into account.

First evidence for the existence of gluons came in 1979 from the observation of three jets events in e^+e^- collisions experiments by Brandelik, Barber and Berger ([20]) in the process

$$e^+e^- \to q\overline{q}, \qquad q \ (\ or\ \overline{q}) \to q \ (\ or\ \overline{q}) + g \tag{2.25}$$

In first approximation in the perturbative expansion, the ratio
$(N.3\ jet\ events)/(N.2\ jet\ events)$ is proportional to α_s.
Additional evidence came at SPS $p\overline{p}$-collider in 1982-83 from experiments by Banner et al.([21]) and Arnison et al.([22]), who detected collimated jets of hadrons clearly emerging from parton-parton scattering at very large momentum transfer when, as it is expected, the coupling constant becomes small and single gluon exchange between partons is dominant. This was confirmed by the centre of mass angular observed particle distribution.

It is worthwhile to observe that one could rewrite, at the lowest order in α_s

$$\alpha_s = \frac{1}{B \ \ ln(\frac{q^2}{\Lambda^2})}, \qquad \Lambda^2 = \mu^2 e^{-\frac{1}{B\alpha_s(\mu^2)}} \tag{2.26}$$

Inserting the measured value of α_s one gets

$$\Lambda \simeq 200 \quad MeV \tag{2.27}$$

This value gives the scale of strong interactions: because the masses of u and d quarks are m_u,$m_d << \Lambda$,while $m_s \simeq \Lambda$, m_c, $m_b >> \Lambda$, only after these consideration one can deeply understand the origin of the strong isotopic spin SU_2 symmetry and why the old SU_3 symmetry is not an exact symmetry.

2.2 The Standard Model : Summary

The theory of elementary particles that we have summarized up to now, is known as the *Standard Model*; as we have seen it is based on the requirements that physics is invariant under local gauge transformations of the direct product

$$(SU_3)^{col} \otimes (SU_2)_L \otimes (U_1) \tag{2.28}$$

In the frame of the Standard Model all general properties of forces could be summarized in 2.1.

Of course many problems are still present at this stage of the model: apart from some fundamental questions which are still unsolved (as for instance, why there exist three families of leptons and quarks, why nature seems to be left handed) in the minimal Standard Model there are too many parameters, at least 18 independent free parameters:

- For fermions we have to specify 6 quark masses, 3 lepton masses, 4 angles in the quark CKM mixing matrix ;
- For bosons, 2 coupling constants α_{em} and α_s, the Z mass, the Weinberg electroweak mixing angle and the Higgs boson mass.

Many ways are considered to go beyond the SM, like Grand Unification Theories and Supersymmetries which, to our purposes, we can still consider here as *work in progress* from the theoretical point of view.

2.3 Current description of hadronic Z decays

Given the consideration above about the theory of strong and electroweak interactions, the current common picture of the Z annihilation into hadrons (representing $\simeq$ 70 % of the total

Fermions	NC	I	I_3	Y	Q
$\begin{pmatrix}\nu_e\\ e\end{pmatrix}_L$ $\begin{pmatrix}\nu_\mu\\ \mu\end{pmatrix}_L$ $\begin{pmatrix}\nu_\tau\\ \tau\end{pmatrix}_L$	0	1/2	$+1/2$ $-1/2$	-1	0 -1
$\begin{pmatrix}u\\ d\end{pmatrix}_L$ $\begin{pmatrix}c\\ s\end{pmatrix}_L$ $\begin{pmatrix}t\\ b\end{pmatrix}_L$	3	1/2	$+1/2$ $-1/2$	$+1/3$	$+2/3$ $-1/3$
e_R μ_R τ_R	0	0	0	-2	-1
u_R c_R t_R	3	0	0	$+4/3$	$+2/3$
d_R s_R b_R	3	0	0	$-2/3$	$-1/3$
Gauge Bosons					
$Gluons$	8	0	0	0	0
W^+	0	1	$+1$	0	$+1$
W^-	0	1	-1	0	-1
Z	0	1	0	0	0
γ	0	0	0	0	0
Higgs Bosons					
$\begin{pmatrix}\phi^+\\ \phi^0\end{pmatrix}$	0	1/2	$+1/2$ $-1/2$	$+1$	$+1$ 0

NC : Number of Colours I : Weak Isospin

Y : Weak Hypercharge Q : electric charge

Table 2.1: *Elementary Particles and corresponding quantum numbers*

number of Z decays) is split into three different phases :

- The Z decays into a primary quark pair. The Standard Electroweak Theory makes exact predictions on the decay amplitude and calculations have been already performed up to a 1% uncertainty precision level. (due to the top quark mass)
- The originally produced quark pair radiates gluons, who can subsequently decay into a quark pair, giving rise to the so-called parton shower process. It is generally believed that Perturbative QCD can describe this phase, given the fact that the Q^2 of the system is high enough so that α_s is small enough to allow the use of Perturbation Theory.
- The coloured radiated partons do cluster themselves in groups of two and three to form colorless mesons and hadrons, detected by the experimental apparatus.

The two last process together represent the so called *Hadronization Process* : the whole matter transition from two originally radiated quarks to (on average) about 40 hadronic final states.

The most unknown part of this process is the last phase, the so called *Fragmentation process*, lasting for a time of the order of 10^{-24}-10^{-25} s (a typical strong interaction time) and energy available to the partonic system to the original 45 GeV per quark to the final kinematical spectrum of the detected hadrons.

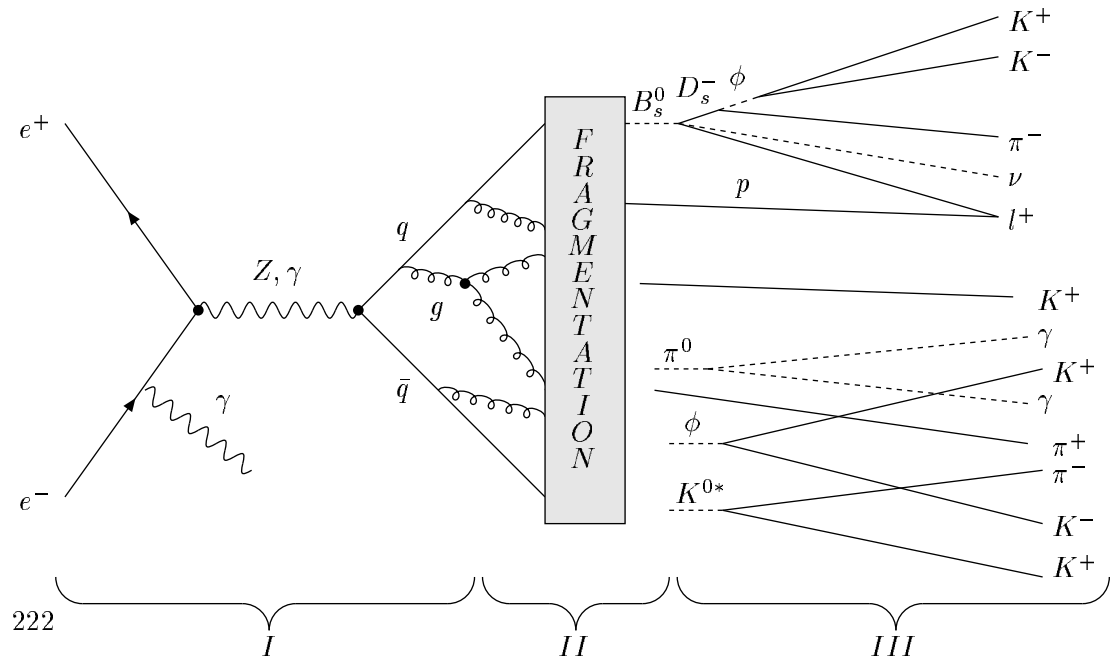

Figure 2.2: *The fragmentation in the Z decay and its three different regions: the production of $q\overline{q}$, the hadronization and the decay of the formed particles accompanied by the primary produced stable hadrons*

Hadronization is split therefore in a first perturbative part in which the Q^2 of the partonic system is high enough to allow the use of Perturbative QCD and in a second part, the most unknown one, the proper fragmentation phase, in which the radiated partons cluster themselves into colorless hadrons.
The approach to the description of the perturbative phase of the hadronization process is usually represented either by the Matrix Element (ME) Method either by the Parton Shower Method (PS).
The fragmentation phase is commonly described by the most common models available, the String and Cluster fragmentation models.
In the following sections first the Perturbative phase approaches are described and then the proper fragmentation models.
For what concerns the primary process $e^+e^- \to q\overline{q}$, at the lowest order (Born level), neglecting the quark masses, the total cross section is given by [24] :

$$\sigma(e^+e^- \to q\overline{q}) = N_c \cdot \frac{4\pi}{3} \cdot \frac{\alpha^2}{s} \left(\quad Q_e^2 Q_q^2 + \frac{1}{16}(V_e^2 + A_e^2)(V_q^2 + A_q^2) \cdot |\chi|^2 + -\frac{1}{2}\, Q_e Q_q V_e V_q \cdot Re(\chi) \quad \right) \tag{2.29}$$

where χ is the ratio of the Z to the γ propagators and is given by

$$\chi = \frac{1}{4sin^2\theta_W \cdot cos^2\theta_W} \cdot \frac{s}{s - M_Z^2 + iM_Z\Gamma_Z} \tag{2.30}$$

In this formula 2.29 the first term describes the photon exchange, the second the Z exchange and the third term the interference between the two.
V_f and A_f are the vector and axial couplings between the fermions and the Z boson, α is here the e.m. fine structure constant, Q_e the electron charge, Q_q the quark charge. This equation describes the Breit-Wigner shape of the Z resonance.
The angular behaviour of the cross section for unpolarized electron-antielectron annihilation (neglecting the interference terms) as a function of the polar angle θ between the incoming electrons and outgoing quarks direction is in good approximation given by

$$\frac{d\sigma}{dcos\theta} \sim 1 + cos^2\theta \tag{2.31}$$

2.3.1 Matrix Element Model

This approach uses the available Matrix Element of QCD calculation in the perturbative expansion for α_S order $o(\alpha_S^2)$. Until today calculations have been performed up to the second order only. Therefore only four partons are foreseen at the end of the cascade. The ME method is in principle the most correct one, from the mathematical point of view. Picture 2.3 shows some of the first and second order QCD corrections for the process $e^+e^- \rightarrow q\overline{q}$, as implemented in the Matrix Element approach.

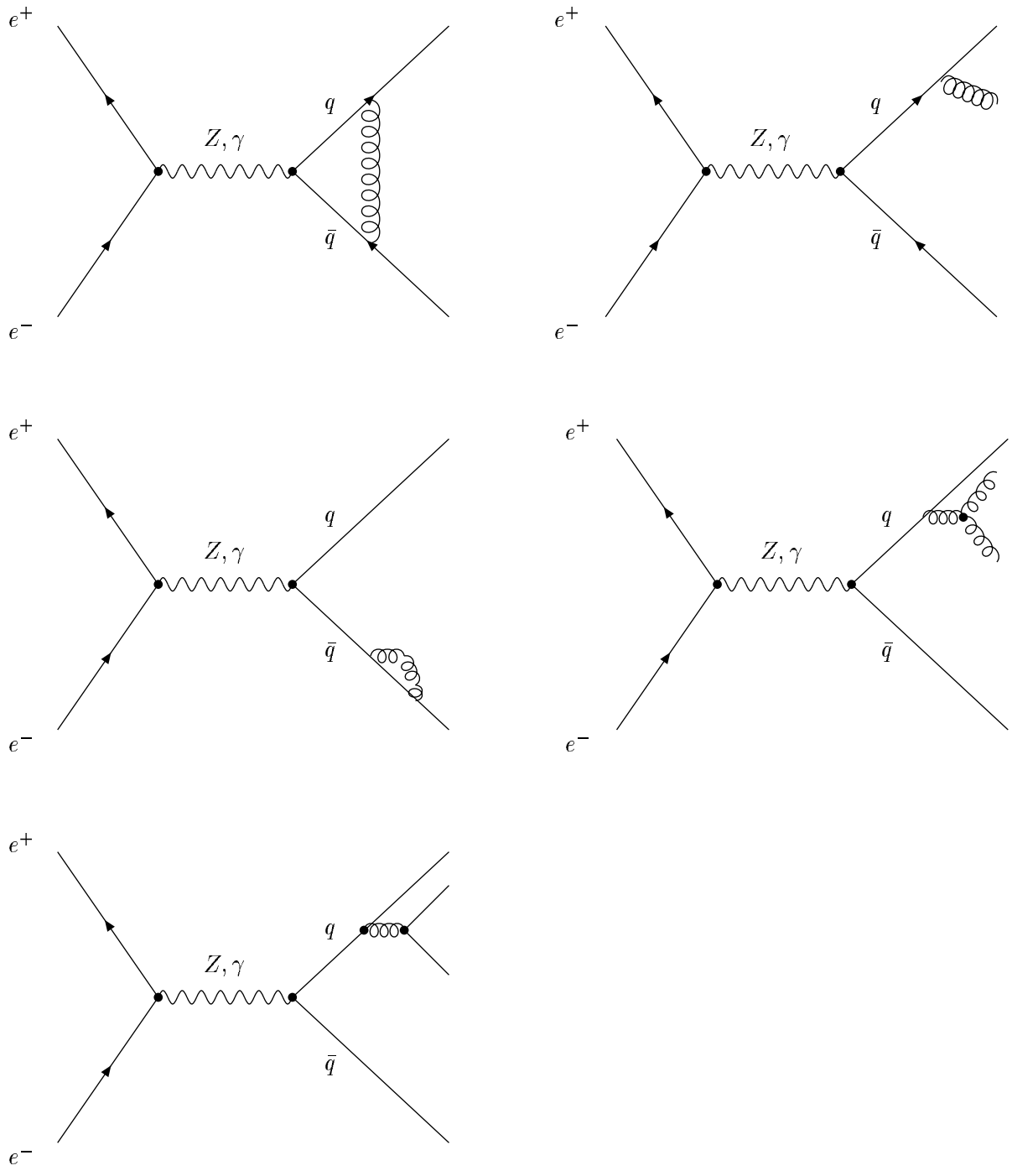

Figure 2.3: *Matrix Elements leading order diagrams contributing to the hadronic production*

The first order corrections to the Born level cross sections represent the main contribution to the three jets events rates, through the emission of a hard gluon. In first order the differential cross sections for 3 jets events for massless quarks is given by the expression

$$\frac{1}{\sigma_{tot}}\frac{d\sigma}{dx_q dx_{\overline{q}}} = \frac{2\alpha_s}{3\pi}\frac{x_q^2 + x_{\overline{q}}^2}{(1-x_q)(1-x_{\overline{q}})} \tag{2.32}$$

where x_q, $x_{\overline{q}}$ and $x_g = 2 - x_q - x_{\overline{q}}$ are the quark, antiquark and gluon energies normalized to the beam energy and Λ is the QCD scale corresponding to 5 flavors ($N_f = 5$) :

$$\alpha_S(Q^2) = \frac{12\pi}{(33 - N_f)\ ln(\frac{Q^2}{\Lambda^2})} \tag{2.33}$$

here $Q^2 = s = E_{cm}^2$.

2.3.2 Parton Shower Model

In the Parton Shower (PS) approach the four fundamental partonic splittings $g \rightarrow q\overline{q}$, $g \rightarrow gg$, $q \rightarrow qg$ and $q \rightarrow q\gamma$ are used iteratively to describe the first (perturbative) part of Hadronization, in a partonic cascade scheme.
In the PS Model perturbative QCD is used usually in the mainframe of the *Leading Logarithm Approximation* (LLA) [26], which allows to reproduce the soft structure of jets better than what does the Matrix Element approach do.
In LLA Perturbative calculation of QCD diagrams, the leading logarithmic terms
$\alpha_s^n(Q^2) log^n(Q^2/\Lambda^2)$ are summed to all orders of n.
The production of partons is described as a Markovian chain of successive branching of off-shell partons. In the LLA scheme it is possible to handle the partonic branchings as classical probabilities, neglecting the interference terms [12] among gluons. Therefore the Leading Log approximation provides a useful way to handle Perturbative QCD calculation for specific processes down to scales of the order of $\simeq \Lambda_{QCD}$.
The Altarelli-Parisi equations [31] describe the probability for each fundamental splitting to occur, according to the fraction of initial (mother (a)) parton momentum carried by the two final (daughters (b,c)) partons (respectively z and $(1-z)$) :

$$\frac{dP_{a\rightarrow bc}}{d\tau} = \int dz \frac{\alpha_s(Q^2)}{2\pi} P_{a\rightarrow bc}(z)$$

(2.34)

where τ is defined as $\tau = ln(Q^2/\Lambda^2)$ These equations are integro-differential equations for the partonic density and they describe the evolution of the splitting functions $P_{a\rightarrow bc}$ as a function of the Q^2.
The Splitting functions $P(z)$, giving the probability for each splitting, are given by

$$P_{g\to gg}(z) = N_c^f \frac{(1 - z(1 - z))^2}{z(1 - z)}$$

$$P_{q\to qg}(z) = C_F \frac{1 + z^2}{1 - z}$$

(2.36)

$$P_{g\to q\bar{q}}(z) = T_f(z^2 + (1 - z)^2)$$

$$P_{q\to q\gamma(z)} = e_q^2 \frac{(1 + z^2)}{(1 - z)}$$

(2.38)

(2.39)

Here $C_F = 4/3$ and $N_c^f = 3$ are colour factors, T_f is defined by $T_f = N_f/2$.

In figure 2.4 the sketch of a typical parton shower development is shown.
The model foresees a cut off (Q_0) in the Parton invariant mass, above which the elementary splittings take place.
Effective masses are calculated according to a given cut off Q_0 for quarks and gluons.

$$m_{eff,g} = \frac{1}{2}Q_0 \tag{2.40}$$

$$m_{eff,q} = \sqrt{m_q^2 + \frac{1}{4}Q_0^2} \tag{2.41}$$

This expedient to handle the partonic evolution in a shower has his correspondent analogous in the theory of the QCD Deep Inelastic Scattering, in which the $log(Q^2)$ dependence term in the quark density distribution $q(x)$ sonded by a probe photon in a nucleon is reabsorbed in the Q^2 dependence for the quark density itself : $q = q(x, Q^2)$ (where $y \cdot p$ is the initial momentum of the quark and $z \cdot (y \cdot p)$ its final one ($z = x/y$)). This is analogous to say that the structure functions for the partons inside the nucleons depend on both the scattering variable ν and Q^2 characterizing the structure functions behaviors and no longer only on their

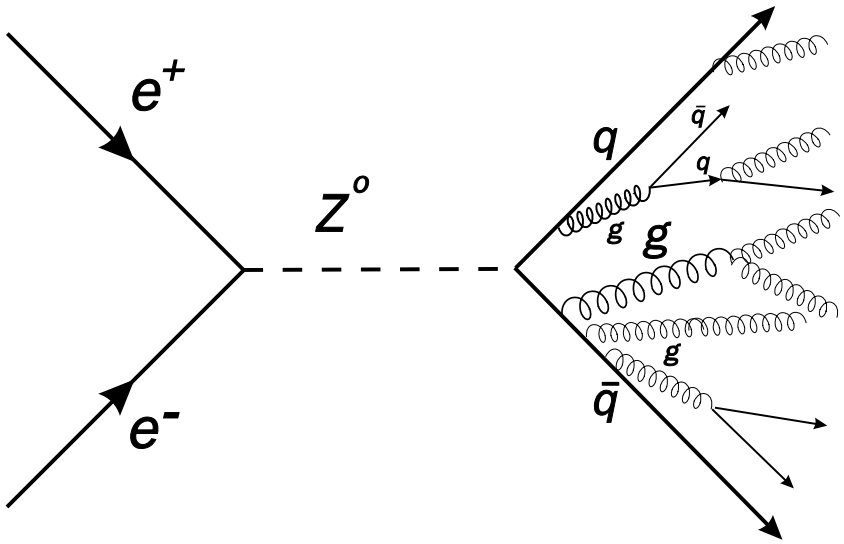

Figure 2.4: *Sketch of a typical Parton Shower development.*

ratio.
In this scheme the Altarelli-Parisi equation are integro-differential evolution equations for the partonic density writable like

$$\frac{d\ q(x,Q^2)}{d\ (logQ^2)} = \frac{\alpha_s}{2\pi}\int_x^1 \frac{dy}{y} q(y,Q^2)\ P_{qq}(\frac{x}{y}) \tag{2.42}$$

where P_{qq} denotes one of the possible splittings above.
The elementary splittings are interrupted corresponding to the smallest effective mass, defined as the sum of the lightest possible partonic daughters in the parton shower.
The time evolution of the cascade is essentially determined by the value of the available four momentum squared of the system, Q^2. In the Monte Carlo generators Q^2 is calculated in many ways : JETSET uses $Q^2 = m_a^2$ (the squared mass of the mother parton).
The evolution of the partonic shower is therefore ruled by the four splitting functions P_{qq}. Their physical meaning and the consequences on the event jet rates are clear if one writes the variation on the partonic density in the form

$$q(x,Q^2) + dq(x,Q^2) = \int_0^1 dy \int_0^1 dz\ q(y,Q^2)\mathcal{P}_{qq}(z,Q^2)\delta(x-zy) \tag{2.43}$$

where

$$\mathcal{P}_{qq}(z,Q^2) \equiv \delta(1-z)\ +\ \frac{\alpha_s}{2\pi}P_{qq}(z)\ log(\frac{Q^2}{\mu^2}) \tag{2.44}$$

It is therefore natural to interpret $\mathcal{P}_{qq}(z)$ as the probability density to find a quark in the showering inside a quark with fraction z of the parent quark momentum, to first order in α_s. The term $\delta(1-z)$ corresponds to there being no change in $q(x,Q^2)$, and this probability for

a quark to remain unchanged is then reduced when the $o(\alpha)$ contributions are included.
In the zero-order approximation the partonic emission in the showers is isotropycal with respect to the initial parton direction. This fact is responsible for the underestimation of the three jets rates provided by the Parton Shower models. The three jet rates is increased by the so called $o(\alpha_s)$-*matching*, provided by the second term in equation 2.44.
In pure leading-log showers it is possible that successive partonic branching provide the emission of partons at higher angles w.r.t.the initial opening angle of the initial ones. In reality, due to destructive negative interference effects this is not the case, due to Quantum Mechanics. Therefore to handle the calculation the opening angles in the showering are angularly ordered so that the latest angles are always smaller than the initial ones in the chain. This procedure is called *angular ordering* and Parton Showers models working in this way are referred to as to *Coherent Leading Log approximation* programs.

2.4 Fragmentation Models

In this section a general overview of the existing fragmentation models is given, starting from the String Model, going through the Cluster Model to end with another, more theoretically based approach to fragmentation, that is, the Modified Leading Logarithm Approximation in the mainframe of the so called *Local Parton-Hadron Duality* assumption.
The fragmentation models try to explain the way in which the partons at the end of the perturbative cascade cluster themselves into colorless hadrons. Since the individual partons cannot be identified, experimentalists can only measure the inclusive *fragmentation functions* matching a given partonic flavour with a given hadronic observable particle. This means - in other words - that we are not able experimentally to bypass the property of confinement : we can observe only colour-singlet hadrons. It is therefore also for the fragmentation models necessary to postulate possible fragmentation functions, that is, functions giving the probability for a given parton to produce a given hadron, as a function of the fraction of momentum (or energy) transfer z from parton to hadron.
In the framework of the fragmentation function ($D_k^h(z,\mu^2)$) model one expresses the particle spectrum $\mathcal{F}^h(x,s)$ of hadron h at a given CM energy $\sqrt{s}$ like

$$\mathcal{F}^{\langle}(x,s) \equiv \frac{1}{\sigma_{tot}}\frac{d\sigma}{dx}(e^+e^- \to hX) = \sum_k \int_x^1 \frac{dy}{y} C_k(s,y,\alpha_s(\mu^2)) D_k^h(\frac{x}{y},\mu^2) \tag{2.45}$$

where σ_{tot} is the total hadronic cross section $(e^+e^- \to X)$, $x = 2E_h/\sqrt{s}$ is the normalized (scaled) energy of the hadron h, k stands for the initial parton of flavour k, whose scaled energy is $y = 2E_k/\sqrt{s}$, $z = x/y$ and $C_k(s,y,\alpha_s(\mu^2))$ is the so called *coefficient function* underlying the production of parton k.
The most commonly used empirical inclusive fragmentation functions $f(z)$ are such that the hadronic flavour determination is often decoupled by the fragmentation process itself :

$$D_k^h(z,\mu^2) \simeq f(z,\mu^2) \tag{2.46}$$

leaving the quark flavour determination (and therefore the ultimate hadronic flavour of the resulting hadron) to some modelling for the relative quark flavour generation probabilities.
In the most common fragmentation models (like for example the string model described in

the next section) the whole hadronization process is an iterative process in which the originary quark q (or quark jet) is splitted (by the creation of a new $q'\overline{q'}$ pair) into two jets given by $q\overline{q}'$ and $q'\overline{q}''$ and so on. In this process the fragmentation functions play the fundamental role of probability distribution for the fraction of longitudinal momentum carried at each splitting by the generated quarks.
The fragmentation functions therefore rule the whole hadronization process and their form and behaviour cannot be foreseen by Perturbative QCD.
Many different fragmentation functions $f(z)$ have been proposed [28]:

- The Field-Feynman parameterization

$$f(z) = 1 \; - \; a \; + \; 3a \; (1-z)^2 \qquad\qquad a = 0.77 \tag{2.47}$$

- A less peaked function at z=0 commonly used is

$$f(z) = (1 \; + \; c) \; (1-z)^c \tag{2.48}$$

  where the parameter c has to be tuned to fit the data.

- To describe appropriately heavy flavour hadronic production in hard processes, usually the Peterson [29] fragmentation function is used

$$f(z) \propto (z(1 - \frac{1}{z} - \frac{\epsilon_Q}{1-z})^2)^{-1} \tag{2.49}$$

  where ϵ_Q is a free parameter, expected to scale between flavors like $\epsilon_Q \propto 1/m_Q^2$.

Normally the relative quark flavour production is chosen randomly according to the relative probabilities $u\overline{u} : d\overline{d} : s\overline{s} = 1 : 1 : \gamma_s$, with typically $\gamma_s = 0.3$.

2.4.1 The String Model and the JETSET MonteCarlo Program

The String Model was conceived by Artru and Mennessier [25] and implemented in the JETSET MonteCarlo event generator by Andersson, Gustafson and Sjöstrand, at the University of Lund [27]. The String Model describes fragmentation starting at the end of the partonic perturbative shower through strings of colour field stretched as the two originary primary produced quarks fly apart.

In this process the kinetic Energy of the quark becomes potential energy of the Colour Strong field between the separating quarks in the amount of about 1 $GeV/1\ fm$, and is eventually available to create new $q\overline{q}$ pairs.

Therefore the color flux tube acts like a string with uniform energy density per unit length. The potential energy of the system rises linearly with the separation distance.

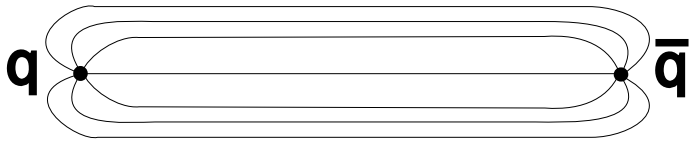

Figure 2.5: *The colour flux tube between quark and antiquark*

In the e^+e^- annihilation into $q\overline{q}$ pairs energy and momentum are conserved at each step of the fragmentation, and all quark quantum numbers are conserved globally.

Figure 2.5 shows the colour flux tube idea behind the string fragmentation model.

In order to generate the quark-antiquark pairs $q'\overline{q}'$ breaking an originary string, the Lund Model of the string fragmentation invokes the idea of quantum mechanical tunnelling. In terms of the transverse mass $m_\perp$ of the generated quark q', the tunnelling probability to generate the $q'\overline{q}'$ pair is given by

$$\mathcal{P} = e^{-\frac{\pi m_\perp^2}{k}} = e^{-\frac{\pi m^2}{k}}\ e^{\frac{-\pi p_\perp^2}{k}} \qquad (2.50)$$

The fact that in this formula the mass term m and the transverse momentum $p_\perp$ factorize produces a flavour independent Gaussian spectrum of $p_\perp$ for the generated $q'\overline{q}'$ quark pairs. Given the fact that strings have no transversal excitations, $p_\perp$ is locally compensated between the quark and the antiquark of the produced pair.
This makes the formula above to have the tendency to underestimate the observed $p_\perp$ spectra since other PQCD $p_\perp$ contributions are not taken into account.
Formula 2.50 implies a suppression of the heavy quark production in the ratios $u : d : s : c \simeq 1 : 1 : 0.3 : 10^{-11}$.
Normally the JETSET Montecarlo program implementing the string fragmentation uses a left-right symmetric fragmentation function, taking into account the primary produced $q\ \overline{q}$ space symmetry for the whole process, given by

$$f(z) = \frac{1}{z}(1-z)^A e^{-\frac{-B\cdot(m_\perp)^2}{z}}$$

(2.51)

This fragmentation function corresponds to a distribution of probability for fragmenting objects per unit mass m and longitudinal momentum z given by

$$\frac{d\mathcal{P}}{dm^2 dz} \propto z^{-1} e^{-bm^2/z} \qquad (2.52)$$

b being a free parameter proportional to the probability for breakup per unit of invariant string area. String fragmentation has to be combined with a perturbative calculation underlying the hard process, either a second-order matrix element calculation or a leading logarithm parton

shower generator.
Concerning baryon production, JETSET has at least 7 free parameters dedicated to the its tuning. Among these, for instance, the ratio of the rate for the production from the vacuum of quark-antiquark states to the rate of production of diquark-antidiquark states (with default value 10) and the POPCORN parameter.
The POPCORN parameter allows the breaking of a string by the creation of a quark-antiquark pair fair apart in the string, in order to increase the rate of baryon production at the end of the colour string itself.
By default in JETSET roughly 50% of the baryons are produced through this POPCORN mechanism.

2.4.2 The Cluster Model and the HERWIG MonteCarlo Program

The Cluster model of fragmentation presents a rather simple and universal description of fragmentation. In this model hadrons derive from colorless clusters of partons produced at the end of the partonic shower [32]. Clusters are characterized only by their mass and their total flavour content. Therefore the internal structure and the directional complexity of the strings (dealing with longitudinal and transversal momentum) is avoided.
The corresponding advantage of cluster models is that they need less parameters to be tuned, with respect to other models : the cluster spectrum may be thought of as a superposition of short lived, broad resonances, whose decay is dominated by phase space properties.
The momentum distribution is determined by the parton shower characteristics and by the phase space decays of the clusters (since Matrix Elements give only four partons at the end of the cascade, Cluster Models are necessarily coupled to a parton shower approach for the elementary hard subprocesses underlying fragmentation).
In the HERWIG Montecarlo generator of Marchesini and Webber [30] a gluon can branch into a $q\overline{q}$ pair or into a diquark-antidiquark $D\overline{D}$ pair. A Leading Log PQCD partonic shower produces therefore quarks and diquarks states, that are preconfined in colour singlets (the clusters).
Branching are governed by the Altarelli-Parisi equations 2.35-2.38.
The evolution variable during the shower is given by $\tau = E_a^2\xi$,
where $\xi = p_b \cdot p_c/(E_b E_c) \simeq 1 - cos\theta_{bc}$, p_b and p_c are the four momenta of the two child partons originating from the mother parton a, θ_{bc} is the angle between b and c.
In HERWIG this variable plays the role of the $log(Q_a^2/\Lambda^2)$ used in other PS models.
The model uses a cut off Q_0 for the virtual mass of the cluster to terminate the decay process, typically $Q_0 \simeq 0.65$ GeV. After the showering led all partons to reach this value of Q^2, the gluons are decayed into $q\overline{q}$ pairs. The colour of all partons is tracked throughout the shower, so that it is possible to combine quarks and antiquarks into colorless clusters. The cluster decay afterwards according to phase space kinematics. The whole model bases on the factorization assumption for the elementary hard subprocess, the final state emission and the hadronization process.
Colour Coherence is one interesting aspect of the HERWIG model, because it is taken into account automatically by the definition of the shower evolution variable itself. This is due to the fact at each branching the full available phase space is by definition restricted to the angular ordered region. Such a restriction is the result of interference and takes leading infrared singularities correctly into account. At each step the angle between the two emitted partons is smaller than that of the step before, without the need for an artificial subsequent

elimination of the available kinematical region like in the string based models.
Therefore HERWIG can be called a *coherent final state branching* generator algorithm.
Since the parton shower produces a large spread in hadron masses, HERWIG uses a mass parameter M_{cl} to constrain the upper limit of the maximum cluster size (typically 5 GeV) : cluster with higher masses are decayed in pair of lighter ones.
Another important parameter is the so called $CLDIR$ parameter, to control the probability to create leading baryon in jets, in principle non foreseen, given the fact that the baryon number of each cluster is 0.
This parameter lets a cluster containing a "perturbative" quark (one coming from the perturbative stage of the event, the hard process or perturbative gluon splitting) to remember its direction.
When the cluster decays, the hadron carrying its flavour continues in the same direction (in the cluster centre of mass frame) as the quark.
This considerably hardens the spectrum of heavy hadrons and it also introduces a tendency for baryon-antibaryon pairs preferentially to align themselves with the event axis.
Of course a crucial parameter of the model is the cut off in the partonic branching itself.

2.4.3 The Modified Leading Log Approximation in the Local Parton-Hadron Duality Ansatz

One of the most Theoretically based approaches to fragmentation models is the so called *Modified Leading Logarithmic Approximation* in the *Local Parton Hadron Duality* ansatz [34].
This is a Theoretical Scheme founded on the Modified Leading Log approximation to handle Parton Shower calculations and on a particular assumption to match the parton and the hadron levels.

2.4.3.1 MLLA

Leading Log Approximation calculations do not include higher orders in the perturbative expansion of the running coupling $\alpha_s(Q^2)$ and therefore are not able to describe accurately the multigluonic production in jets, where the purest Quantum Mechanical effects due to gluon interference play a fundamental role. The gluonic radiation during the hard process in a partonic cascade contribute to the particle multiplicity in the low momenta (soft) region. Therefore LLA is unable to predict accurately the properties of particles with relatively small momenta produced in hard interactions [35] (and therefore unable to describe the particle multiplicities as well). The *Double Logarithmic Approximation* (DLA) represents a first step in the upgrade of the modeling to implement better the effects of the multigluonic contributions to particle spectra.
In the DLA all double logarithmic contributions like $\alpha_s^n(Q^2) log^{2n}(Q^2/\Lambda^2)$ are taken into account.
It can be proved [36] that angular ordering in the parton branching is obtained implicitly, without the need to introduce it explicitly (to keep a probabilistic interpretation for the branching process itself) like is done in LLA.
The energy ordered and angular ordered partonic (gluonic) ladders cross sections of DLA are used essentially to study the particle multiplicities in jets, the multiplicity distribution and mean values.

For instance DLA is sufficient to observe the so called KNO Phenomenon [37], that is the dependence of the multiplicity distributions on the total energy of the system ($ln(Q)$) only via the ratio $n/\overline{n}(ln(Q))$. In QCD the KNO scaling is exact in the limit $Q \to \infty$
The *Modified Leading Log Approximation* by Dokshitzer, V.A.Dyakonov and S.Troyan (1980) [33] represents the ultimate step in the Perturbation Theory of the QCD diagram calculations and takes all logarithmic terms into account (single and double logarithmic) :
$\alpha_s^n(Q^2)\log^n(Q^2/\Lambda^2)$.
The price to pay is a tremendous growth of the number of interference contribution to be calculated. The interference graphs contain soft gluon connecting harder partons of quite different generations. It is amazing to verify the fact that one can keep the probabilistic mainframe of the idea of the Parton Shower (like in the LLA Model), in the sense that it is possible to let the dependence of the probability for a given parton (at a given step of the cascade) to depend on the nearest "fathers" in the shower. All the essential interference terms can be absorbed in the local probabilistic scheme. That's why this approach, better describing the soft particle region, is referred to as to "Modified" Leading Log : the probabilistic showering is a straightforward generalization of the LLA model's one.
One of the most important prediction of the MLLA is the so called *hump-backed* shape of the distribution of the $\xi \equiv ln(1/x_p)$ ($x_p \equiv p/p_{beam}$) variable for parton distributions in e^+e^- annihilation events.
In the limit in which the cut off of the partonic cascade is $Q_0 \simeq \Lambda_{QCD} \simeq 0.2\ GeV$ (limiting spectrum) one can derive the shape for the partonic spectra after fragmentation and MLLA foresees them to be hump-backed like, approximately like a distorted Gaussian [38] curve

$$D = \frac{N}{\sigma\sqrt{2\pi}} e^{(\frac{1}{8}k - \frac{1}{2}s\delta - \frac{1}{4}(2+k)\delta^2 + \frac{1}{6}s\delta^3 + \frac{1}{24}k\delta^4)} \tag{2.53}$$

where $\delta \equiv \xi - \xi^*/\sigma$ and the other parameters are a function of the energy scale (with respect to the cut off Q_0), $Y \equiv log(E/Q_0)$ and other theory parameters.

2.4.3.2 Local Parton-Hadron Duality

The *Local Parton-Hadron Duality* (LPHD) ansatz was introduced by Azimov, Dokshitzer, Khoze and Troyan [34], and states that *the momentum spectra of hadrons are directly proportional to the spectrum of partons produced (up to some cut off scale Q_0) in the MLLA framework approach.*
In other words LPHD states that the whole fragmentation process does not characterize the hadron dynamics, whose origin lays in the parton showering itself, provided the showering is modelled by MLLA. Therefore if $\overline{D}_k^g(\xi, E, Q_0)$ is the distribution of gluons in a jet of energy E, the LPHD ansatz reads, for the fragmentation function of hadron h

$$D_k^h(\xi, E) = K^h \overline{D}_k^g(\xi, E, Q_0) \tag{2.54}$$

where the constant K^h depends only on particular hadron flavour. Therefore LPHD states that the duality of parton and hadron is extended on a local scale up to the level we want to test it. This is a rather constraining, powerful assumption. One of the problem of the MLLA+LPHD scheme is the lack of leading particle effects, in the sense that apparently u,d and s quark should give rise to the same, identical kind of hadronic jets (from the point of

view of the inclusive hadronic content) , given the fact that these three quark flavour produce the same amount of gluons in this scheme. There are already some hints to wonder about the total reliability of this assumption [40], especially in the high momentum region.
However until today the general prediction of MLLA+LPHD have shown to hold remarkably well in many experimental aspects [39] : the ξ spectra are roughly distorted Gaussians like in e^+e^- annihilations. Moreover the peak position ξ_p^* of the ξ_p variable have been shown to increase effectively with increasing energy [34], as foreseen by this model, according to the law

$$\xi_p^* = 0.5 \cdot Y + 0.593 \cdot \sqrt{Y} - \frac{0.3513}{Y} + \mathcal{O}(Y^{-3/2}) \tag{2.55}$$

where :

Y	: $ln(\sqrt{s}/(2 \cdot Q_0))$
Q_0	: effective cutoff in the parton cascade

In this expression the dependence on the hadron mass M_h is contained in the cutoff term Q_0.

Chapter 3

The DELPHI experiment

3.1 Introduction

The DELPHI experiment is mounted at the LEP (**L**arge **E**lectron-**P**ositron) Collider at CERN, where electrons and positrons annihilate, at a total Centre-of-Mass energy of around 91 GeV, corresponding to the mass of the Z boson.
LEP has a circumference of 26.66 km and lays at an average depth of 100 m underground.
The name DELPHI stands for **DE**tector with **L**epton, **P**hoton and **H**adron **I**dentification.
Indeed its different parts (subdetectors) allow Particle Identification of Photons (HPC), Leptons (HPC, Muon Chambers) and Hadrons (RICH, TPC, HPC).
In this chapter a general description of the DELPHI detector is given, mentioning the essential aspects of its subdetectors as well.

The Detector [41] consists of a Barrel (central) part and two End-Caps on each side
(Forwards and Backwards). The general lay out of the detector is shown in picture 3.1.
All the subdetectors mounted on the Barrel Region are concentric with the beam pipe, occupying a radial region between R_{in} and R_{out} specified in the following sections.
The coordinate used to describe a given position relative to a given detector are the polar coordinates r (the radius), ϕ (the angle around the beam axis) and also $r\phi$ to describe the distance along a circle.
The z-coordinate is parallel to the axis of the cylinder (detector) and $z = 0$ corresponds to the interaction point.
The whole detector is in the $|\vec{B}| = 1.2$ Tesla magnetic Field provided by the superconducting coil (radial dimension = 2.75 m, length = 7.4 m). The conductor is made by a single layer of $N_b T_i$ crossed by a current of 5000 A.
The magnetic configuration of the field, parallel to the beam axis (the relative radial component of $\vec{B}$ is approximately $4 \cdot 10^{-4}$) is insured by the two complementary compensating coils (mounted on the End-Caps) at the end flanges of the main coil.

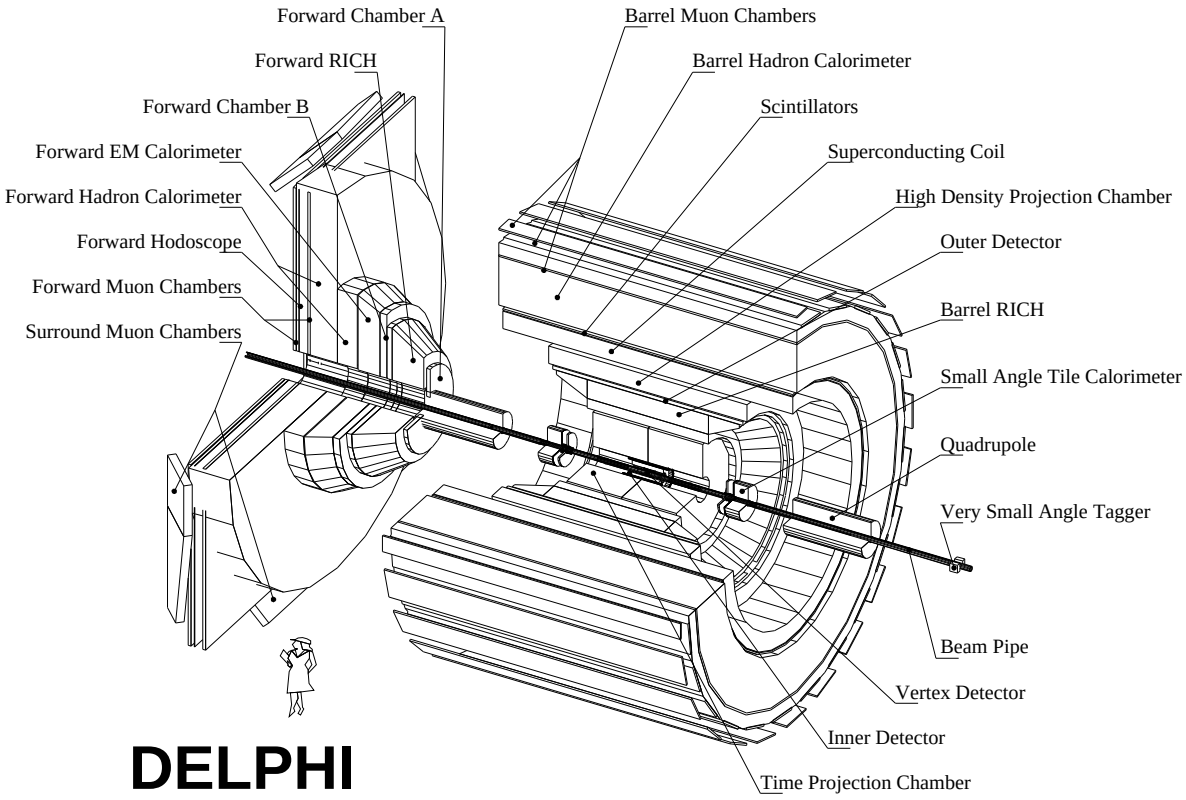

Figure 3.1: *The DELPHI detector*

3.2 Tracking Detectors

The DELPHI tracking in the Barrel Region relays on the information provided by the Vertex Detector, the Inner Detector, the Time Projection Chamber and the Outer Detector.

3.2.1 The Microvertex Detector (VD)

The Microvertex Detector (VD) is made by three concentric layers of Silicon strip detectors, placed at a radial distance from the beam of (respectively) 6.3, 9.0 and 11.0 cm. It is the closest to the beam pipe and covers the interaction region.
The VD covers the polar region corresponding to $31° < \theta^{track} < 149°$. Each one of the three layers is made by four modules in z and 24 modules in $r\phi$. The resolution in $r\phi$ is 8 μm per measured point.
The double track resolution in $r\phi$ is $\leq 100\ \ \mu m$.

The VD plays a central role in the DELPHI performances in b-quark tagging, where the reconstruction of the $2-4\ mm$ displacement of the secondary vertex is essential in the track extrapolation procedure. The presence of the VD hits reduces dramatically the error on the secondary vertex reconstruction and in the tracks impact parameters. Figure 3.2 shows the

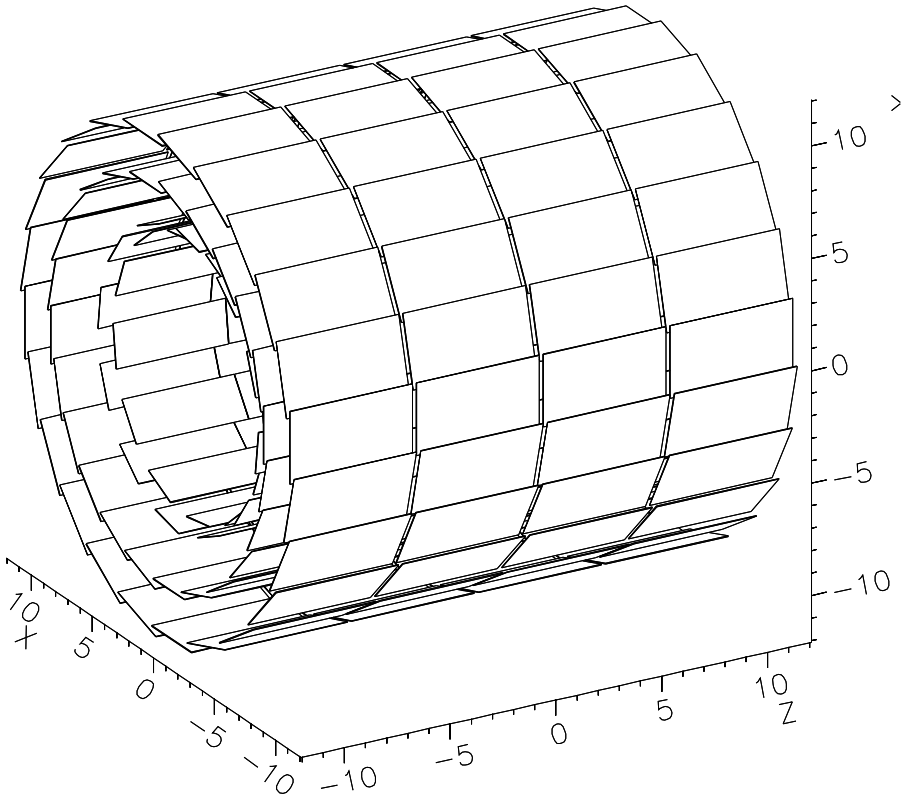

Figure 3.2: *The DELPHI MicroVertex Detector*

structure of the DELPHI MicroVertex Detector.

3.2.2 The Inner Detector (ID)

The Inner Detector is made by a Jet Chamber (polar region $15° < \theta^{track} < 165°$) and a set of 5 cylindrical coaxial Multi Wire Proportional Counters (Trigger) Layers; it has been upgraded in the beginning of 1995.

The Jet Chamber is made by 24 sectors in the azimuthal angle ϕ and is located in the first radial region between $R_{in} = 12$ and $R_{out} = 22\ cm$.
Each sector contains 24 anode wires along z, in rows of increasing r. The electric drift field is

perpendicular to the magnetic field, and therefore the electrons drift with a non zero Lorentz angle. The single wire resolution in $r\phi$ ranges from 75 μm to 125 μm. Since the drift configuration is such that electrons from tracks originated from the interaction point arrive at the anode wires simultaneously, the ID information is used on the DELPHI trigger.
The five Trigger Layers are situated in the radial region between $R_{in} = 23$ and $R_{out} = 28$ cm. Each layer has a Multi Wire Proportional Counter with 192 sense wires (spaced by $8mm$), 192 field shaping wires, stretched parallel to the beam pipe and circular cathode strips giving rz information.
For each track they provide 5 measurements in $r\phi$ and 5 measurements in z. Combining the Jet Chamber and Layers information resolves the Left/Right ambiguities on the position measured in the Jet Chamber. The space resolution of the whole detector is roughly 40 μm (60 μm for 1994 data) in $r\phi$ and approximately 1 mm in z (before 1995).

3.2.3 The Time Projection Chamber (TPC)

The TPC is the central tracking detector in DELPHI. Moreover it provides particle identification through a measurement of the energy loss of charged particles produced in the Z decay. It consists of two halves ($z \geq 0$, $z \leq 0$) with six 60-degrees vessels sectors in ϕ each, for a total of 12 modules.
The active length of the detector is $2*1.34\,m$ and the active radial range is between $R_{in} = 0.325$ and $R_{out} = 1.16$ m; the number of $R\phi$ points per module is 16 for a total of 1680 pads per sector.
The three coordinates are reconstructed as follows : x and y are given by the single pad hits distributions at the end of the drift volume on the collector plane and z is reconstructed by the charge drift time. The whole detector is in the magnetic field of the DELPHI superconducting solenoid of 1.2 $Tesla$, parallel to the beam axis.
A detailed description of the TPC can be found in ref. [62].
Ionization electrons produced by charged tracks in the TPC gas (Ar 80% - CH_4 20%) drift with a velocity of 6.67 $cm/\mu s$, reaching the end-side Multi Wire Proportional Chambers (MWPC) because of a 20000 V very high tension (equivalent to an electric field of 150 V/cm), and their signal is measured by the MWPC wires (set to the High Voltage of 1385 V).
According to the track's polar angle, the TPC measures up to 16 points in 3 spatial dimensions, providing therefore the main contribution to the DELPHI tracking.
The average tracking spatial resolution in $r\phi$ $\sigma_{r\phi}$ ranges from 180 to 280 μm (depending on the ϕ and z), and the average z resolution is 0.9 mm. The average resolution on the stopping power dE/dx measurement is (in hadronic events) $\sigma_{dE/dx} \simeq 6.5\% \cdot (dE/dx)$. A further, more detailed, description of the TPC is given in chapter 5.

3.2.4 The Outer Detector (OD)

The Outer Detector (OD) is composed of 24 planks of 5 layers $\times$ 32 columns of drift tubes (4.7 meters long) , operating in the limited streamer mode. The section of each tube is 1.65 $\times$ 1.65 cm^2. The electrons produced by a charged particle crossing a tube drift toward the wire (high voltage of 4.4 kV) and give a signal with short raise time and high amplitude (typically 3 ns and 80 mV).
It is situated at 2 meters from the beam axis and covers the polar region between 43° <

$\theta^{track} < 137°$.
Because of the long lever arm with respect to the interaction point, it improves the precision of the momenta of charged particles measured by the TPC. Its 5800 electronic channels (in total) give 3 space points plus 2 $r\phi$ points per track.
It has a fast electronic read-out implemented in the DELPHI trigger. Typical resolutions provided by this detector are $\sigma_{r\phi} = 110\ \mu m$ and $\sigma_z = 4.4\ cm$.

3.2.5 The Forward Chamber A (FCA)

The FCA is a tracking detector in the Forward region. Its three modules are mounted on each end of the TPC at a distance of 160 cm in $|z|$ from the interaction point.
Each module is a double layer of drift chambers working in the limited streamer mode. The direction of the wires of each module have a relative orientation of 120° with respect to each other, allowing a good resolution on the reconstructed space points.
It covers the polar region $11° < \theta^{track} < 32°$ and $148° < \theta^{track} < 169°$. In normal conditions (when the direction of the particle is known *apriori*) the space point resolution per layer is roughly 300 μm.

3.2.6 The Forward Chamber B (FCB)

The Forward Chamber B is a tracking drift chamber in the Forward region, situated at an average distance of $|z| = 275\ cm$ from the interaction point.
It covers the polar track angles between $11° < \theta^{track} < 36°$ and $144° < \theta^{track} < 169°$. It has 6 double wire planes which give together high track-finding efficiency. The internal calibration of the chamber is performed using the so called "parallel muons" (the muons in the LEP beam Halo).
Single wire residuals have an average value of 300 μm. The precision in the reconstructed track elements are $\sigma_{xy} = 150\ \mu m$, $\sigma_\theta = 3.5\ mrad$ and $\sigma_\phi = 4.0/sin(\theta)\ mrad$.

3.2.7 Combined Tracking Performances

Given the presence of the magnetic field, in DELPHI the tracking is crucial for the measure of the particle momenta.
The various detectors combined DELPHI tracking performances, in the precision of the momentum measurement, are studied using dimuons (back to back tracks, within 0.15°). In the Barrel region, using the VD, ID, TPC and OD detectors, plotting the distribution of the inverse momenta for dimuons and measuring the width of the obtained distribution ($\sigma_{1/p}$), DELPHI obtains

$$\frac{\sigma_p}{p} \approx 0.57 \times 10^{-3} \cdot p \quad (GeV/c)^{-1} \tag{3.1}$$

In the forward-backward region, using the information provided by the ID, TPC, FCA and FCB detectors, the resolution on the momentum measurement is given by

$$\frac{\sigma_p}{p} \approx 1.31 \times 10^{-3} \cdot p \quad (GeV/c)^{-1} \tag{3.2}$$

3.3 The RICH (Particle Identification) detectors

The RICH detector is the main DELPHI detector devoted to Particle Identification.
Its detailed description is given in chapter 4, since this analysis refers essentially to it. Here only a brief summary is given. It consists of the Barrel (BRICH) and the Forward RICH (FRICH).
The BRICH is subdivided into two halves ($z > 0$,$z < 0$), centrally placed around the beam axis, between the extreme positions $|z| = 177.5\ cm$ w.r.t. the interaction point.
Both detectors let charged tracks perform the Cherenkov effect in two different radiators, a liquid and a gaseous one, (with two different refractive indexes ($n_{liq} = 1.274$, $n_{gas} = 1.00178$) in order to extend the available momentum range for identification. The two perfluorocarbons radiating media are Liquid Freon (C_6F_{14}) and Gas Freon (C_5F_{12}). The identification is performed through the measurement of the Cherenkov angle Θ_C, related to the particle mass and momentum by the relation

$$cos(\Theta_C) = 1/\beta n \tag{3.3}$$

where n is the medium refractive index and β is the relativistic $\beta = v/c$ particle speed. Knowing the particle momentum, identification is performed using the Cherenkov bands, that is the expected Cherenkov angle as a function of the particle momentum:

$$\Theta_C = cos^{-1}(\frac{\sqrt{1 + m^2/p^2}}{n}) \tag{3.4}$$

where m is the particle mass, p its momentum and n the medium refractive index.
The liquid radiator is used to identify tracks in the momentum range 0.7 to 8 GeV/c and the gas radiator in the range $2.5 - 30\ GeV/c$.
The whole detector is kept at a temperature of 40° and at a Pressure of 1033 $mbar$ (20 $mbar$ above 1 Atmosphere).

3.4 Energy Measurement Detectors

3.4.1 The High-Density Projection Chamber (HPC)

The High-density Projection Chamber is located between the Outer Detector and the Solenoid, at a radial distance $r = 208 - 260\ cm$ from the axis and a z position of $|z| < 254\ cm$ and is the electromagnetic calorimeter in the Barrel region.
It consists of 144 independent modules, arranged in 6 rings of 24 modules each. It covers the polar region $43° < \theta^{track} < 137°$. Its thickness corresponds to 18 radiation lengths. It has a granularity in ϕ of 1 degree, 4 mm in z, 9 samples in r, a dynamical range from MIP to 50 GeV showers.
Sets of three modules with the same phi and sign of z are known as "gas lines". Each HPC module is a trapezoidal box with a width ranging from 52 to 64 cm and a height of 47 cm.
The length is 90 cm, except for modules in the first and last rings which are somewhat shorter.
The box is filled with 41 layers of lead separated by gas gaps. An electromagnetic particle showers in the lead and ionizes the gas. The charge drifts to one end of the box, where it is collected by a proportional chamber with pad readout (like in a TPC).

Each layer of material is actually a fiberglass-epoxy support (0.1 mm) with lead wires (1.7 mm) glued to both sides. Resistor chains set up a voltage gradient between neighboring lead wires, giving a constant drift field along z of about 100 V/cm. The 8 mm gaps are filled with 80% Argon and 20% Methane. The electric and magnetic fields are precisely aligned by adjusting the orientation of each box, making it possible for the ionization electrons to spiral all the way to the readout chamber. The charge transmission is limited by transverse diffusion, giving an attenuation length of 3-4 meters (much greater than the longest drift distance).
With a drift speed around 5.5 cm μs, the maximum drift time is 16 μs. The 10-th sampling gap at about 4.5 radiation lengths (shower maximum) is filled with a scintillator plane instead of gas. It is also for the first level trigger.
Each sampling gap ends in a U-shaped brass cathode (8 by 8 mm) with a 20 μm goldplated sense wire. It is the induced cathode pulse that is read out. The cathodes are divided into segments (2-8 cm long), which are connected to their neighbours (above or below) in groups of 3-6. The result is 128 pads in 9 rows, ranging from 2 by 3 cm (first three rows) to 8 by 7 cm (last three rows). It is this pad pattern that defines the granularity in r and ϕ. The pad signals pass through preamplifiers mounted on the chamber and are sent via 40 m of cable to the counting rooms.
The Electronic readout consists of 144 modules with 128 pads each means 18,432 channels. The electronics is grouped into four clusters. Each cluster consists of six crates with 32-channel shaper boards and six Fastbus crates with 32-channel digitizer boards. The shaper circuit suppresses chamber-induced tails and amplifies the signal further.
The 18432 (128 pads $*$ 144 modules) electronic channels of the HPC read out are calibrated using a radioactive gas, referring to the 41.5 KeV line of the ^{83m}Kr. The ^{83m}Kr is produced by a ^{83}Rb source inserted to the gas supply.
The ^{83}Rb decays onto its ground state through a double photon cascade emission. The photon energy is respectively 32.1 KeV and 9.4 KeV.
The HPC energy resolution is given by

$$\frac{\sigma_E}{E} \simeq \frac{32.0\%}{\sqrt{E}} + 4.3\% \quad [E \; in \; GeV] \tag{3.5}$$

A module of the HPC detector is shown in figure 3.3.

3.4.2 The Forward Electromagnetic Calorimeter (FEMC)

The Forward Electromagnetic Calorimeter is made by a Cherenkov lead glass and covers the polar regions $8° < \theta^{track} < 35°$, $145° < \theta^{track} < 172°$.
It is located between $|z_{in}| = 284$ cm and $|z_{out}| = 340$ cm. It consists of two arrays of 4532 blocks. The blocks are truncated pyramids with inner (outer) face dimensions of $5.0 * 5.0$ $(5.6 * 5.6)$ cm and a depth of 40 cm, corresponding to 20 radiation lengths.
The Cherenkov lead signal induced by charged particles in the shower is read out by a single stage photomultiplier triode.
The reconstruction of electromagnetic showers is performed in two stages.
First an iterative search of energy cluster is performed. Second the information from the tracking system is used to separate charged by neutral clusters. Bhabha events are used to calibrate the whole detector.
The energy resolution can be parameterized by

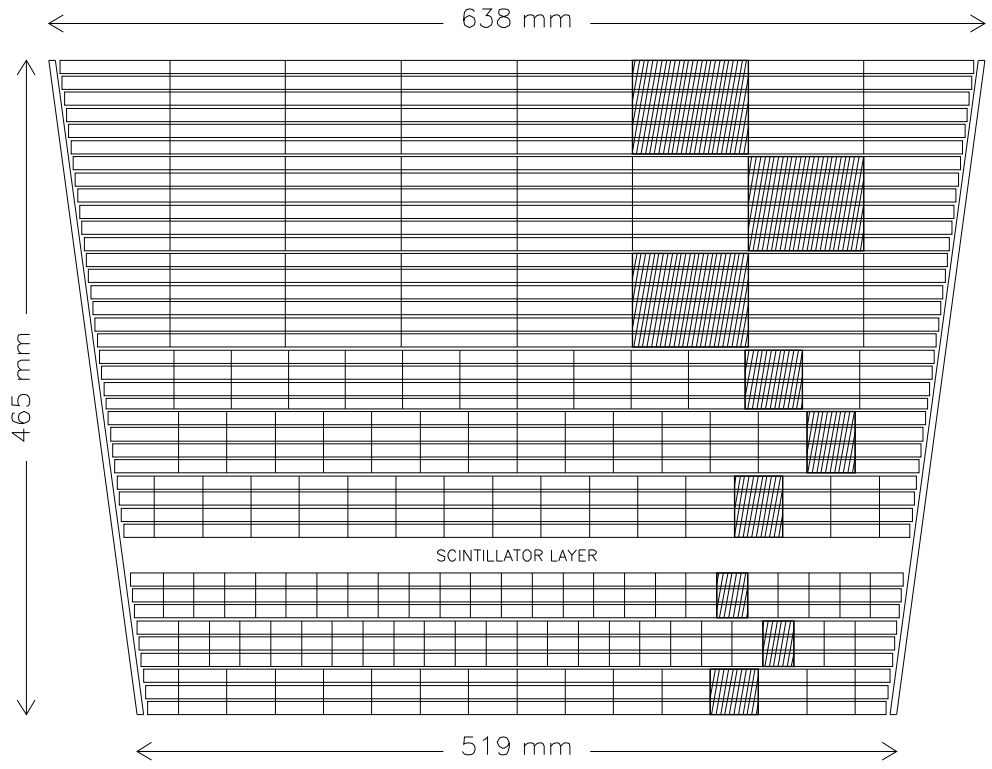

Figure 3.3: *The HPC module*

$$\frac{\sigma_E}{E} \simeq 0.03 + \frac{0.12}{\sqrt{E}} + \frac{0.11}{E} \quad [E \; in \; GeV] \tag{3.6}$$

The spatial resolution of the detector is given by

$$\sigma_{xy} \simeq \frac{8.2}{\sqrt{E}} \; [mm] \qquad (\; E \; in \; GeV \;) \tag{3.7}$$

3.4.3 The Hadron Calorimeter (HAC)

The Hadron Calorimeter is situated between the radial positions $r_{in} = 320 \; cm$ and $r_{out} = 470 \; cm$, in the return joke of the DELPHI solenoid.
It is an Iron-Gas-Sampling calorimeter and covers a wide polar angle region : $8° < \theta^{track} < 35°$.
It is made out of two endcaps (12 sectors each, Forward HAC) and a barrel part (24 modules in $r\phi$). The B-HAC consist of 20 sandwich layers of 5 cm iron and 1.7 cm LST detectors, with a length of 760 cm. The 19,000 limited streamer tubes are mounted on copper readout boards. The energy resolution has been measured to be

$$\frac{\sigma_E}{E} \simeq \frac{112.0\%}{\sqrt{E}} + 0.21 \quad [E \; in \; GeV] \tag{3.8}$$

3.5 Scintillators

3.5.1 The Time of Flight Detector (TOF)

The Time of flight detector consist of scintillator counters around the Superconducting coil. It covers the polar region $41° < \theta^{track} < 139°$. It is made out of 172 scintillators, each one equipped with a photomultipliers at each end.
Its purpose is to eliminate cosmic events and to contribute to the first level trigger.
The precision on the z coordinate is about 20 cm.
TOF is also used to provide information for the particle (essentially photons) that go in the dead regions of the inner-most detector layers of DELPHI, complementing the HPC in the photon reconstruction of DELPHI.

3.5.2 The Forward Hodoscope (HOF)

The Forward Hodoscope is made by scintillator detectors. It is situated between the endcap joke and the second layer of the muon chambers.
It is organized in 4 quadrants with 28 counters each. It is used as a trigger for muons in the Forward region.

3.6 The Muon Chambers

3.6.1 The Barrel Muon Chambers (MUB)

The Barrel Muon chambers are made by three layers of detector planks placed at different r : $r = 444.5$, $r = 479.3$, $r = 532.0$ cm. The detector covers the polar region $53° < \theta^{track} < 127°$
Each plank is at its time made by several layers (3 for the inner plank and 2 for the middle and outer plank). Every layer is made by drift chambers (operating in the proportional mode) of the dimensions $2.0 \times 20.8 \times 532.0$ cm, side by side.
Two consecutive layers chambers do overlap with each other. The planks of the inner layer are embedded inside the return joke of the magnetic coil, at a distance of 20 cm from its outer surface. To cover the gap in the azimuth ϕ left over by the inner and middle layers, the outer layer do overlap with them.
The $r\phi$ coordinate is measured by the drift time of the ionizating electrons and the z coordinate is measured by delay lines.
The achieved precision are $\sigma_{r\phi} \simeq 3.0$ mm and $\sigma_z \simeq 1.8$ cm.

3.6.2 The Forward Muon Chambers (MUF)

The Forward Muon Chambers are subdivided in 4 quadrants. The detector covers the polar region $9° < \theta^{track} < 43°$ Every quadrant consist of a double layer of drift cells, with a 90° two layers relative rotation.
The spatial resolution per read out plane is $\sigma_{x,y} \simeq 3.0$ mm.

3.7 Luminosity Measurement Detectors

3.7.1 The Small Angle Tile Calorimeter (STIC)

The Small angle Tile calorimeter (STIC) is situated at a distance of $|z| = 220\ cm$ from the interaction point along the detector axis.
It measures energy and Luminosity.
The STIC is a sampling lead-scintillator calorimeter made by two cylindrical detectors placed on either side w.r.t. the interaction region.
It provides the calorimetric coverage in the very forward region. It is built with the so called "Shashlik" (skewer) Technique, that allows to insert tracking detectors within the sampling structure. This improves the precision in the determination of the showering particle direction and enhances the e^{-}-$\pi^{\pm}$ separation power.
By detecting the Bhabha scattering it provides (since the Bhabha cross section is well known) a measurement of the LEP Luminosity provided to DELPHI.
For each event, the following informations are produced :

- The Calorimeter information: the energy deposited in the 320 towers (160 per side) is recorded.
- The Silicon detectors information: there are 3840 silicon strips that help in the reconstruction of the shower direction.
- The Veto Counter information: the 64 scintillator wedges in front of STIC are used to separate charged from neutral showers.

The energy resolution at 45 GeV is 3%. The spatial resolution of the calorimeter alone is 1.5° in (ϕ) and from 300 μm to 1 mm in radius.
The resolution of the silicon strips (1.7 mm pitch) over the measure of radial coordinate is 400 μ . The systematic error in luminosity measurement is 0.2%.
Dedicated electronics is used to produce the local trigger results for the first and second level.
Picture 3.4 shows the STIC detector.

3.7.2 The Very Small Angle Tagger (VSAT)

The Very Small Angle Tagger is a luminosity monitor. It covers the very forward region, polar angles $0.29° < \theta^{track} < 0.4°$.
It is located 7.7 meters away from the interaction point. It is a W/S_i calorimeter, whose relative energy resolution is about $\simeq 5\%$ for 45 GeV/c momentum particles. Its depth corresponds to 24 radiation lengths.

3.8 Trigger

At LEP, with eight bunches of electrons and positrons circulating at equal distances, the bunch crossings occur every 11 μs.
Given the high LEP luminosities, the DELPHI trigger system is organized in 4 different (successive) trigger levels (T1, T2, T3, T4) of increasing selectivity.

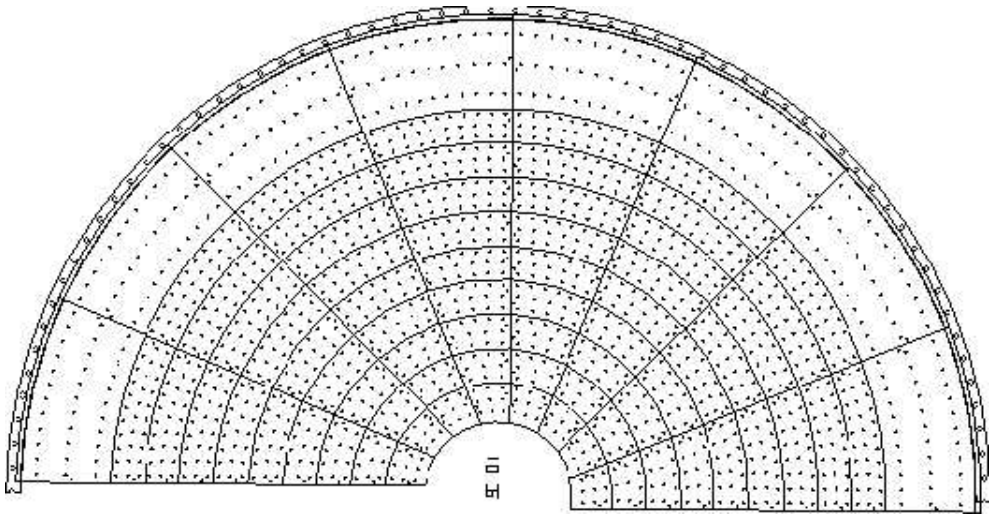

Figure 3.4: *Section of the STIC Calorimeter*

T1 and T2 are synchronous with the Beam Crossing Over (BCO) signal. The first level trigger is a loose pre selection trigger level, while the T2 trigger rules the data acquisition of the front-end electronics.
The T1 and T2 trigger decision are taken 3.5 μs and 39 μs after the BCO signal respectively. The corresponding induced dead time is roughly 3% (2% due to T1 and 1% due to T2. The typical readout time is 3 ms per event.
Input to the T1 trigger is the information coming from the fast tracking detectors (ID,OD,FCA and FCB), by the scintillators (TOF and HOF), by the HPC scintillators, by the Forward Electromagnetic calorimeters and the Muon Chambers (MUB).
In T2 these information are complemented by signals from the Time Projection Chambers, HPC, Forward Muon Chambers and the individual subdetectors.
T3 and T4 are software filters running asynchronously with respect to the BCO.

T3 halves the background passing through the T2 triggers, using the same trigger selection logic but using more detailed information. T4 was implemented in 1993, to tag (and in 1994 also to reject) about half of the background still remained after T3.
Every DELPHI subdetector participates to the trigger decision providing data coming from its subtrigger processors.
Redundancy between the different trigger components also makes it possible to determine both the trigger efficiency and its errors with good precision.
The configuration of the trigger signal T2 used up to 1994 is given in table 3.1 :

- Track elements give trigger signals in the TPC, FCA/FCB, ID, OD and TOF. A transverse momentum cut $p_t \geq 1$ GeV/c for $29° \leq \theta \leq 151°$ (TPC) and $p_t \geq 1.6$ GeV/c in the forward/backward region (FCA/FCB) $11° \leq \theta \leq 33°$ and $147° \leq \theta \leq 169°$ is applied.

- Muons also give trigger signals in the barrel region, $50° \leq \theta \leq 130°$ with a 1° hole at 90°, in the MUB and in the forward and backward regions, $15° \leq \theta \leq 41°$ and

Luminosity					
Trigger	Rate (Hz)	Detection			
		e	μ	γ	$c^{\pm}$
SAT/STIC Bhabha	0.8	•			
Single arm	0.4	•			
Delayed Bhabha	$\ll$0.1	•			

Barrel region					
Trigger	Rate (Hz)	Detection			
		e	μ	γ	$c^{\pm}$
TPC	0.8	•	•		•
OD*HPC	0.2	•		•	
OD*TOF	0.4	•	•	•	•
HPC*TOF	0.3	•		•	
HPC $\geq$2 clusters	0.1	•		•	
ID*(MUB+HAB)	0.5		•		•
HPC (Single-γ)	0.3	•		•	

Intermediate region					
Trigger	Rate (Hz)	Detection			
		e	μ	γ	$c^{\pm}$
ID*(HAF+MUF)	0.1		•		•
HPC*(HAF+FEMC)	0.1	•		•	

Forward/Backward region					
Trigger	Rate (Hz)	Detection			
		e	μ	γ	$c^{\pm}$
TPC*FCA/B	0.2	•	•		•
MUF*FCA/B	0.1		•		
TPC*MUF	0.1		•		
FEMC*FCA/B	0.2	•			
FCA/B*HAF	0.4		•		•
HOF Back-to-back	0.3		•		
FEMC$\geq$2 clusters	0.2	•		•	
FEMC (High Threshold)	0.5	•		•	

Calibration and special triggers		
Trigger	Rate (Hz)	Detection
NIM	0.04	Random trigger
TPC*(SAT/STIC)	0.1	Two-photon trigger
TOF*HAB (High Threshold)	0.2	Search trigger
HOF*MUPARAL	0.1	Halo-μ trigger

Table 3.1: *List of triggers in T2. The names of the participating subdetectors are indicated together with the rates and the sensitivity to electrons (e), muons (μ), photons (γ) and charged particles ($c^{\pm}$). The logical "OR" and "AND" combinations are shown as "+" and "*", respectively.(From PPE/95-194)*

$139° \leq \theta \leq 165°$, in the HOF and in the MUF.

- Electromagnetic energy deposition gives trigger signals in the barrel region in the HPC and in the forward/backward regions in the FEMC. Energy depositions above 2 GeV and 2.5 GeV respectively are demanded. A lower threshold is applied in the FEMC (1.2 GeV) when it is correlated with other detectors.

- Hadronic energy deposition gives trigger signals in the Hadron Calorimeter, both barrel (HAB) and forward (HAF). Energy deposition thresholds of 0.5, 2 and 5 GeV -this last is referred as High Threshold- are used.

3.9 Data Handling and Detector Running

DELPHI has an online system controlling and ruling the Data Handling, the whole Data Taking procedures and the running and maintenance of the detector. The DELPHI online system has three basic purposes :
The Data Acquisition System [44] reads out digitized data from the detector; The data are also used to monitor detector performance online; Detector operation is monitored and controlled by the Slow Controls system [48].

3.9.1 The DELPHI Data Acquisition

The DELPHI Data Aquisition is organized and based on the Fastbus standards and uses over 150 Fastbus crates and more than 70 microprocessors. The Data Acquisition is divided into sub sets called "partitions" corresponding to subdetectors or half a subdetector, and one for the trigger system. Each partition uses its own digitization modules. In order to reduce the dead time at each trigger, almost all front-end modules are equipped with a 4-event buffer. The main task of the DAS on receiving a T2 trigger is to switch to the next buffer, if available. The handling of the trigger and the read-out of the front-end digitizers are performed by the "Crate Processor" package, consisting of a general skeleton with hooks for detector dependent readout routines and real time configuration, running inside a 16 MHz M68020-based Fastbus master called a FIP (Fastbus Intersegment Processor). The readout of each individual partition is performed asynchronously by the so called "Local Event Supervisor" (LES) software process, also running in a FIP. This software is fully standard, only a few partitions needing a specialized formatting routine. At this level, the data are already formatted as banks in the ZEBRA memory management [49]. The events are first transferred and formatted in the Spy Event Buffer (SEB). They are then copied into the Multi-Event Buffer (MEB) if the detector is being read out centrally and to a dedicated VAX station (one for each subdetector) for monitoring and for standalone tests. The central readout is controlled by the Global Event Supervisor (GES) software process. It uses all the messages issued by the LESs to build an event inside a Fastbus memory, the Global Event Buffer (GEB). The actual transfer is done by a Fastbus Block Mover. The full ZEBRA structure of the event is set up in the GEB. Only those events which have been accepted by the third level trigger (T3) are built. They are then transferred to the VAX online cluster by means of a CERN Host Interface (CHI), connected to a VAX mainframe by an optical fibre. Before

1995, the disk files were then copied locally onto IBM3480 cartridges. Now they are sent over the FDDI optical link network to a Central Data Recording facility at the CERN computing centre where they are copied onto high capacity tapes (10 GByte Digital Linear Tapes). From there, the offline data analysis farm of DELPHI performs the final reconstruction.

3.9.2 DAS Control System

The control of the data acquisition system is performed by a programmed state machine (State Management Interface, SMI). Normally SMI handles objects, states of objects, and actions to be performed on these these objects. It allows states to be changed on the occurrence of events in other objects. An SMI process runs for each domain to be controlled (e.g. subdetector DAS control and LEP state control). The DAS SMI subsystem has one control unit per partition while a central control unit is used to handle the central readout. The run control is implemented using SMI through a dedicated user interface implemented using the MOTIF standard (DELPHI User Interface, DUI. It allows the operator to reconfigure the system at will, define the data taking conditions, and start and stop data taking. In order to ease operations, an Autopilot system, also implemented in SMI, can be used to force the system to be permanently in a data taking state. It takes all appropriate actions and asks for intervention only when needed. An even higher level of control, known as "Big-Brother" links the DAS SMI domain to the Slow Controls and to LEP. It detects changes in the LEP machine status to automatically ramp the voltages on the detector up and down and prepare, start and stop the DAS such that data are collected with a maximum efficiency but only while LEP and the detector are in good data taking conditions.

3.9.3 Slow Controls System

The Slow Controls system [48] controls the operation of the detector, reporting and (where necessary) acting on significant changes in the detector or its environment, recording such changes where required for the data analysis, and maintaining the safety of the equipment.

Most front-end monitoring and control of temperatures, low voltages, fastbus power supplies, etc., is performed by digital monitoring, relay, and ADC cards in 90 G64 [46] microcomputers. Most high voltages are supplied by the intelligent CAEN [47] system, controlled by G64. Each G64 accepts commands from, and reports significant changes to, the VAX "Elementary Process" responsible for the subsystem. In most cases, standard, configurable, G64 and Elementary Process programs are used. The operator is alerted to problems via the Error Message Utility (EMU) and SMI. Communications between the Elementary Processes and the G64s, database server, and EMU use the Remote Procedure Call model, DECnet and OSI transport protocols, running over Ethernet. Operator and automatic control is effected using SMI. For potentially dangerous conditions, automatic actions implemented in SMI complement hardware interlocks. The high voltages are raised at the start of a fill in order to take data, and (for many parts of the detector) lowered at the end of a fill to prevent damage from high currents during refilling. These actions are performed under SMI control, either automatically (Big Brother) or at the instigation of the operator. During data-taking, significant changes in parameters required for the subsequent data analysis (such as chamber pressures, temperatures, voltage values or the operational status of any subdetector or

subdetector module) are recorded on the central database by the Elementary Process using a dedicated server process, which sends a copy of all updates to the offline data analysis farm for use by the analysis program. This system has allowed a single operator to oversee 12609 detector monitoring and control channels.

Chapter 4

The Barrel Ring Imaging CHerenkov Detector (RICH) in DELPHI

4.1 Introduction

The Cherenkov effect was discovered by Pavel Cherenkov, a russian Physicist, at the beginning of the thirties. His work was published in many different articles written in russian from 1934 to 1937 ([51]).
At the beginning he thought that the observed emitted radiation from Radium decays particles was a fluorescence effect. After some investigation he excluded this explanation. He showed that fast electrons from a Radioactive source emitted polarized radiation while crossing some Liquids.
Later on again two russian physicists, Frank and Tamm [52] provided the first theoretical explanation of this effect as we know it now. Cherenkov, Frank and Tamm got the Nobel Prize because of their contribution to this discovery on 1958.
The Cherenkov effect was later on employed in Particle Physics experiments, and played an important role in the discovery of the anti-proton in 1955.
In the early seventies T.Ypsilantis and J.Seguinot [58] started working on the Ring Imaging Cherenkov (RICH) detectors to perform particle Identification through the Cherenkov ring reconstruction idea.
The first operational experiment using a RICH detector was the E605 experiment at Fermilab. Using a proton beam from the Tevatron Collider ([50]) particle ratios in p-Be and p-W interactions at $\sqrt{s} = 38.8\ GeV$ were measured.
In this chapter a description of the general structure and operation of the DELPHI Ring Imaging Cherenkov detector is given.
First the general operating principle of the Ring Imaging technique is given and then the DELPHI Barrel RICH detector is described : The DELPHI collaboration has designed and implemented a Cherenkov Ring Imaging Detector which surrounds the interaction region. The Barrel part of the detector is fully operational since October 1991.
The RICH measures the emission angle of Cherenkov light photons emitted by charged particles crossing first a 1 cm $\times$ 22 m^2 liquid radiator (filled with liquid fluorocarbon C_6F_{14}) and

then a 40 $cm \times 32\ m^2$ gas radiator (filled with Gas Freon C_5F_{12}). The light is detected by a 5 $cm \times 27\ m^2$ photon converter, acting as a Time Projection Chamber.

4.2 Basic Operating Principle

The RICH detection Technique is founded on the Cherenkov Effect. This takes place when a charged particle travels faster than light in a given medium, like a gas ore a liquid. If the speed v of the particle is higher than the light speed c/n in that medium, the polarized molecules of the medium emit electromagnetic radiation (photons) on a cone whose axis is the particle trajectory direction. The opening angle (Θ_C) of this cone is given by the Cherenkov relation

$$cos(\Theta_C) = \frac{1}{\beta n} \tag{4.1}$$

where β is the relativistic beta of the particle ($\beta = v/c$) and n is the medium refractive index ($n = \sqrt{(}\epsilon(\omega))$).
The spectrum in frequency of the emitted photons is in between (below) the anomalous dispersion region of the medium ($\omega > \omega_0$) and (above) the frequency (ω) value for which $\epsilon(\omega) = 1/\beta$.
If β is very close to one, the frequency range can be very extended so that one could consider the Cherenkov radiation spectrum almost flat as a function of the radiated photons frequency. The crucial parameter is therefore the refractive index of the medium governing the whole process.
For different particle flavors (i.e.masses) this corresponds to different thresholds in momentum for emitting Cherenkov light.

$$p_{threshold} = \frac{m}{\sqrt{n^2 - 1}} \ . \tag{4.2}$$

In the DELPHI liquid Freon (C_6F_{14}) radiator (n=1.2718) a charged pion emits Cherenkov light only if its momentum (p) is above 0.17 GeV/c, a kaon if $p > 0.7$ GeV/c and a proton if $p > 1.2$ GeV/c.
In the Gas Radiator (C_5F_{12}, n = 1.00194) the momentum thresholds in GeV/c are 2.3 GeV/c for pions, 8.2 for Kaons and 16.0 for protons.
DELPHI uses therefore two different radiator media to be sensitive to different momentum

	Liquid Radiator	Gas Radiator
π^+	0.17 GeV/c	2.3 GeV/c
K^+	0.7 GeV/c	8.2 GeV/c
p	1.2 GeV/c	16.0 GeV/c

Table 4.1: *Cherenkov thresholds for π^+, K^+ and p in the two radiators*

ranges, since with increasing momentum ($\beta \rightarrow 1$) all flavors Cherenkov angles tend to a saturated common value given by

$$cos(\Theta_{C\,sat}) = \frac{1}{n} \tag{4.3}$$

This corresponds roughly to 65 mrad in the gas and 670 in the liquid radiator. When a particle is in the momentum region where it can emit Cherenkov light we speak of "positive identification" or **Signal** region . On the other side when the momentum of a particle is below the Cherenkov threshold we speak of "negative identification" or **Veto** Region, meaning that also the fact that a particle did not radiate light for a given momentum provides information on its possible flavour. The RICH identification makes use therefore of the information on the particle momentum (coming from the tracking detectors fit) to extract the expected Cherenkov Angles (or the expected no light emission) for a given particle flavour and to compare it with the measured angle, i.e. to extract a probability performing therefore Particle Identification. The number of detected photo electrons is a crucial parameter for RICH detectors. It can be written as

$$N_{detected} = N_0 \cdot L \cdot sin^2(\Theta_C) \tag{4.4}$$

where L is the length of the particle path in the radiator material and N_0 is the so-called *quality factor* of the detector which is defined as

$$N_0 = \frac{q^2\alpha}{\hbar c} \cdot \int e(\omega)d\omega \; = \; 370(cm \cdot eV)^{-1} \cdot \int e(\omega)d\omega \tag{4.5}$$

where q is the charge of the particle in units of the electron charge, α the fine structure constant, $\hbar$ the Planck constant and c the speed of light in vacuum. $e(\omega)$ designates the detection efficiency per photon wave length interval and accounts for the influence of the detector design and the materials used. The integral is taken over the wave length range in which the photons are detected. For the DELPHI RICHes this is between 160 nm and 220 nm. The first limit originates from the transparency cutoff of the quartz walls and the second from the quantum efficiency of TMAE, as we shall see later. A high N_0 value is clearly important for the operating of a RICH detector. In the case of DELPHI, a charged track is detectedby on average 8 Cherenkov photons in the gas and 12 photons in the liquid.

The RICH detector is designed to let charged tracks perform the Cherenkov effects in a 1 cm thick Liquid Radiator and in a 40 cm thick Gas Radiator and to detect the emitted individual photons on a drift tube, where they convert in photoelectrons because of a photoconvertive substance called TMAE (with a ionization potential in the ultraviolet region corresponding to the Cherenkov photons, $\lambda = 100 - 300\ nm$). The Cherenkov effect in the case of the RICH detector working principle is shown by figure 4.2.
In order to maximize the track path length in the gas radiator (and therefore the number of emitted photoelectrons), mirrors have been used to reflect back on the drift tube the radiated photons, so that all the 40 cm depth of the gas radiator is a radiating active region.
A detailed description of the DELPHI Barrel RICH is given in the following section.
Figure 4.2 shows the measured angle by the two radiators for DELPHI 1994 DATA.

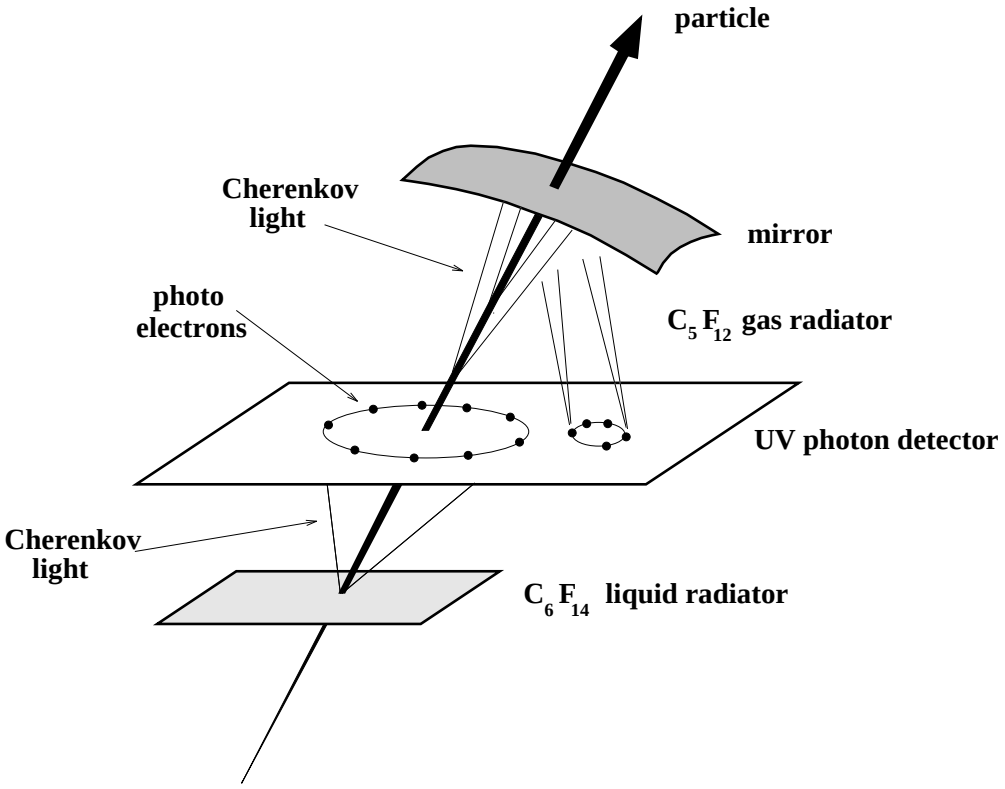

Figure 4.1: *The Cherenkov Effect in the case of the RICH detector working principle.*

4.3 BRICH Detector general description

The Barrel RICH detector consists of 48 nearby identical elements. It appears as a big tick tube surrounding the LEP e^+e^- beam axis, whose thickness is about 60 cm, and located between 1.30 m and 1.90 m from the beam axis. It occupies 1.52 m on each side ($z > 0$, $z < 0$ of the interaction point; 24 elements are on the $z > 0$ side and 24 on the $z < 0$ side.
Each element consist of a liquid radiator, a drift tube, 6 mirrors.

At a distance of 1.3 m from the beam axis is the Liquid Radiator box, 1.5 m long, 1 cm thick. It covers an azimuthal angle region corresponding to 15°.
The liquid radiator is filled with liquid Freon (C_6F_{14}), having a low index of refraction (1.274) and is transparent to ultraviolet radiation down to 170 nm.
The opposite side to the interaction region is made of UV quartz, transparent to UV light down to 160 nm. The photon detector (drift tube) is parallel to the liquid radiator and is radially located at 145 cm from the axis. It is TPC-like detector with a drift field of 0.36 kV/cm,

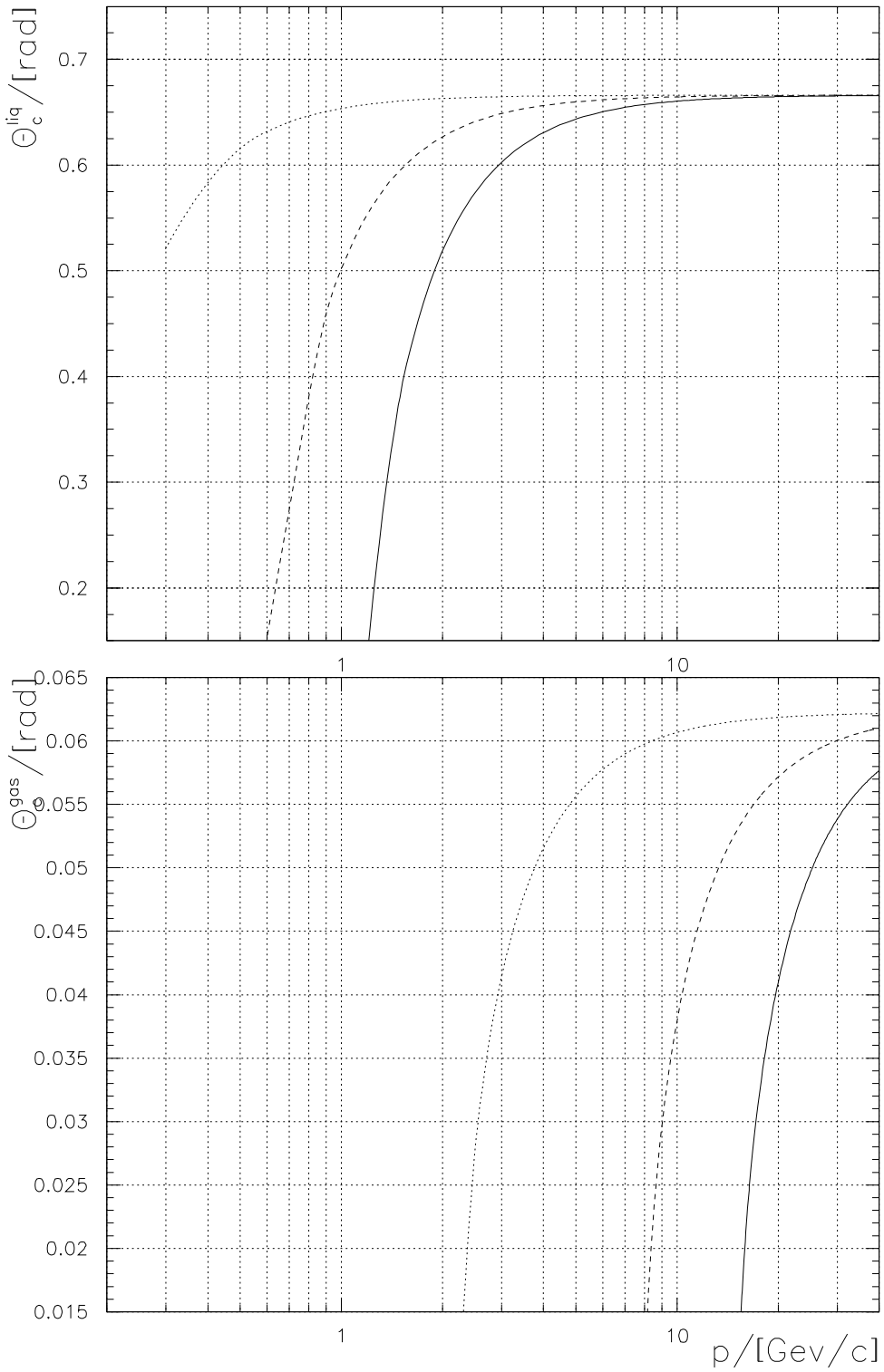

Figure 4.2: *The Expected Cherenkov Angle versus particle momentum in the Liquid (above) and Gas (below) Radiators for pions (dotted line) , kaons (dashed), protons (full line).*

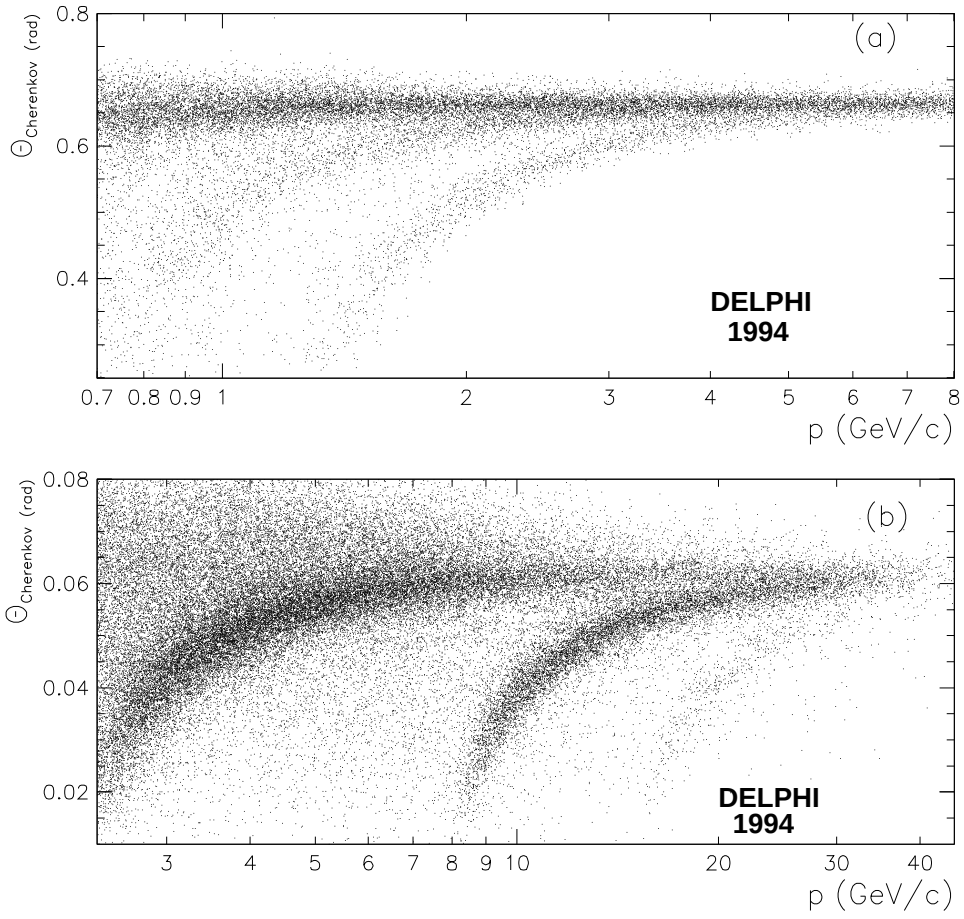

Figure 4.3: *The Measured Cherenkov Angle versus particle momentum in the Liquid (above) and Gas (below) Radiators. Visible are the three pion, kaon and proton bands. Electrons and Muons are undistinguisheable from pions.*

liquid radiator medium	C_6F_{14}
gas radiator medium	C_5F_{12}
drift gas	CH_4 (75%)-C_2H_6 (25%)-TMAE($\simeq 0.1\%$)
liquid radiator refractive index n_{liq}	1.274
gas radiator refractive index n_{gas}	1.00184
n.bitubes	2×24
n.liquid radiators	2×24
liquid radiators tot. volume	240 l
n.MWPC	2×24
bitube module length	152 cm
bitube module width	32 cm
track polar angle coverage	$40° < \theta^{track} < 140°$
longitudinal diffusion factor	210 $\mu m/\sqrt{cm}$
transversal diffusion factor	100 $\mu m/\sqrt{cm}$
Single MWPC read out in X :	8×16 wires
Single MWPC read out in Y :	8×16 strips
total n. mirrors	288
operating temperature	40° C
operating pressure	1030 nP
total n.read out channels	12288
Very High Voltage drift tension	54000 V
Drift field intensity	0.36 kV/cm
Photoelectron drift speed	5.15 $cm/\mu s$
n.of 3 $M\Omega$ resistors	500

Table 4.2: *Summary of the DELPHI Barrel RICH main characteristics.*

along the z direction.
It is filled with Methane, CH_4 (75%), Ethan , C_2H_6 (25%) and TMAE($\simeq 0.1\%$) (Tetrakis-dimethylamine-ethylene), a photosensitive agent to convert radiated Cherenkov photons into electrons in the drift tube.
In order to minimize drift diffusion effects and maximize the electron collecting efficiency it has a pyramidal shape : its thickness varies from 4.2 cm at the start of the drift region to 6.2 cm on the detecting side.
The operation of the Barrel RICH [54] has imposed the following design constraints:

- The drift tube is made entirely of UV transparent (down to $\lambda = 165$ nm) quartz plates in order to cope with the spectral quantum efficiency of TMAE.

- The operating temperature of the detector is 40° C since the gaseous radiator is liquid at room temperature and the vapor pressure of TMAE allows a sufficient high concentration in that temperature range only.

- The drift field - up to 0.36 kV/cm - ensures drifting without distortions and it is determined by a High Voltage (HV) of up to 54 kV on the mid wall. This requires good electrical insulation and demands great care in the design of the electrostatics (to avoid coronas and field deformations).

- The RICH is operated at a pressure of 1033 $mbar$ in order to overlap the identification range of the gaseous radiator with the one of the liquid radiator, by increasing the index of refraction of the gas.

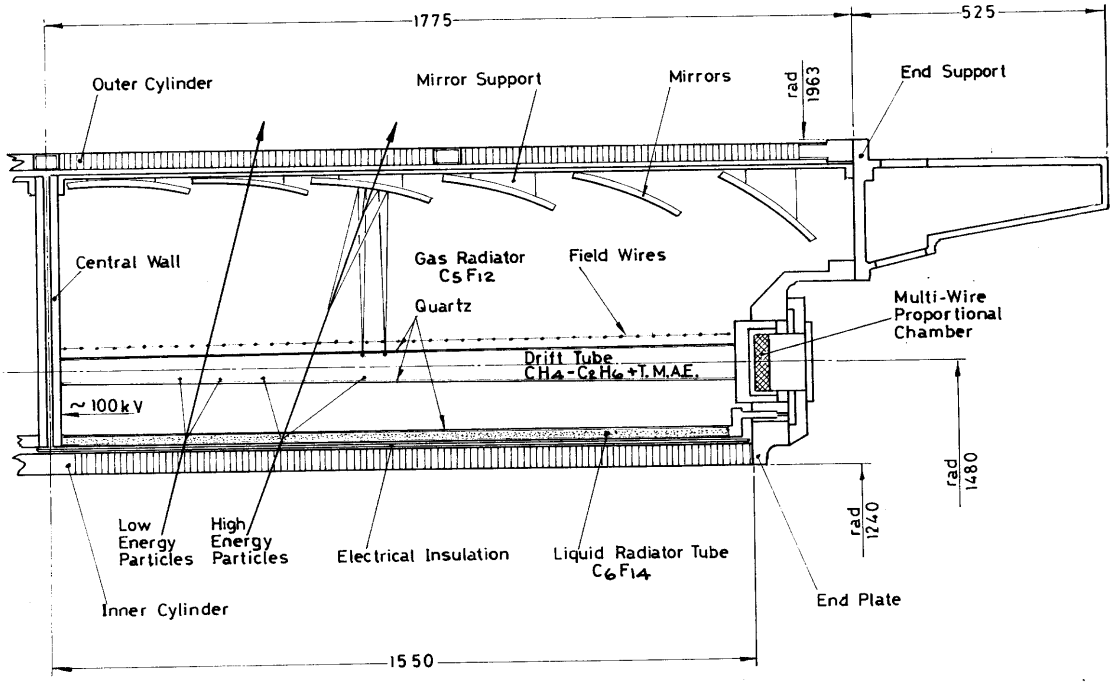

Figure 4.4: *Cross section of a Barrel-RICH module.*

A detector's element is sketched in fig.4.4 and a summary of its characteristics is given by table 4.2.

4.4 The Vessel

The BRICH detector is enclosed by the inner and outer cylinders and the two end flanges. The cylinders are made of aluminium honeycomb sandwiches in order to keep the overall material radiation length small. The whole vessel has been tested to stand an overpressure of 0.4 bar. It is fixed to the inside of the cryostat of the Superconducting Magnet coil. Its mechanical

stiffness allows the tracking detector of the Barrel region to be fixed on to the cylinders of the Barrel RICH. All Vessel components are equipped with heating devices, to keep the whole detector at the operating temperature of 40°.

The inner cylinder is 45 mm thick; an electrical insulator (made of mylar foils, 75 μm thick) is glued onto it by means of a polyurethene glue. It plays an important role in the definition of the BRICH electric field. The mid-wall (dividing the RICH in two symmetrical side along z) is connected to the drift Very High Voltage (VHV) (54 kV). The VHV is degraded all along the length of the inner cylinder down to a zero value, corresponding to the end flanges. This is done using a Kapton foil with copper strips, with a width of 3 mm and a pitch of 6 mm.
The strips form circles running perpendicular to the detector axis. They are interconnected by a resistor bar (degrader) chain.

The outer cylinder has a diameter of 3.85 m and a total length of 3.55 m. It consists of a sandwich of 30 mm Al honeycomb in between two sheets (each 1 cm thick) of aluminium. Heating circuits and Thermal insulation are mounted on the outside.

The outer flanges represent the mechanical reference for the whole Barrel RICH : upon them are fixed the mirror cages, the drift tubes (bitubes) with their MWPC's and the liquid radiator boxes. They are made of aluminium, electrically heated.

4.5 The Drift Tube

The Barrel RICH contains in total 48 (2 $\times$ 24) drift tubes. Each drift tube is made out of 4 mm thick quartz, is 155 cm long, 34.5 cm width, internal hight (in the radial direction) 4.2 cm at the HV and 6.2 cm at the support side : this tapering minimize electron diffusion spread during the drift.
The tubes are grouped into sets of two for practical design reasons, to form the so called *bitubes*.
In azimuth (ϕ) each bitube covers 30°. The main goal of the drift tubes is of course to let the produced Cherenkov photons to convert into electrons by TMAE induced photoconversion and let the produced electrons drift up to the end of the drift tube by means of the electric field and be detected by the multi wire proportional chambers.
The drift gas is made of a mixture of Argon (Ar) 80% and Methane (CH_4) 20% with a small percentage of TMAE (0.1%). Photoelectrons travel on average with a drift speed of 5.15 $cm/\mu s$ The Very High Voltage providing the electric field is a 54 kV tension kept between the midwall and the end flange, where the multi wire proportional chambers are. A degrader bar made by 500 Resistors, each of 3 $M\Omega$, shapes the drifting field, whose orthogonal component is less than 10^{-4} its longitudinal one.
The potential planes outside and inside the tubes are defined by metallic strips (0.1 mm wide, pitch 3 mm) on the inside and the outside surfaces of the drift tubes; metallic strips mounted on the liquid radiator tubes and a wire frame at the mirror side of each drift tube.
All this strips and wires are carefully positioned to coincide in planes perpendicular to the longitudinal axis of the tube (i.e.the drift direction).

The top and bottom walls consist of 4 quartz plates being glued together side to side, while the side wall each consist of 3 plates.
Each strip is made out of three layers : 20 nm Cr, 200 nm Cu and again 20 nm Cr; their width is, on the top and bottom walls, 0.1 mm and 0.5 mm on the side walls.
The pitch of the strips is 3 mm. A conductive glue is used to connect the strips to the joint of the bitube. Apart from shaping the electric drift field, the strips also reduce the building up of surface charges. The electron attenuation length is about 10 m and the drift deviations over the whole 1.5 m drift is about $2-3$ mm.

4.6 The Liquid Radiator

The Liquid radiator boxes consists of trays made of composite materials, closed by a 4 mm thick UV transparent quartz window, facing the photon detector.
They are 150 cm long and 34 cm wide, with an internal hight of 1 cm.
The Liquid radiators are filled with Liquid Freon, where charged tracks perform the Cherenkov effect, radiating on average 12 photoelectrons per track.
Two radiators are glued together and form one mechanical unit. The radiating medium is a 1 cm thick Liquid layer, with a refractive index of $n = 1.274$ at $\lambda = 175$ nm.
The outer quartz surface of each radiator is equipped with metallic, 130 μm wide strips along the $r-\phi$ direction (the pitch in z is 6 mm). They are interconnected by a resistor chain, therefore contributing to the definition of the global electric drift field shape.

4.7 The Gas Radiator

The whole space between the BRICH elements is filled by the gas Freon (C_5F_{12}), for a total of about 24 m^3.
The main gas volume to perform the Cherenkov effect has a thickness of 40 cm, extended 150 cm along z. Photons created by Cherenkov effect along the whole particle path between the drift tube and the parabolic mirrors are reflected backwards by them on to the photon detector. The mirrors focal plane is situated just inside the drift tube, where the Cherenkov photons allow the reconstruction of the signal ring image (in the gas, on average 8 signal photoelectrons are expected).
An important effect due to the track's curvature (under the effect of the DELPHI 1.2 Tesla magnetic field) is the spread out of the ring image collected, due to the wide spread of the possible original photon emission points. Since the trajectories are sometimes curved, the ring focusing mirror geometry does not work perfectly. For low momentum tracks (especially electrons, below 3 GeV/c in momentum) this is an important effect to take into account.
The boiling point at atmospheric pressure of Gas Freon is at 28° C : therefore the entire detector volume is kept by the heating system at 40° C, well above it, to avoid condensation.

4.8 The MultiWire Proportional Chambers

The Barrel RICH disposes of a total of 48 Multi Wire Proportional Chambers to perform the electronic read out of the drifted electrons signal.
Each MWPC (figure 4.5) is mounted in front of the corresponding drift tube. Each chamber contains 128 anode wires (along the radial direction, with a pitch of 2.62 mm in $r\phi$, a diameter of Ø 20) and 16 strips (directed along $r\phi$, pitch 4 mm in r, width 3.8 mm). The strips are further subdivided along $r\phi$ into 8 blocks of 16. Single photo-electrons develop avalanches at the anodes containing an average of $2 \cdot 10^5$ electrons which leads to a detectable signal. Small blinds (so-called 'cloisons') between the individual wires absorb UV-photons which are produced in the avalanche process because they in turn may produce unwanted (photon feedback) electrons.

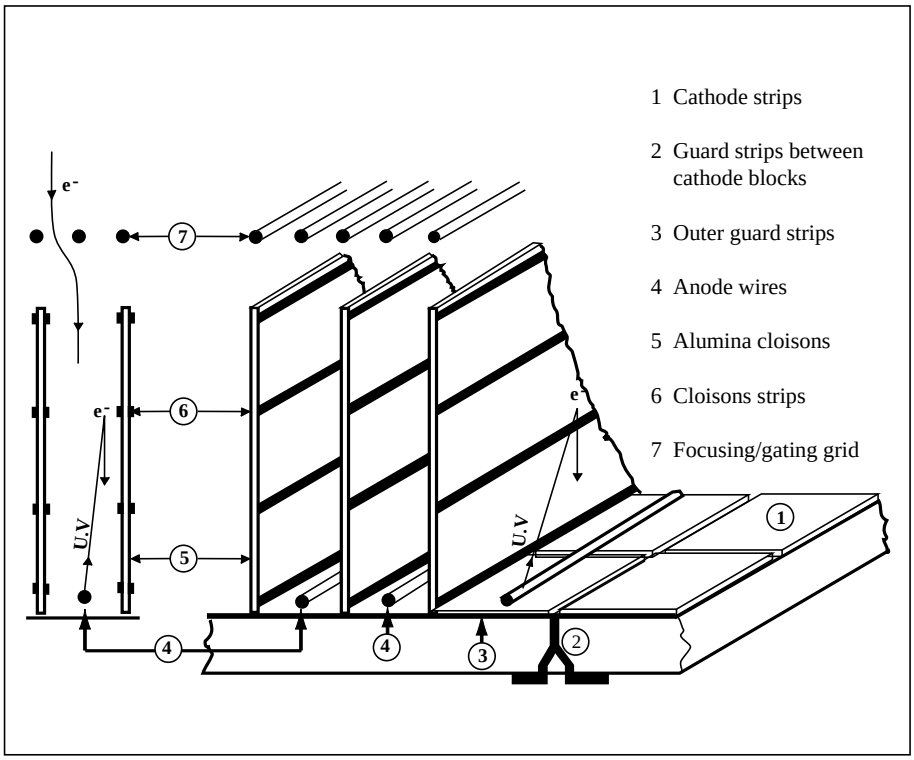

Figure 4.5: *A Barrel RICH Multi Wire Proportional Chamber (MWPC).*

4.9 The Mirrors

Every bitube module of the Barrel RICH contains 6 Parabolic mirrors (288 in total). They have been produced using a specially developed slumping technique [53], followed by vacuum deposition of a 50 nm thick layer of Al and a 30 nm thick protective layer of MgF_2.
The reflectivity for UV light is above 90 % in the wavelength range $\lambda = 165 - 230\ nm$. The mirrors are mounted on mirror cages concentric with the Barrel RICH, using the end flanges

as support. The focal lengths vary from 401.0 mm for mirror n.1 (close to the midwall) to 376.6 mm for mirror n.6, close to the Multi Wire Proportional Chamber. The positioning and the tilt angle of the mirrors is such that the gas radiator photons are reflected normally to the surface of the photon detector, thus optimizing the photon transmission.

4.10 The Calibration system

The Calibration system plays the fundamental role of monitoring the drift speed permanently during the detector running (it has been experimentally proved that it has a strong sensitivity to the global gas pressure of the detector : small fluctuation in pressure cause immediate fluctuations in the drift speed). Most of the possible systematics effect of the BRICH are therefore overcome by this monitoring. The bitubes are connected to a UV light source (a trigger-pulsed UV lamp) through optical fiber cables. They end up normally to the quartz box of the drift tubes, at 5 different position along the drift direction (z)
(5 rows, each of 9 optical fibers).
The length of the fibers is such that the light arrives simultaneously on the drift tube, to all points, generating photoelectrons. By measuring their drift time one gets an independent measure of the detector drift speed and an indication of possible deformations in the drift field geometry. The UV lamps are triggered 5000 times allowing the monitoring of the data acquisition and detection system. The typical drift velocity is about 5.15 $cm/\mu s$.

4.11 Cleaning, monitor, alignment and identification performances

In this section some aspects concerning the RICH identification characteristics are discussed, namely the problem of the cleaning of the data, the alignment procedure and its global overall identification performances.

4.11.1 Cleaning of the electronic signal

The drift of the signal photoelectrons along the 1.5 m bitube needs an accurate reduction of the background sources polluting the signal itself.
The amount of electrons whose coordinates are measured at the raw level at the end of the drift can be of several hundreds, while only 10-20 are the expected signal photoelectrons. The electronic read-out provides therefore (at the raw level, before any hardware or software cleaning) an "electronic picture" of the signal detected by the photon detector, containing, among the few ring signal electrons, a big part of noise. Therefore electronic cleaning plays a fundamental role in the practice of the RICH technique associated to drift TPC-like tubes and Multi Wire Proportional Chambers (the most recent experimental tendencies [59] are more oriented towards the combined use of radiators with solid state Cesium-Iodide (CsI) photon detectors).
The main sources of noise [61] are the following :

- **Delta rays.** High energetic ionization electrons are produced by tracks crossing the drift tubes. They are easy to recognize and remove given the straight line image produced on the photon detector. Removed rejecting (normally) 4 consecutive wire hits separated by a time difference smaller than (normally) 11 LTD (Lep Time Digit, 1 $LTD = 8.518\ ns$).

- **Ionization electrons.** Ionization (dE/dx) photoelectrons are produced by the passage of the charged particles through the drift tube and form accumulations of reconstructed space points. They are eliminated for known tracks ($p > 0.7\ GeV/c$) by the rejection of all the hits in a cylinder of 1 cm radius around the track. For other tracks they are rejected by the suppression of the accumulation points, that is of all hits in a sphere of radius 1 cm. Also point with a strip multiplicity bigger than 3 are rejected at the same purpose.

- **Feedback photoelectrons.** These are created during the avalanches around the anode wires. Usually identified by a cloud of points behind the δ-rays.

- **Electronic Noise.** It is generally induced by the LEP machine and other DELPHI detectors. It can be identified and eliminated because it induces signal on several hits simultaneously, both on anode wires and cathode strips of the MWPC. Easily rejected by the cut of 5 hits or more in a time interval in within 1 LTD (that is 0 LTD counts).

- **Electronic Oscillations.** Oscillations are electrically induced by large charges, observed in the chambers or the discriminators. They are characterized by several consecutive hits in the same electronic channel, normally separated by a time distance corresponding to the read-out dead time.

- **After-Pulses.** They are produced by the tail of the signal pulses, superimposed on the background fluctuations; they appear normally after the dead time.

- **Cross-Talk** Cross-Talk between cathode strips is induced by large charges. It is observed on cathode strips (and not on wires) given their high electronic capacity.

- **Other ring in the neighbourhood.** The case in which two (or more) tracks are so close to each other that other rings in the neighbourhood disturb the signal of a track happens rarely, but happens. A part of this background can be reduced by a clustering procedure in the $r - \phi$ space around the track volume, rejecting space points too close to each other in $r - \phi$ (since the Cherenkov signal is expected to be uniform in this coordinate).

In DELPHI therefore front-end (hardware) and software background rejection is applied, rejecting on average 70 % of the background and only 15 % of the signal. The same effects are taken of course into account to fine tune the detector simulation, in the MonteCarlo data

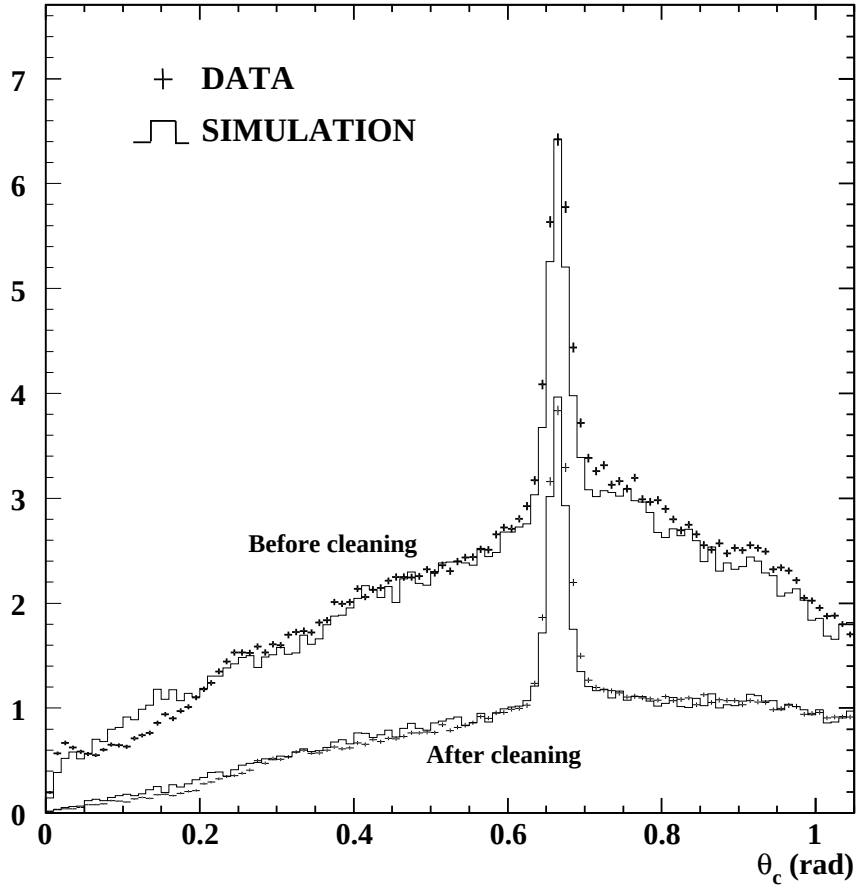

Figure 4.6: *Cherenkov Angle before and after the cleaning, Liq.Rad.($p > 6$ GeV/c)*

sets.

Figure 4.6 shows the Cherenkov angle distributions for the Liquid radiator, for particles with momentum in the saturated region ($p > 6$ GeV/c), before and after the cleaning, compared with the simulated distributions.

4.11.2 Alignment of the BRICH detector

To optimize the detector performances it is crucial to minimize all possible contributions to the spread, the imprecision contributions to the determinations of the Cherenkov angle. At this purpose a rather structured software procedure to align all the detector components in order to minimize unwanted residuals due to misalignment has been developed. The total number of components is given by 48 drift tubes, 48 liquid radiators, 48 mid-wall mirrors and 288 gas radiator mirrors : this means that about 900 geometrical parameters (relevant for the precise reconstruction of the Cherenkov Angle) have to be aligned. A detailed program called ERA [60] has been developed at this purpose. ERA uses a χ^2 minimization procedure

to minimize the function

$$\chi^2 = \sum_1^N \frac{(\Theta_C^{measured} - \Theta_C^{expected})^2}{\epsilon^2} \tag{4.6}$$

running upon selected samples of tracks (Selected Two Prong events, $Z \rightarrow \mu^+\mu^-$ or $Z \rightarrow \tau^+\tau^-$, Bhabha scattering), with saturated Cherenkov angle in both radiators and an easy tracking 2 prong topology.
ϵ is the expected error on the Cherenkov angle. When important detector parameters like the drift velocity, the read-out timing, the refractive indices of the radiators, the transmission radiators coefficient are known with high accuracy, the χ^2 can be minimized by slightly changing all the xyz and angular orientation coordinates of the detector components (shift, rotations, z dependent shift). The result of the alignment procedure is then written in the DELPHI RICH database.

It is shown in figure 4.7, showing the resolution in the gas radiator before and after the

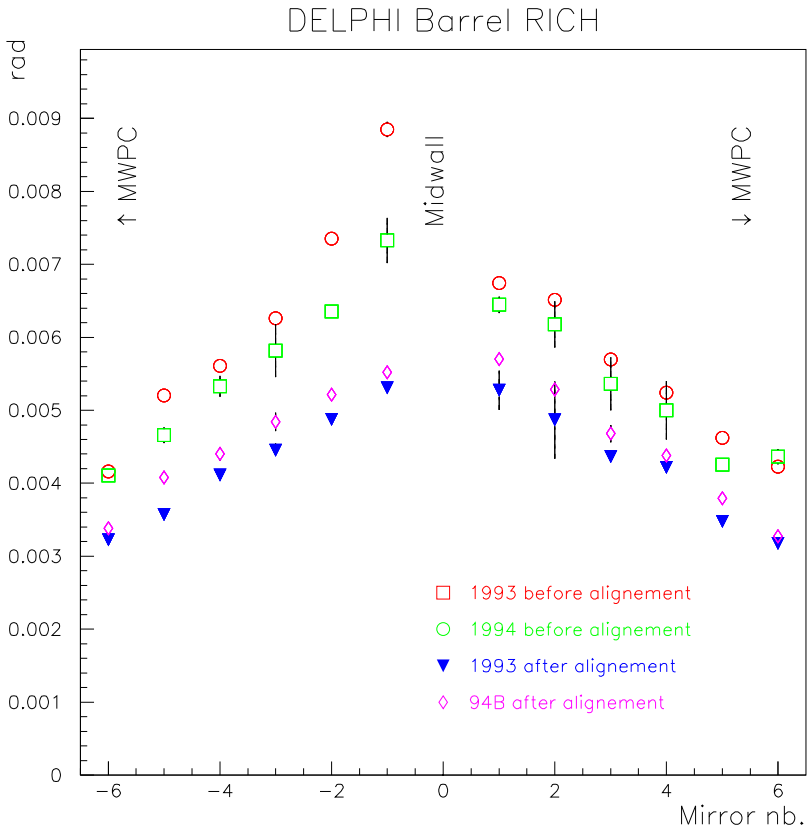

Figure 4.7: *Cherenkov angle resolution in the gas before and after the alignment.*

detailed ERA alignment procedure for data 1993 and 1994.

4.11.3 Identification Performances

The overall BRICH identification performances depend dramatically on the resolution on the reconstructed Cherenkov Angle in both radiators. In chapter 6 the effect of the particular algorithm used to measure the Cherenkov angle is reported. Here the nominal results after the alignment procedure are summarized in table 4.3.

To show how powerful can be a RICH detector in performing particle identification, the

	BRICH Liquid	BRICH Gas
Number of photoelectrons per track	14	8
Saturated Cherenkov angle (mrad)	666	62.3
resolution per photoelectron (mrad)	13.3	4.3
resolution per track (mrad)	5.2	1.5

Table 4.3: *Numbers of signal photoelectrons, Cherenkov saturated angles and resolutions obtained in $Z \to \mu^+\mu^-$ events, for the Barrel RICH.*

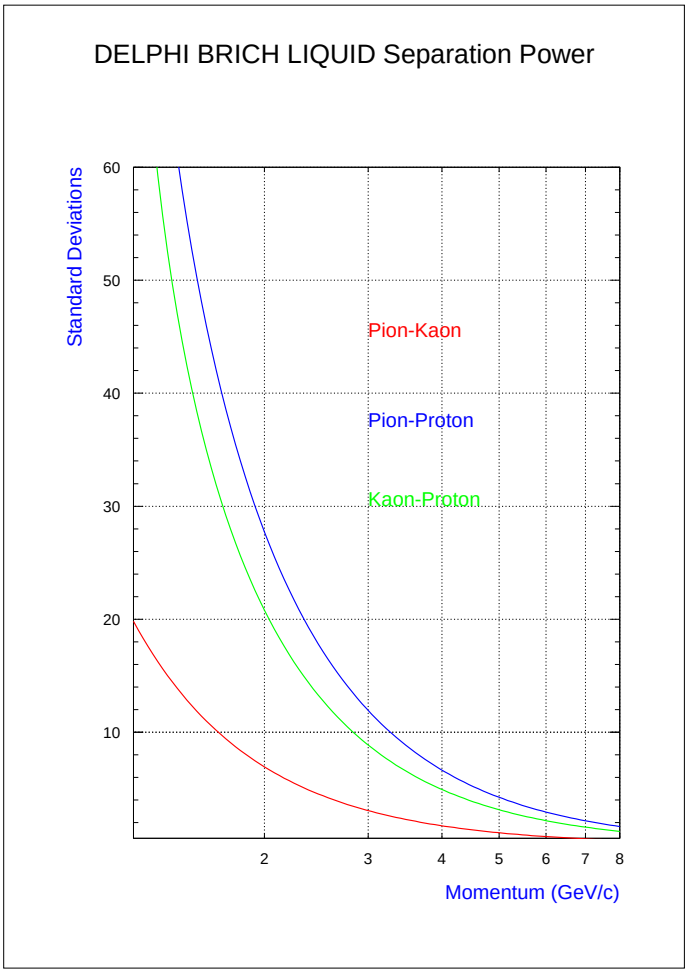

Figure 4.8: *Nominal Separation Power for the BRICH Liquid*

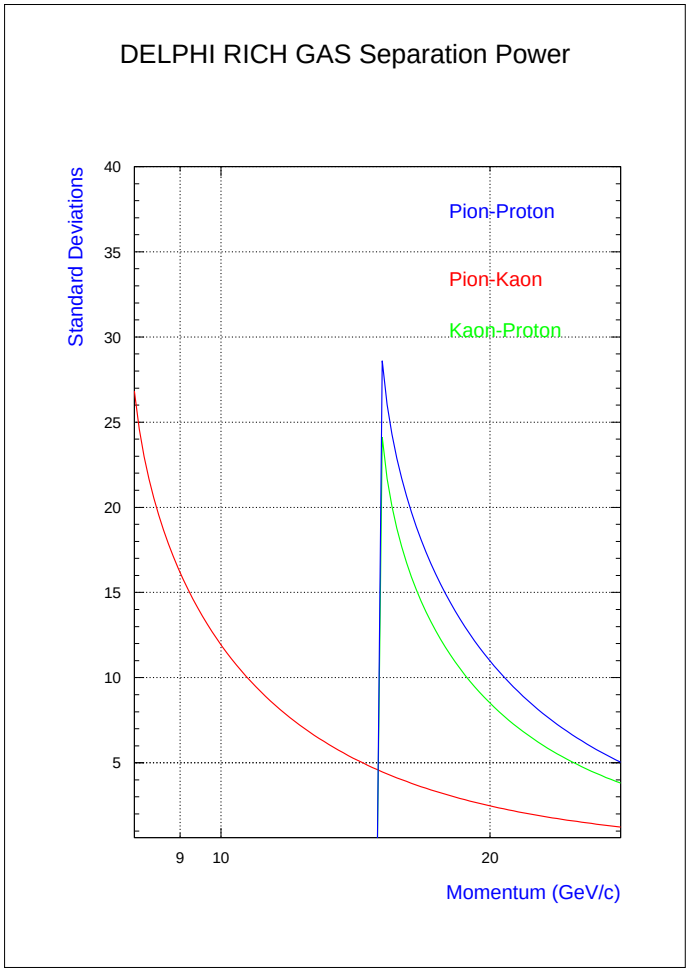

Figure 4.9: *Nominal Separation Power for the BRICH Gas*

nominal separation power of both the Liquid and Gas Barrel RICH detectors are shown in fig.4.8 and 4.9 : the separation power for the three hadronic flavour (π^+, K^+ and p) is given in units of standard detector resolutions as a function of momentum. They corresponds to a single track Θ_C resolution of 5.2 *mrad* in the Liquid radiator and 1.9 *mrad* in the Gas radiator. These are the values corresponding to the error on the mean Cherenkov angle for saturated tracks as provided by the RIBMEAN package (see chapter 6).

Chapter 5

The Time Projection Chamber

The Time Projection Chamber is the central tracking detector of the DELPHI experiment. It provides the so called "Track Elements", allowing the fit of the charged particle trajectories under the magnetic field. The TPC can provide a measure of the stopping power (dE/dx) for charged particles, performing therefore particle identification as well. In this chapter a general description of the TPC is given, focusing on the its characteristics relative to the particle identification power.

5.1 General Description

The TPC is a cylinder of 2x1.3 m in length, situated between the radial positions 0.29 m and 1.22 m from the beam axis. The two drift volumes are separated by a High Tension plate (20 kV), producing an electric field of 150 V/cm. A charged particle crossing the TPC produces by ionization around 70 electrons per cm of gas. Under the action of the electric field these primary electrons drift in the direction of the proportional chambers (6 at each TPC extremity).

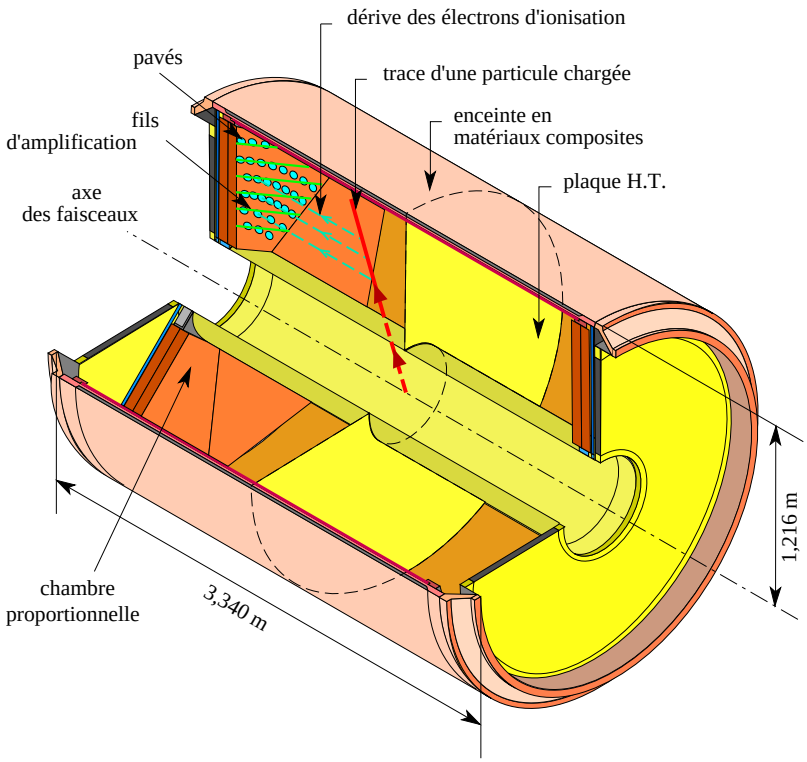

Figure 5.1: *The DELPHI TPC detector.(see below)*

derive des electrons d'ionisation	: ionization electrons drift
trace d'une particule chargee	: charged particle track
enceinte en materiaux composites	: composite material vessel
plaque H.T.	: High Tensions plate
paves	: pads
fils	: wires
chambre proportionelle	: proportional chamber
axe des faisceaux	: beam axis

The TPC Vessel is made out of Carbon fiber, built to stand vacuum, filled with a mixture of Ar (80%) and CH_4 (20%), kept at atmospheric pressure. The vessel contains an electric cage consisting of copper strips (3 mm wide, separated by 1 mm) on a kapton foil, glued on both sides of two cylindrical epoxy skins defining the inner and outer electric cages. The electric field is set through a central high voltage plane at 20 kV. A chain of 333 high precision 4 $M\Omega$ resistors connecting the copper strips defines a homogeneous field of 150 V/cm over the whole drift volume.

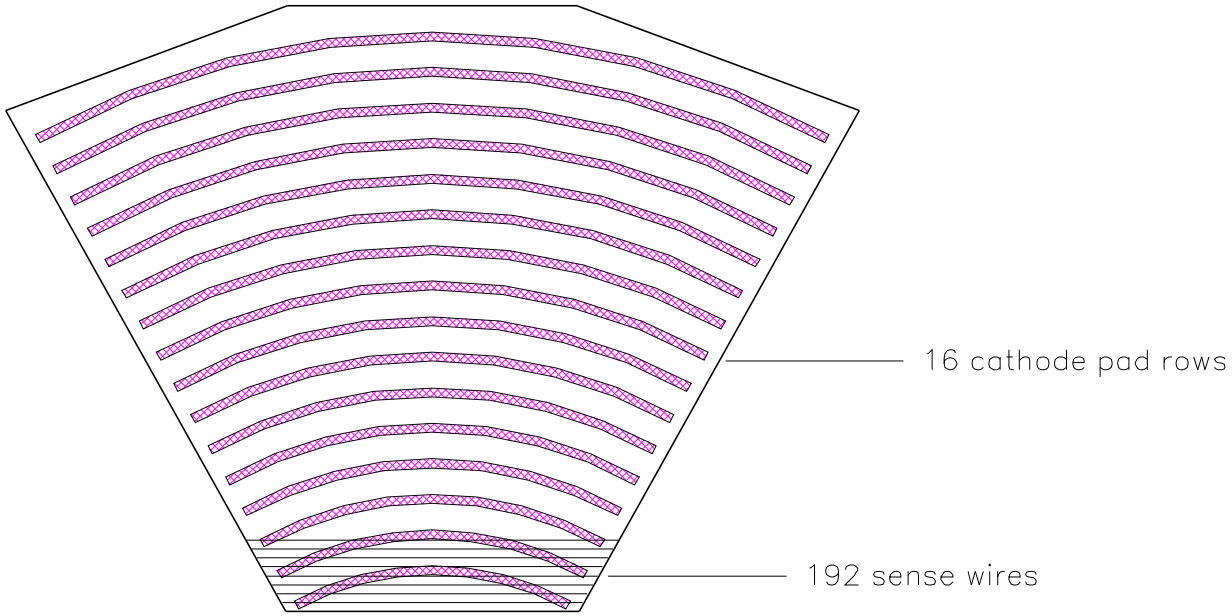

Figure 5.2: *One of the DELPHI TPC modules*

active length	$2 \times 134\ cm$
active radius	32.5-116 cm
detector volume	14 m^3
working pressure	1 Atm
gas mixture	80% A_r 20% CH_4
gas temperature	$\sim$ 29° C
number of dE/dx samples	192
number of $r\phi$ points	16
drift speed of primary electrons	7 cm / μs
drift field	187 V/cm
sense wires spacing	4 mm
sense wires diameter	20 μm
sense wires high voltage	1435 V
magnetic field	1.23 T

Table 5.1: *The DELPHI TPC main characteristics.*

5.2 The TPC Multi Wire Proportional Chambers and Read out

Each one of the two TPC circular end-caps is subdivided in 2 $\times$ 6 proportional chambers.
The *TPC* Multi Wire Proportional Chambers consist of a triple layer of wires included in a 1 cm tick box. The first wire plane is a gating grid to address the drift, the second one is a cathode plane defining the end of the drift area, the last one (the closest to the Anode Pad, kept at +1430 V) is the 192 sensitive wires plane, collecting the track's ionization.
The wires have a diameter of 20 μm, with a pitch of 4 mm, interspersed with field wires.
The anode sense wires are set to a high voltage of 1435 Volts. A gap of 4 mm separates the sense wire plane from the rigid structure of the chambers, covered by a cathode copper plate, on which 16 circular rows of capacitive pads are engraved.
The surface of each pad is constant (52.5 mm^2), and the number of pads per row (from 64 to 144) is kept a multiple of 16 for read-out convenience, which implies different pad widths.
The rows are distant 4.5 cm from each other, centered at the TPC axis, at a distance from 40 to 140 cm from the axis.
There are 1680 pads per sector, for a total of 22464 channels to be read out.
The Electronic read out is performed by hybrid pre-amplifiers located inside the vessel, and their signal are sent, through 30 m long cables, to FASTBUS crates in the control room.
The charge signal collected by pads and wires is first translated into an electronic signal by preamplifiers, and then, in the *FASTBUS* crates, is shaped gaussian with a 250 ns width, keeping its integrated size, and digitized.
The ADC provide therefore the time of arrival of the electric signal (from which the z coordinate is extracted : this is the "Time Projection" technique) and the total amount of the signal itself (dE/dx information).

5.3 Measure of the specific ionization (dE/dx)

The Proportional Chambers are called like this because of their proportionality in the total collected charge as a function of the applied voltage. By working in this linear *regime* are used to measure the energy loss of the charged particles produced in DELPHI. A charged track produces on average 70 electrons per centimeter while crossing the TPC.
The energy loss of moderately relativistic charged particles (other than electrons) in matter is given by the *Bethe – Bloch* formula :

$$\frac{dE}{dx} = Kz^2 \frac{Z}{A}\frac{1}{\beta^2}[\frac{1}{2} ln \frac{2m_e c^2 \beta^2 \gamma^2 T_{max}}{I^2} - \beta^2 - \frac{\delta}{2}] \qquad (5.1)$$

In this formula β and γ are the relativistic kinematical parameters of the particle, m_e is the electron mass $[\frac{MeV}{c^2}]$, A is the mass number of the material, I is its ionization potential in $[MeV]$ (According to the Thomas-Fermi model $I_{[eV]} \simeq 12Z$, $Z =$ atomic number), T_{max} is the maximum kinetic energy transfer from the particle of mass M to an electron in a single collision ($T_{max} = 2m_e c^2 \beta^2 \gamma^2 / (1+2\gamma\ m_e/M) \simeq 2m_e c^2 \beta^2 \gamma^2$ for $\frac{2\gamma m_e}{M} << 1$) , $K = 4\pi N_A r_e^2 m_e c^2$ (r_e is the classical electron radius, 2.818 fm) and δ is the *density effect* correction factor.
In the case of the DELPHI TPC, the final dE/dx measurement written on the DSTs comes from the averaging of the 80% lowest amplitudes associated to a given track. This is done in

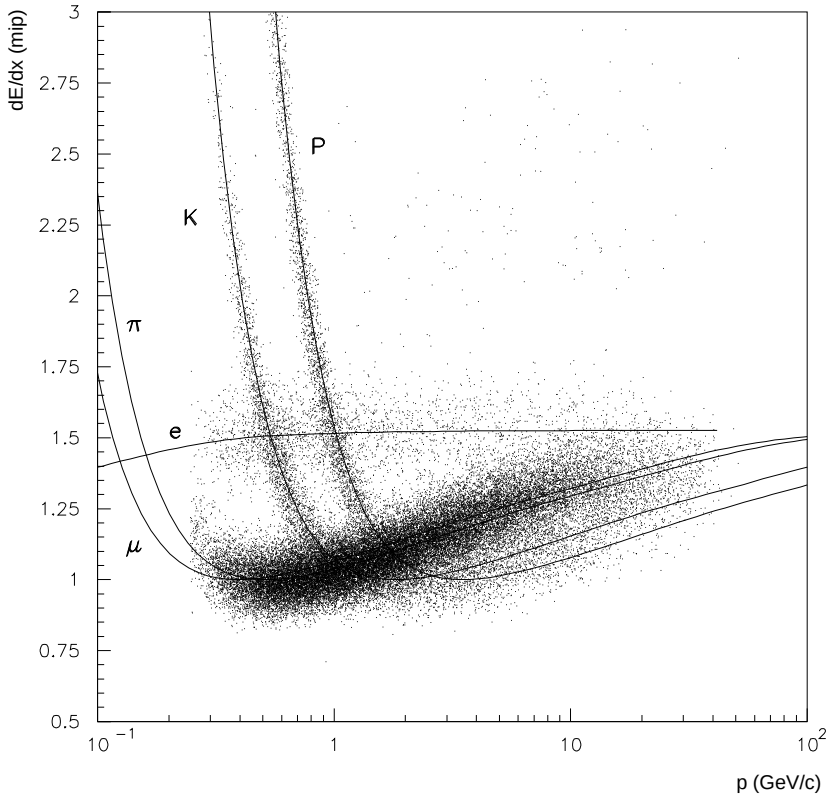

Figure 5.3: *Behaviour of the stopping power as measured by the DELPHI TPC.(from PPE/95-194)*

order to avoid an excessive rise in the Landau fluctuations for the highest amplitudes and to exclude the saturation region for the chamber in which the dE/dx measurement is wrong. To this number many successive corrections are applied :

- A normalization (to 4 mm) to take into account different path lengths due to different incident track angles
- A correction for the bias induced by the truncation procedure
- A drift distance correction in the case the electronic shapers are not used, to take into account the deformation of the electronic signal during the drift
- A track separation rejection of clusters separated by less then 2 cm in z
- A parameterized correction for the loss of efficiency corresponding to the radial edges of the TPC sectors.

Chapter 6

Charged Hadron Identification

In this chapter a general overview of the DELPHI charged hadron identification through the RICH and TPC detectors is given.
The identification of charged hadrons is performed merging the information coming from the $RICH$ and the TPC detectors, to extend the available momentum range and to provide a cross for the information coming from the two detectors. In this chapter the RICH identification is described together with the way the TPC (dE/dx) is used to measure the RICH identification performances and to complement the RICH information.

As we mentioned in chapter four, the physical information output coming from the RICH detector relative to a charged track crossing the detector is a given photoelectronic distribution : on average in DELPHI hadronic events roughly up to 100-120 photoelectrons are detected after the on line noise reduction for cross-talk, delta rays, feedback photoelectrons (produced during avalanches in the MWPC), electronic noise and oscillations.
The position on the photon detectors of these photoelectrons is recorded on the full DSTS (data summary tapes) and it represents the input to the identification tools.

6.1 Probabilities

One of the first ways [63] in which particle identification through the RICH detector has been implemented in DELPHI is by means of Tagging Probabilities for charged tracks. These probabilities are calculated by a Maximum Likelihood Technique, starting from a given track's photoelectronic distribution.
Identification probabilities are calculated by the standard DELPHI analysis program (DELANA) [42] and written on the DELPHI data tapes (Data Summary Tapes, DST) [43].
The program starts accepting all detected photons in a three standard deviation window around each expected angle for the five (e, μ, π, K, p) mass hypothesis for a track of a given measured momentum.
For each mass hypothesis (h) , the Cherenkov angle θ^h and the expected number of photoelectrons are known (see eq 4.4).

For any observed photon at the angle θ_i the probability density can be written as

$$\mathcal{P}^h(\theta_i) = N^h \frac{e^{\frac{-(\theta_i-\theta^h)^2}{2\sigma_i^2}}}{\sqrt{2\pi}\sigma_i} + B^h \frac{J\theta_i}{\int_{min}^{max} J\theta d\theta} \tag{6.1}$$

In this equation σ_i is the error on the single photoelectron (i) Cherenkov Angle (typically $\sigma_i \simeq 14\ mrad$ in the liquid radiator and $\sigma_i \simeq 7\ mrad$ in the gas radiator).
B^h is the fitted background contribution to the observed photoelectronic distribution, assumed to be flat in the angle itself, and therefore proportional to the angular interval between θ_i^{min} and θ_i^{max}.
J is the Jacobian of coordinate transformation from the *track* reference frame to the $\rightarrow$ detecting *phototube* frame.
The likelihood function is therefore given by the expression

$$\mathcal{L} = \frac{1}{n!}\{\prod_{i=1}^{n} \mathcal{P}^h(\theta_i)\} exp(-N^h - B^h) \tag{6.2}$$

where n is the number of observed photoelectrons and $exp(-N^h - B^h)$ represents an approximation for the empty cells ($i = n+1 \cdots k$) probability term given by

$$\prod_{i=n+1}^{k} (1 - \mathcal{P}(\theta_i)) \tag{6.3}$$

N^h and B^h are fitted terms corresponding to signal and background for each hypothesis h.
Maximizing the probability to have detected the observed photoelectronic distribution (that is maximizing this likelihood function) one gets the unknown parameters, that is the five probabilities for the mass hypothesis and the five background terms. These probabilities are normalized to one and written on the DSTs, to allow particle identification.

6.2 HADSIGN: merging dE/dx and Cherenkov information

HADSIGN has historically been the first program built in DELPHI for charged hadron (K^+ and p) identification.
It sets separated identification flags according to the RICH and the dE/dx information and combines the two set of flags to define a loose, standard and tight tag for K^+ and p.
The momentum axis is split into different regions according to the expected Cherenkov behaviour (Signal or Veto Region for π^+, K^+ and p) and dE/dx requirements and according to them K^+ and p are tagged cutting on the number of photoelectrons and the DELANA probabilities

In table 6.1, as an example, the list of requirements is shown for the HADSIGN standard proton tag as a function of momentum.

momentum range (GeV/c)	RICH requirements	(dE/dx) requirements
$0.7 < p < 1.2$	$n.ph.el.liq. > 4$ $\mathcal{P} > 0.3$	$(dE/dx) > 1.$ $1 < ((dE/dx) - (dE/dx)^{exp.K})/\sigma < 3$
$1.2 < p < 9$	$\mathcal{P}^p + \mathcal{P}^K > 0.8$ $n.ph.el.gas < 20$	$(dE/dx) > 1.1$ $1 < ((dE/dx) - (dE/dx)^{exp.K})/\sigma < 3$
$9 < p < 16$	$\mathcal{P}^p/(\mathcal{P}^p + \mathcal{P}^K > 0.5$ $\mathcal{P}^p > 0.4$ $n.ph.el.gas < 20$	$(dE/dx) > 1.2$ $1 < ((dE/dx) - (dE/dx)^{exp.K})/\sigma < 3$
$p > 16$	$\mathcal{P}^p > 0.2$ $n.ph.el.gas > 40$	$(dE/dx) > 1.2$ $1 < ((dE/dx) - (dE/dx)^{exp.K})/\sigma < 3$

Table 6.1: *RICH and dE/dx tagging cuts applied as a function of momentum for the HADSIGN standard kaon tag. The number of photoelectron is intended in within 3 σ from the kaon hypothesis*

6.3 RIBMEAN algorithm

In the RIBMEAN [41] algorithm, the one used to perform this analysis, an iterative clustering procedure is applied to select a subsample of photoelectrons to calculate the average Cherenkov angle for a charged track in the signal region and to perform hadronic tagging . Starting from the raw information on the full DSTs, (roughly 80-100 photoelectrons per hadronic event) , the program performs a cleaning of the RICH data, a rescaling of the error, a run selection.
The calculation of the mean Cherenkov angle is performed in the following way :

- A clustering length d in the Θ_C axis is set to a small value of some milliradiants and cluster of photoelectrons in within d are grouped together into different clusters.
- In each cluster the average Cherenkov angle $\overline{\Theta_C^{clus}}$ is calculated by a Gaussian fit.
- Drop the ambiguous photoelectrons, that is eliminate in each cluster the photoelectrons giving the highest contribution to the χ^2 of the fit.
- Make the clustering length d bigger and iterate the process (by clustering the photoelectronic distribution again) until ending up with only one cluster.
- Calculate then the average Cherenkov angle for the survived Cluster according to the formula

$$\overline{\theta} = \sum_i \frac{\frac{\theta_i}{\sigma_i^2}}{\sum_i \frac{1}{\sigma_i^2}} \tag{6.4}$$

6.4 RINGSCAN algorithm

RINGSCAN is a maximum likelihood based algorithm measuring an unbiased mean Cherenkov angle. The method is unbiased in the sense that it does not make use of any apriori assumption on the expected angular (photoelectronic) acceptance region for the five different mass

hypothesis.
RINGSCAN divides the spatial acceptance region (for each track) in multidimensional cells. If k is the total number of observed photoelectrons for a given track, and H is the probability to observe 1 photoelectron in cell i, the probability to observe j photoelectrons in cell i is given by

$$\mathcal{P}_j = b_k^j H^j (1-H)^{k-j} \tag{6.5}$$

where b_k^j are the binomial coefficients $b_k^j = k!/(j!(k-j)!)$.
In the case k is Poissonian distributed with average count M on gets :

$$\mathcal{P}_{j,k} = \frac{M^k}{k!} e^{-M} b_k^j H^j (1-H)^{k-j} \tag{6.6}$$

The method assumes that signal and background are distributed according to the two functions $B(\theta,\phi)$ and $G(\theta,\phi)$ and that the number of detected photoelectrons for these two categories follow the Poisson distribution with mean values N and K respectively. In this hypothesis the probability to observe n photoelectrons (signal (m) and background (l) : $l = n - m$) is given by

$$\mathcal{P}_n = \sum_{m=0}^{n} \frac{e^{-NG}}{m!}(NG)^m \cdot \frac{e^{-KB}}{(n-m)!}(KB)^{n-m} \tag{6.7}$$

This is equivalent to a Poisson distribution with mean value $NG + KB$:

$$\mathcal{P}_n = \frac{(NG+KB)^n}{n!} e^{-(NG+KB)} \tag{6.8}$$

For each mass hypothesis (h) the total probability is then given by the product on all the angular cells

$$\mathcal{P}^h = \prod_{i}^{cells} \{ \frac{(N^h G_i + K^h B_i)^{n_i}}{n_i!} e^{-(N^h G_i + K^h B_i)} \} \tag{6.9}$$

where n_i is the number of observed photoelectron in cell i and B_i and G_i are the background and signal distribution relative to the its angular position.
For small enough angular cells one can neglect the terms corresponding to more than one photoelectron in the same cell and reorganize the sum into

$$\mathcal{P}^h = \prod_{j=1}^{n} \{ (N^h G_j + K^h B_j) \} e^{-(N^h + K^h)} \tag{6.10}$$

obtaining therefore the same expression got for the DELANA probabilities 6.1 and 6.2.
Taking the conversion length (l) for the photons in the drift tube into account, for each hypothesis h, the probability distribution for signal and background are given by

$$G(\theta,\phi,l) = \frac{r\ sin(\theta)\ d\theta\ d\phi\ dr\ e^{-\frac{(\theta-\theta^h)^2}{2\sigma^2}} e^{-l/l_0}}{\int_{\theta_1}^{\theta_2} sin(\overline{\theta})\ e^{-\frac{(\overline{\theta}-\theta^h)^2}{2\sigma^2}} d\overline{\theta}\ \int_{\phi_1}^{\phi_2} d\overline{\phi} \int_{r_1}^{r_2} \overline{r} e^{-l/l_0}\ d\overline{r}} \tag{6.11}$$

$$B(\theta,\phi,l) = \frac{r\ sin(\theta)\ d\phi\ d\theta}{\int_{\theta_1}^{\theta_2} sin(\overline{\theta})\ d\overline{\theta}\ \int_{\phi_1}^{\phi_2} d\overline{\phi} \int_{r_1}^{r_2} \overline{r}\ d\overline{r}} \tag{6.12}$$

In these formulae r is the total distance from the track crossing point in liquid radiator to the conversion point in the drift tube, $l = r - r_1$ is the path in the drift tube along the photon direction covered by the photon before its conversion into electron, r_2 is the distance between the track crossing point in the liquid radiator and the end of the drift tube along the photon flight direction. l_0 is the TMAE (in the drift gas) absorbtion length, $l_0 \simeq 2.0\ cm$.
ϕ_1, ϕ_2, θ and θ_2 are the polar angle and azimuthal angle of the observation region limits.

6.5 Other Cherenkov Angle reconstruction programs

Tracks above the threshold radiate photoelectrons allowing therefore the reconstruction of their Cherenkov Angle.
At this purpose the NNRIB and DETAL programs reconstruct the Cherenkov angle in the signal region, allowing to perform statistical analysis to measure the inclusive content of π^+, K^+, p and therefore giving the possibility to measure the efficiency and purity of identification tagging programs.
An example of the extraction of the inclusive hadronic amount from a triple Gaussian fit of the reconstructed Cherenkov (through the NNRIB algorithm) angle is shown by picture 6.1.

6.5.1 NNRIB algorithm

NNRIB is a triangulation geometrical Technique to reconstruct a given track's Cherenkov angle in the signal region, above the light threshold.
The algorithm is based on the reconstruction of a ring from 3 photoelectrons and the construction of the distribution of the possible centers for all the given triplets of photoelectrons. Given n detected photoelectrons, the number of possible triplets defining a ring (and therefore a center) is given by $n(n-1)(n-2)/6$. For every possible set of three photoelectrons, the radius of the corresponding circle is evaluated.
Signal photoelectrons from the Cherenkov Ring tend to distribute normally accumulating on a Gaussian, while background photoelectrons are flat in the radial space. The radial distribution is fitted with a Gaussian and a linear background and the mean radius is extracted; correspondingly the mean Cherenkov angle is calculated.

6.5.2 DETAL algorithm

The name DETAL stands for DETerministic ALgorithm. The Mean Cherenkov Angle is calculated trough a successive, step by step minimization of the difference between the number of photons above and below the central value at each step, seeing the calculation of the mean Cherenkov angle as an general optimization problem. At each step the considered acceptance angular interval in θ is reduced to one half of the value at the step before. To correct for the background, a correction factor for the definition of the number of photoelectrons above and below the mean value is taken; it is proportional to the surface of the corresponding annular region, therefore proportional to θ_C^2.

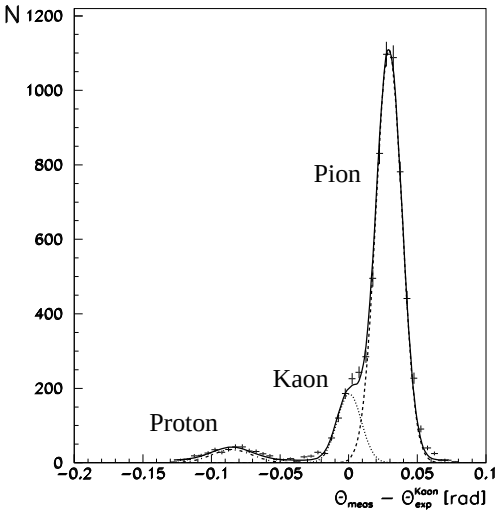

Figure 6.1: *Fit of the* $\theta - \theta_k^{exp}$ *distribution in the momentum range* $2.0 - 2.5$ GeV/c *in the liquid radiator.* Θ_C *is reconstructed through the NNRIB algorithm.*

The iterations are stopped when the difference between two successive mean angles is smaller than 1 $mrad$ in the Gas and 2 $mrad$ in the liquid, defining a given θ_{final}.
Afterwards the weighted average (through the inverse squared of the error) of all Cherenkov angles θ_i corresponding to all photoelectrons in within $\theta_{final} - \theta_i < 3\sigma_{\theta_i}$ is taken as

$$\overline{\theta} = \frac{\sum_i \frac{1}{\sigma_{\theta i}^2}\theta_i^2}{\sum_i \frac{1}{\sigma_{\theta i}^2}} \tag{6.13}$$

This method, tested on $\pi^{\pm}$ provided a resolution on the mean Cherenkov angle of 3.2 $mrad$ in the Gas and 9.0 $mrad$ in the Liquid.

Chapter 7

The Analysis : hadronic and b quark flavour tags

7.1 Introduction

In this chapter the method used for the measure of the inclusive charged π^+, K^+ and p production in hadronic Z decays into light quark (u,d,s) and in heavy quark (b) events is described.
It makes use of the performances of the two main particle identification detectors (TPC and $RICH$) and of a life-time impact parameter topological tag ([65]) to select heavy quarks in order to enrich the heavy quark and light quark samples.
The working principles of both the hadronic flavour (π^+, K^+ and p) tagging program and the b quark tagging program are described and the general method used in the analysis is reported.

In the next section of this chapter (section 2) the structure of the hadronic identification (tagging) program for π^+, K^+ and p is described, focusing on the requirements applied to select tracks and on its performances in terms of efficiencies.

In section three the general working principle of the analysis is described, with the description of the analysis method and the main corrections applied.

In section four the $b\overline{b}$ tagging program is described, focusing on its performances and on its basic operating principles, its purity and its efficiency.

7.2 The π^+, K^+ and p identification tag

The particle identification program (tag) uses the dE/dx information at low momenta (0.3-1.3 GeV/c) and the RICH Cherenkov information at higher momenta.
In particular the π^+ and K^+ tag use dE/dx information up to 0.7 GeV/c and the p tag uses it up to 1.3 GeV/c.

momentum range (GeV/c)	dE/dx (M.I.P.)	n.wires	ABS(pull)
0.3 - 0.5	< 1.3 ($\pi^{\pm}$ *tag*)	> 70	< 3
	> 1.6 ($K^{\pm}$ *tag*)	> 70	< 1
	> 2.0 ($p\overline{p}$ *tag*)	> 70	< 3
0.5 - 0.7	< 1.2 ($\pi^{\pm}$ *tag*)	> 70	< 3
	> 1.3 ($K^{\pm}$ *tag*)	> 70	< 2
	> 2.0 ($p\overline{p}$ *tag*)	> 70	< 3
0.7 - 0.9	> 1.8 ($p\overline{p}$ *tag*)	> 70	< 2
0.9 - 1.3	> 1.25 ($p\overline{p}$ *tag*)	> 70	< 2

Table 7.1: *dE/dx tagging cuts applied in the low momentum region for different momentum ranges and particle flavors*

7.2.1 (dE/dx) tag

The dE/dx information used with respect to momentum for the three different tags is showed in table 7.1. If a given track's dE/dx in the accepted angular region satisfied the criteria listed in table 7.1, was tagged as π^+, K^+ and p respectively. Double tags have been avoided by excluding tracks with more than one flag to minimize the population of the off-diagonal elements of the efficiency matrix. The pull variable is defined as

$$pull = \frac{(\frac{dE}{dx}) - (\frac{dE}{dx})^{expected}}{\sigma_{\frac{dE}{dx}}} \tag{7.1}$$

7.2.2 ($RICH$) tag

At higher momenta ($p > 0.7$ Gev/c for π^+ and K^+, $p > 1.3$ GeV/c for p) a RICH-based identification program [64] has been applied to perform particle identification for pions, kaons and protons.
The tag cuts on different quantities like the number of measured photoelectrons and the measured Cherenkov angle in the liquid and in the gas.
It also requires, in the Cherenkov Angle signal region for a given hypothesis, the measured Cherenkov angle to be far apart from the other two hypothesis's angles of a minimal distance

in units of Cherenkov angle resolutions.
The tag is based on the output of the RIBMEAN package described in chapter 6.
Namely the Mean Cherenkov Angle reconstruction and the number of signal photoelectrons after clustering and background reduction.

Both liquid and gas radiators are operational for particles with momenta from 0.7 up to 45 GeV/c. For each radiator, the collected information can be separated in 2 different classes:

• *Liquid/Gas Signal* This applies to particle momentum windows where sufficient Cherenkov photons are measured and a ring is reconstructed. This means that the RIBMEAN clustering package found at least a minimum number of photoelectrons, with a minimum value for the Cherenkov angle.
For the liquid signal information, the minimum angle must be 0.25 radiants and the minimum number of photoelectrons is 4. In the Gas radiator case the corresponding values are 0.015 radiants and 2 photoelectrons. This is the so called "ring identification".

• *Liquid/Gas Veto*: Applies to momentum regions where for one - or more - hypotheses no signal is expected, i.e., the particle velocity is below the Cherenkov threshold. This is the so called "veto identification". Liquid veto is defined by a number of photoelectrons lower than 4 and gas veto lower than 2.
It is possible to distinguish between 4 different veto identification areas, one in the Liquid and three in the gas radiator, defined as follows :

- *proton liquid veto*: This corresponds to the momentum range under the kaon band, up to the proton threshold, corresponding to 1.3 GeV/c.
  Since both kaons and pions are in the signal region, requiring a liquid veto corresponds to a positive proton identification.
- *π-k-p gas veto*: the corresponding momentum range is below the pion gas threshold, that is below 2.3 GeV/c in momentum.
  In this region electrons still radiate photons so that requiring such a veto can be used to identify electrons to reduce their background in the kaon and proton liquid signal tag.
- *k-p gas veto*: (under the pion band up to the kaon threshold at 8.5 GeV/c). Pions can be removed by such a veto, so that this veto is used in both kaon and proton tags.
- *proton gas veto*: (under the kaon band up to the proton threshold at $\simeq$ 17.5 GeV/c).
  This is of course used to improve the proton positive identification, rejecting pions and kaons.

A detailed description of the tag can be found in [64].

7.2.3 Efficiency, Purity and (dE/dx) fits

The flavour tagging efficiency ϵ_k^k of a tagging program is defined as the number of tracks of flavour k actually tagged as k (that is called "k") divided by the total number of particle of flavour k in input to the program itself :

$$\epsilon_k^k \equiv \frac{\#(k \rightarrow \text{"}k\text{"})}{tot.\#\ k} \tag{7.2}$$

The corresponding purity P^k of the k flavour tag is defined as the number of tracks of flavour k actually called k by the tag divided by the total number of particles tagged as k :

$$P^k \equiv \frac{\#(k \rightarrow \text{"}k\text{"})}{tot.\#\ \text{"}k\text{"}} \tag{7.3}$$

Tagging efficiencies can of course be defined for the misidentification efficiencies (the off diagonal terms of the efficiency matrix for a given identification inclusive analysis) replacing the nominator of equation 7.2 by the number of particle of flavour k tagged as flavour i : $\#k \rightarrow \text{"}i\text{"}$:

$$\epsilon_k^i \equiv \frac{\#(k \rightarrow \text{"}i\text{"})}{tot.\#\ k} \tag{7.4}$$

In this convention, more generally, in this analysis equations 7.2 and 7.4 are taken into account by referring to ϵ_k^i as the i-tag efficiency for flavour k.
For example ϵ_k^π denotes the efficiency of the pion tag for kaons.

In an inclusive hadronic flavour analysis like this one, the knowledge of the identification ϵ_k^k and misidentification ϵ_k^i efficiencies plays a fundamental role.
In this analysis the efficiencies have been extracted by means of full detector simulation (montecarlo) data.
Anyhow, further information and cross checks about the values obtained from the montecarlo can be obtained using selected samples of tracks like pions, kaons or protons coming from (invariant mass) reconstructed decays. For example useful decays are $K^0 \rightarrow \pi^+ \pi^-$, $\phi \rightarrow K^+ K^-$ and $\Lambda^0 \rightarrow p \pi^-$. Anyhow in most of these decays, the decay products have a very limited spectrum in momentum, so that they can be used only for small, given ranges in momentum.
For instance protons and pions from the Λ can be used up to about $6-8\ GeV/c$ in momentum. Similarly for the pions from K^0.
Moreover in some cases the topology of the event induces biases in the RICH identification, like in the case of the kaons from the ϕ, where the angle between the two kaons is very small (of the order of some degrees), so that it can induce a bias in the RICH identification due to possible overlapping rings.
Another possible way in which the identification efficiency of a RICH (Cherenkov Information)

tagging program can be measured is through a statistical analysis of the dE/dx information on a given set of tracks. In other words one can use the dE/dx information provided by the TPC measurement as an independent check of the information coming from the RICH detector. For instance, on a given set of RICH tagged pions one can perform an inclusive dE/dx study of the hadronic flavour content plotting the distributions of $(dE/dx) - (dE/dx)^{expected\ for\ kaons}$ in a narrow momentum bin and fitting this distributions with four Gaussian functions with fixed mean values (centered on the expected values for electrons, pions, kaons and protons, all shifted of course by $(dE/dx)^{expected\ for\ kaons}$). From such a 4 Gaussian fit one can extract the content in terms of these particles in the RICH tagged sample of pions and extract therefore the efficiencies and the purity of the RICH pion tag at that fixed value of momentum.
Figures 7.1 and 7.2 show these 4 gaussians fits in 1994 DELPHI Montecarlo data, to show the principle of the technique to cross check the inclusive hadronic flavour content in a given sample through (dE/dx) fits. The corresponding result in the real data sample would look identical.
The efficiency matrix for the three hadronic tags used in this analysis are shown by picture 7.3 and 7.4, respectively for light quarks and b quark events.

7.3 The Analysis Method

Having at our disposal the efficiency matrix for the hadronic tagging program, the central part of the analysis relies on the efficiency matrix inversion to calculate the true distributions from the measured observables according to the system of equations 7.5 :

$$\begin{pmatrix} N_\pi \\ N_{\rm K} \\ N_{\rm p} \end{pmatrix}^{\rm True}_{ib}(x) = \begin{pmatrix} \mathcal{E}^\pi_\pi & \mathcal{E}^\pi_{\rm K} & \mathcal{E}^\pi_{\rm p} \\ \mathcal{E}^{\rm K}_\pi & \mathcal{E}^{\rm K}_{\rm K} & \mathcal{E}^{\rm K}_{\rm p} \\ \mathcal{E}^{\rm p}_\pi & \mathcal{E}^{\rm p}_{\rm K} & \mathcal{E}^{\rm p}_{\rm p} \end{pmatrix}^{-1}_{ib}(x) \cdot \begin{pmatrix} N_\pi \\ N_{\rm K} \\ N_{\rm p} \end{pmatrix}^{\rm Measured}_{ib}(x) \tag{7.5}$$

The variable x stands here for the observables p, x_p, ξ_p, ξ_E, $|y|$, p_t^{in} and p_t^{out}, which are defined in chapter 8.
The efficiency matrices are derived from full Monte Carlo simulation.
This inversion of the system has been performed twice : for light quark (u,d,s) enriched events and for b quark enriched events.
To take into account a possible bias of the b tagging program on the event selection (through the sphericity cut or other event shape variables related to the event topology) , the whole efficiency matrix has been calculated separately for both categories (b and light) of events ($ib = 1, 2$).

Acceptance correction have been applied, according to the DELPHI JETSET Full detector simulation montecarlo and the corresponding generated one. For each momentum bin, observable, and particle flavour, the acceptance correction matrix element term has given by

$$A_{ij} = \frac{1/N^{tot}_{gen}\ dN^{i\ generated}}{1/N^{tot}_{sim}\ dN^{j\ simulated}} \tag{7.6}$$

and the acceptance correction for the tagged number of tracks of bin i

$$N^{i,corrected} = A_{ik} N^k \tag{7.7}$$

The overall global efficiency for a given observable, bin and tag is therefore given by

$$\epsilon^i_{k\ global} = \epsilon^i_{k\ tag}\ \epsilon^i_{k\ acceptance}\ *\ f^{DA/MC} \tag{7.8}$$

where the factor

$$f^{DA/MC} = \frac{(tot\ n.tagged\ tracks\ (\pi + K + p))/(tot.\ n.charg.tracks\ input)_{DATA}}{(tot\ n.tagged\ tracks\ (\pi + K + p))/(tot.\ n.charg.tracks\ input)_{MC}} \tag{7.9}$$

copes with slight difference in the global tags acceptance behaviour in the data and the montecarlo sets. It is flavour independent and its deviation from unity is in the worst cases of the order of 2. – 3.%.

Moreover in the analysis only negative charged tracks have been used at low momenta, ($p < 2.3\ GeV/c$), to reduce the effects of secondary interactions and background on the stable primary (both fragmentation and decay) produced tracks measurement.

The measured inclusive fractions have been corrected for secondary detector interactions and ghosts by means of the full montecarlo detector simulation.
In particular the measured fractions have been corrected in a flavour depend way, calculating the measured ratio by

$$\vec{f}^{meas} = \frac{\vec{N}^{tag}\ (1 - \vec{R}_s^{tag} - \vec{R}_g^{tag})}{N^{tot.charged}\ (1. - R_s^{tot} - R_g^{tot})} \tag{7.10}$$

where $\vec{R}_s^{tag}$ is the flavor-vector secondary tracks in tag i divided by the total number of tracks and $\vec{R}_g^{tag}$ is the corresponding vector for the ghost tracks ($\vec{R}_s^{tot}$ and $\vec{R}_g^{tot}$ correspond to the total number of secondaries and ghosts, flavorwise).

Finally a leptonic ($l = e^{\pm} + \mu^{\pm}$) correction factor has been used, extracted by the montecarlo simulated data, to correct for the $e^{\pm}$ and $\mu^{\pm}$ background in the pion, kaon and proton samples :

$$N_i^{tag} \rightarrow N_i^{tag}\ (1 - \frac{N_{l^{\pm}}}{N^{tagged\ i}}) \tag{7.11}$$

7.3.1 Hadronic Events and Tracks selection

From a sample of 1.4 million events collected by the DELPHI detector during the 1994 LEP run, in each event tracks have been accepted according to the following requirements:

- Relative error on the momentum measurement $< 100\%$
- Track Polar Angle $41° < \Theta_{track} < 139°$ (barrel RICH polar region)
- Track length (in the TPC) ≥ 30 cm
- $p > 0.3\ Gev/c$
- impact parameter relative to the primary vertex in xy < 5 cm
- impact parameter relative to the primary vertex in z < 6 cm
- abs(charge) > 0

The requirements for the hadronic event selection were as follows:

- Number of charged tracks > 5
- Total hadronic energy $> 12\% \times \sqrt{s}$
- Total energy in each hemisphere (forward, backward) $> 3\% \times \sqrt{s}$
- Total energy of all charged tracks $> 12\% \times \sqrt{s}/2$
- Sphericity axis in the barrel region i.e. $40 < \theta^{Sphericity} < 140°$

About 1.1 million events matched these requirements and were taken as input to the b-tagging hadronic content analysis.

7.4 The DELPHI b-quark tagging program

Due to the presence of a very precise Vertex Detector, the tagging of topologically selected $Z \to b\overline{b}$ events is possible.
The b quark tagging is based on the impact parameter (I.P.) in space. For a given track, the I.P. in the $R-\phi$ plane is defined as the minimal distance between the track and the primary interaction point (primary vertex reconstructed in the event), in the plane perpendicular to the beam direction ($R-\phi$ plane).
The sign of the I.P. is defined as positive if the vector joining the primary vertex and the point of closest approach of the track lies in the same direction as the jet to which the given track belongs.
The primary vertex is reconstructed after a selection of the accepted tracks (according to the information on the Vertex Detector) and χ^2 minimization procedure using the position of the LEP beam spot as a constrain.
The beam spot size is rather small ($\sigma_x \simeq 100\ \mu\ m$, $\sigma_y \simeq 10\ \mu\ m$) and its inclusion in the fit significantly improves the accuracy on the result.
Hadrons containing b quarks have a long lifetime (about 1.6 ps) and are produced in Z decays with a large momentum. Moreover B hadrons have large masses, compared to other hadrons. (for example the Λ_b^0 has a mass $m_{\Lambda_b^0} \simeq 5.6\ GeV$, more than 5 times the proton's mass). Therefore the decay products of B hadrons have large impact parameters.
This quantity can therefore be used as tagging variable to separate events originated by b quarks from other hadronic events (from u, d, s, c quarks).
The b-tagging algorithm defines for each accepted track an *impact parameter significance* as the ratio of the I.P. (d) to its error

$$S(d) = \frac{d}{\sigma_d} \tag{7.12}$$

Figure 7.5 shows the distribution of the significance for hadronic events.
After a convolution with an experimentally measured resolution function, (probability density function of the significance distribution) $f(S)$, a track probability function $P(S_0)$ is built, representing the probability for a track from the primary vertex to have a significance absolute value S_0 or greater:

$$P(S_0) = \begin{cases} \int_{S<S_0} f(S)dS & : \quad S_0 < 0 \\ P(-S_0) & : \quad S_0 > 0 \end{cases}$$

Using the track probability function $P(S)$, the probability for each track in the event can be computed according to its significance.
For an event (or an hemisphere) the N-track probability is defined as :

$$P_N \equiv \Pi \cdot \sum_{j=0}^{N-1} (-\ln \Pi)^j / j!, \qquad \text{where} \qquad \Pi \equiv \prod_{i=1}^{N} P(S_i). \tag{7.13}$$

This variable gives the probability for a group of N tracks with the observed values of significance all to come from the primary vertex. By construction, the distribution of P_N should be flat for groups of tracks from the primary vertex, provided the significances of these tracks are uncorrelated, while for b quarks it should have a sharp peak at 0.
Figures 7.6 and 7.7 show the behaviour of the N track event probability for positive track

impact parameters in all events and in the three classes uds, c, b.
When the Rz impact parameter is measured, the probability $P(S_0)_z$ is computed in the same way as for the $R\phi$ impact parameter. The N-track probability is then given by the combination of the $P_{r\phi}$ and P_z probabilities. The N-track probability is the only variable which is used in this approach for tagging b hadrons. The event probability, P_E, is the probability computed using all tracks of the event.
Similarly, the hemisphere or jet probabilities, P_H or P_J, are the probabilities computed from the tracks belonging to a given hemisphere or jet. The positive event probability, P_E^+, is - by definition - the event probability computed using all tracks which have positive significance.
Figure 7.8 shows the efficiency and purity of the tagged sample for different values of the cut on the event probability (upper) and on the hemisphere probability (lower) for the 3-coordinates VD (full line) and the 2-coordinates VD (dashed line). The curves were calculated for a sample of simulated hadronic events selected within the acceptance of the vertex detector ($|\cos(\theta_{thrust})| < 0.75$). This selection corresponds to an efficiency of 69%. It can be seen from the figure that the possibility of measuring both $R\phi$ and Rz increases the efficiency for a given purity.

In order to get a pure uds quark sample a correction to the measured (tagged) number of particles in both categories (uds and b quarks) has been applied, according to the system of two equations

$$\begin{pmatrix} N^b \\ N^{uds} \end{pmatrix} = \begin{pmatrix} P^b & (1-P^{uds}) \\ P^{uds} & (1-P^b) \end{pmatrix} \begin{pmatrix} N^{b,tag} \\ N^{uds,tag} \end{pmatrix} \tag{7.14}$$

where P^b and P^{uds} are the b-purity and uds-purity respectively of the b-tagging program. They have been estimated by means of fully simulated montecarlo data.
Given the values of the two cuts in the positive event probability defining the two classes of events, namely $-log_{10}(P_E^+) > 2$ ($P_E^+ < 0.01$) for b events and $-log_{10}(P_E^+) < 0.2218$ ($P_E^+ > 0.6$) for uds quark events, the purities are given respectively by

$$Purity^{b\ events} \equiv P^b = 0.829 \tag{7.15}$$

$$Purity^{uds\ events} \equiv P^{uds} = 0.860 \tag{7.16}$$

The total number of selected tagged b events in the montecarlo is 148,990 and uds tagged is 207,325.
In the data the b tagging program tagged and selected 96,270 b events and 143,305 uds tagged events.

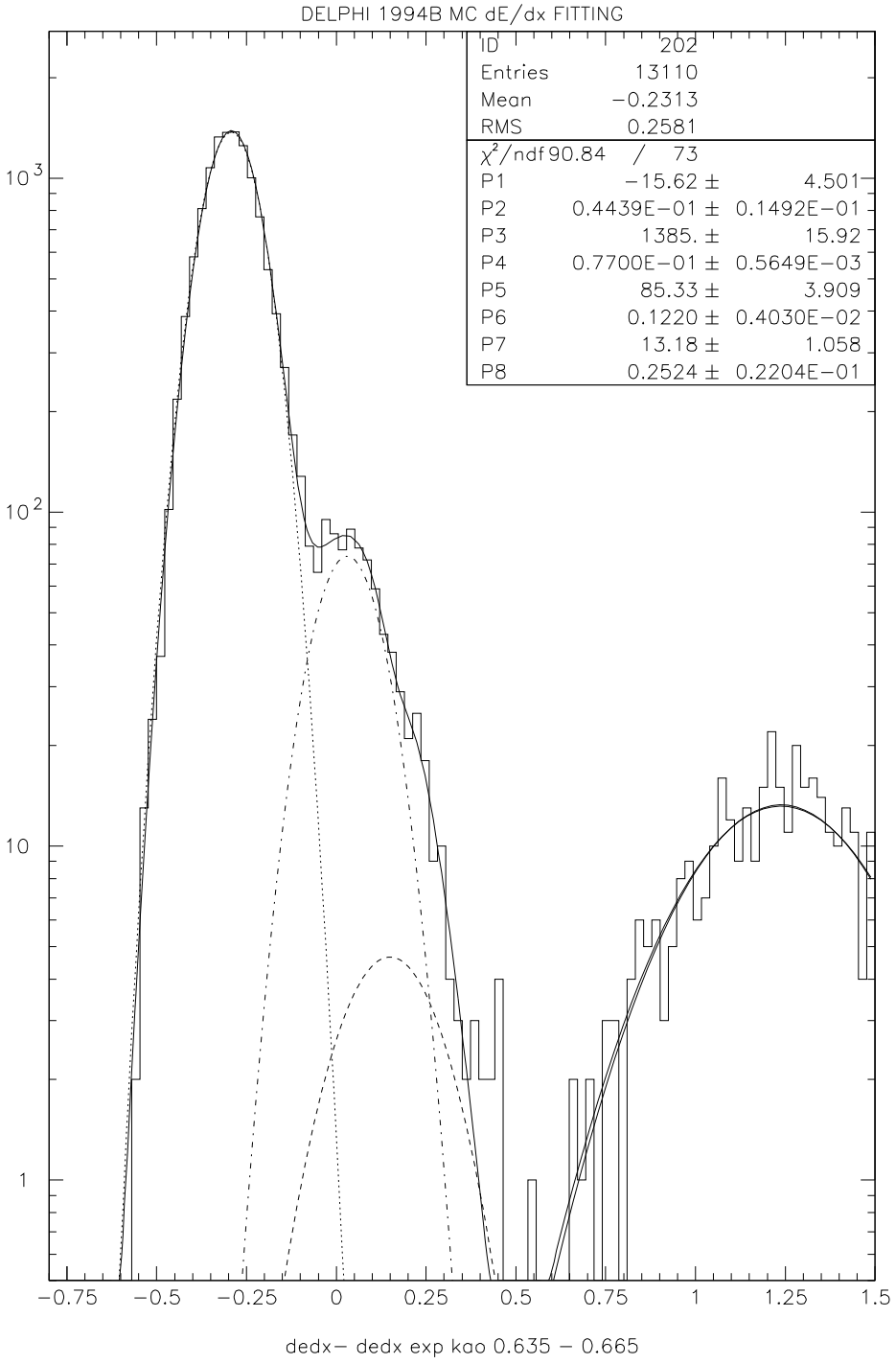

Figure 7.1: *4 gaussians Fit of the* $(dE/dx) - (dE/dx)^{expected\ kaon}$ *distribution in a Montecarlo sample in the momentum range 0.635-0.665 GeV/c. The mean values are fixed, the Constants are proportional to the absolute values of parameter P1, P3, P5 and P7. The widths are parameters P2, P4, P6 and P8. Left to right : pions (including muons), kaons, electrons and protons.*

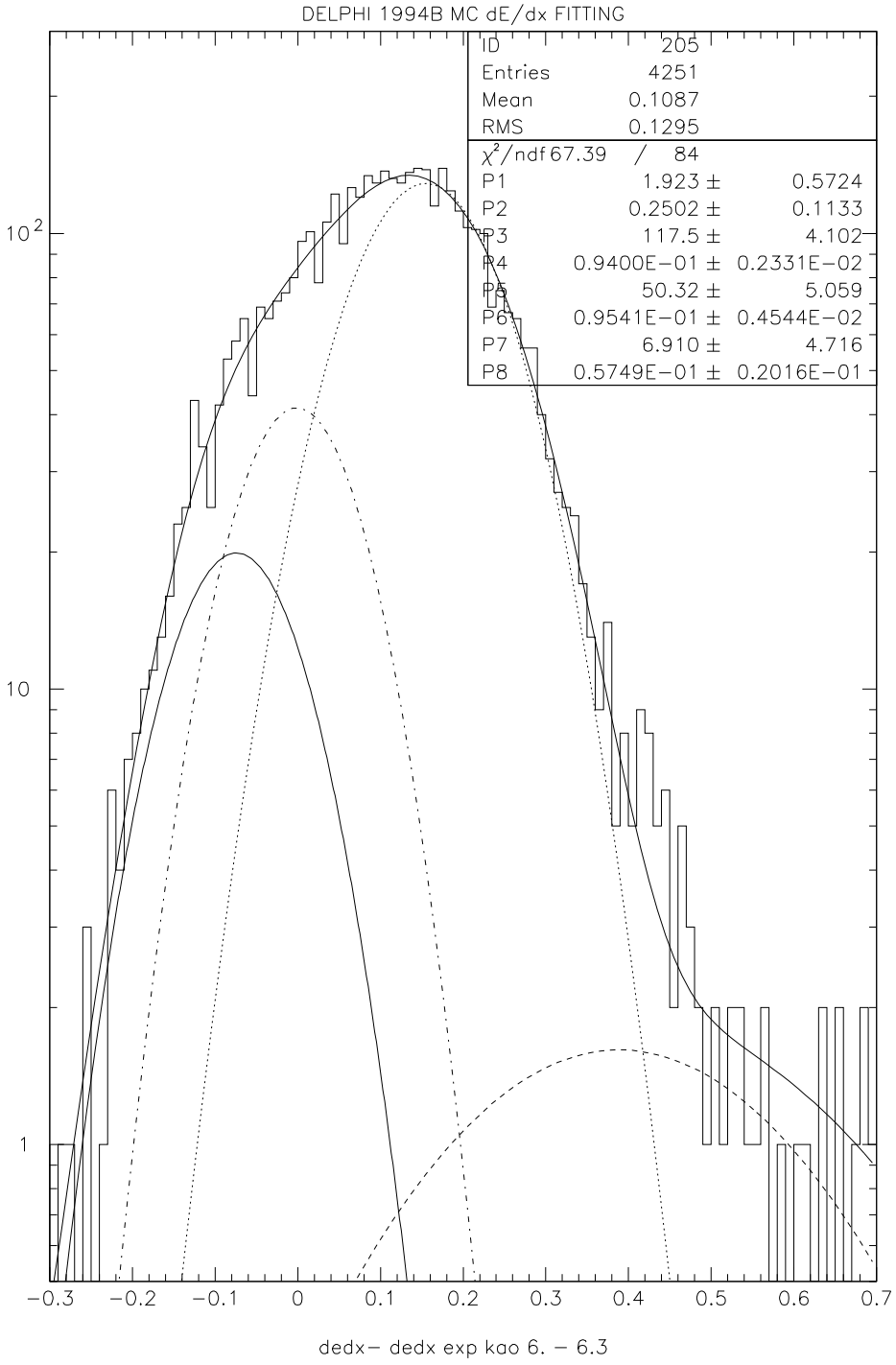

Figure 7.2: *4 gaussians Fit of the* $(dE/dx)-(dE/dx)^{expected\ kaon}$ *distribution in a Montecarlo sample in the momentum range 6.0-6.3 GeV/c. The mean values are fixed, the Constants are proportional to the absolute values of parameter P1, P3, P5 and P7. The widths are parameters P2, P4, P6 and P8. Left to right : protons, kaons, pions (including muons) and electrons.*

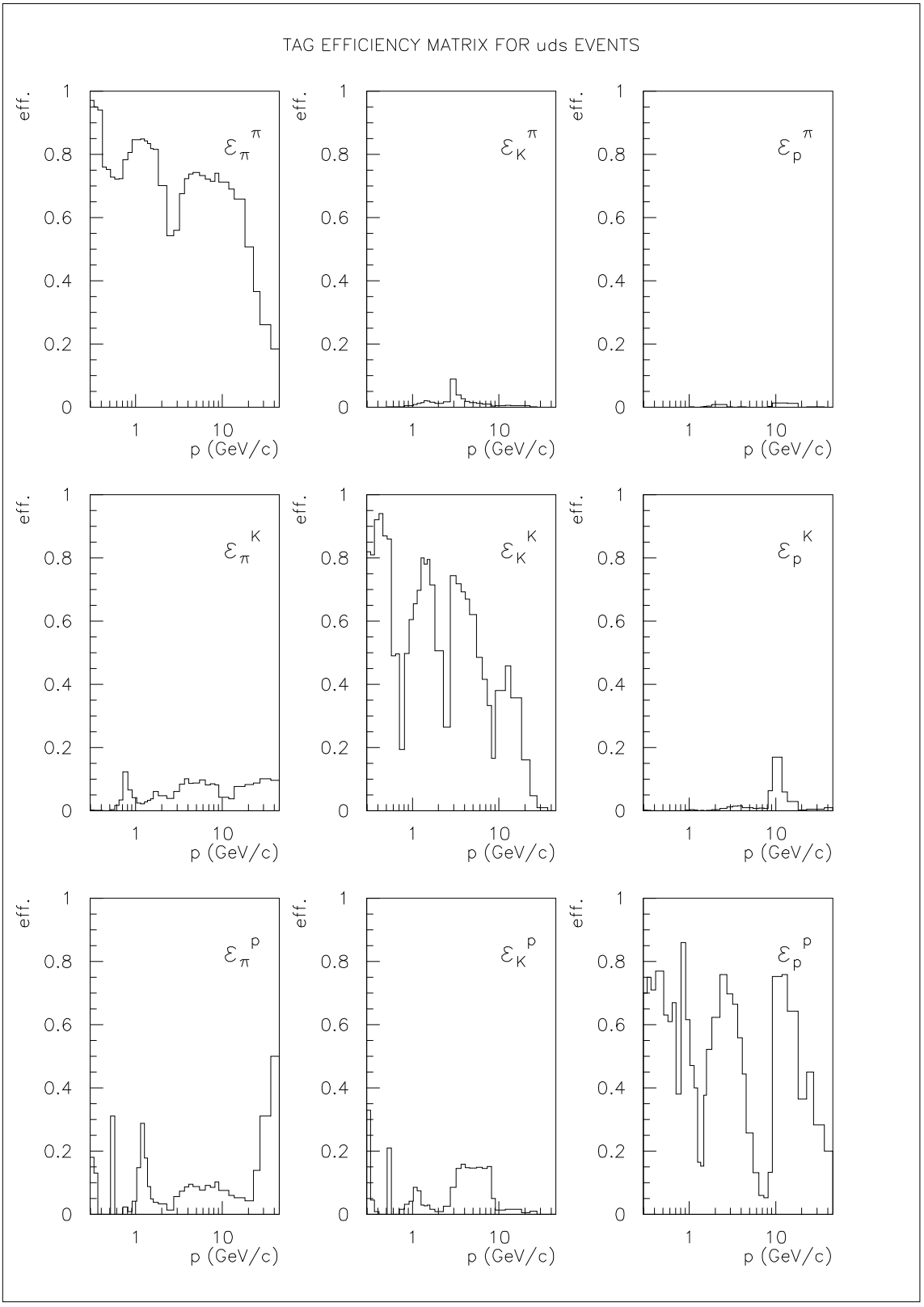

Figure 7.3: *Hadronic Tag efficiency matrix in light quark Z decay events : the first line shows (from left to right) the efficiency on pions for the pion, kaon and proton tags and similarly for the other tags and lines.*

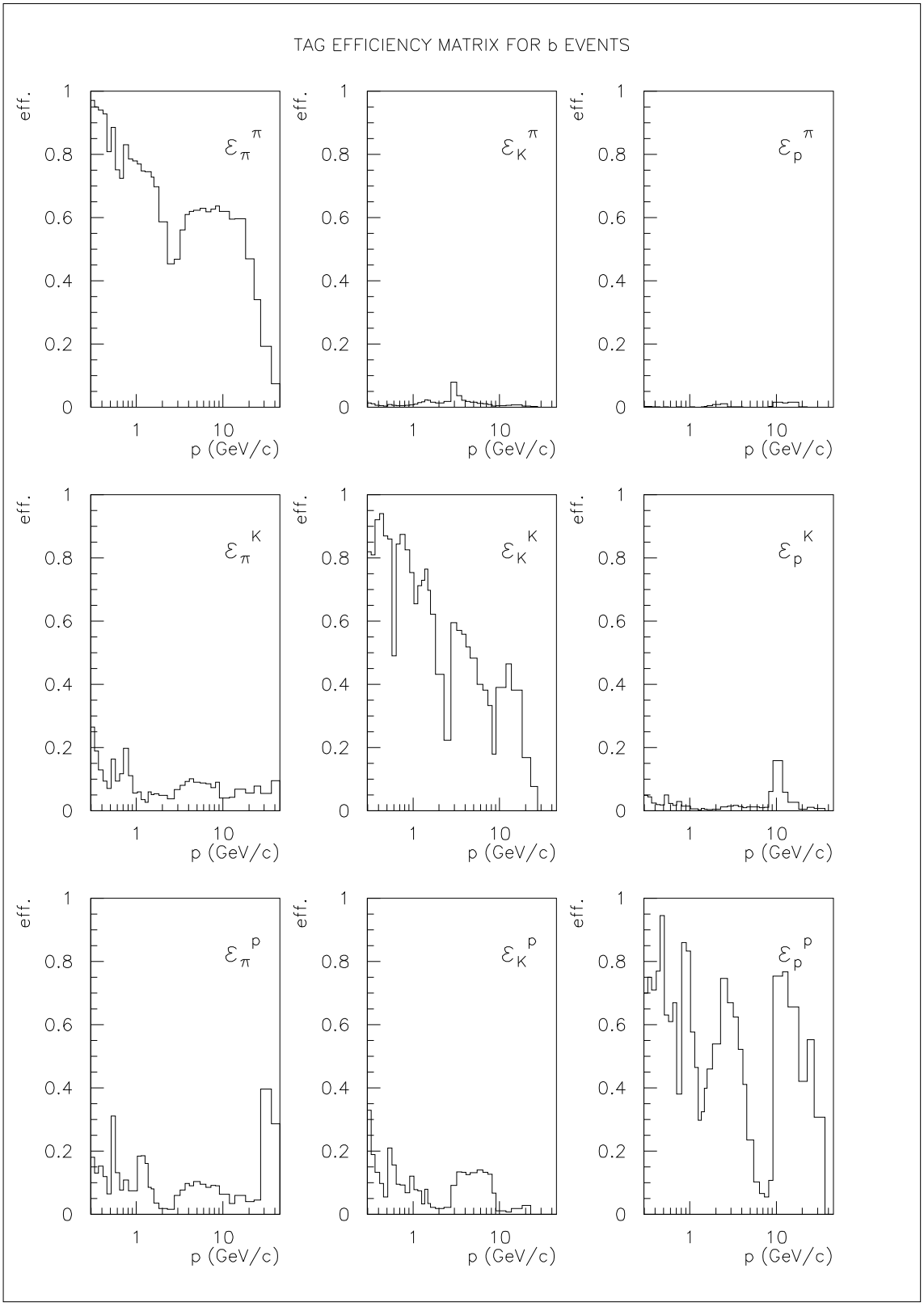

Figure 7.4: *Hadronic Tag efficiency matrix in heavy quark Z decay events : the first line shows (from left to right) the efficiency on pions for the pion, kaon and proton tags and similarly for the other tags and lines.*

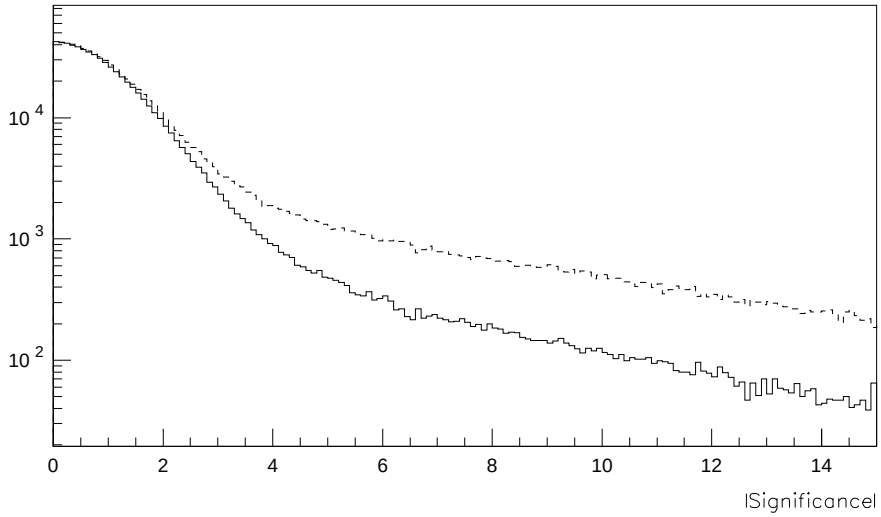

Figure 7.5: *Distribution of the absolute value of the significance as built by the b tagging program. The dashed line is for positive impact parameters tracks. The full line for negative impact parameters.*

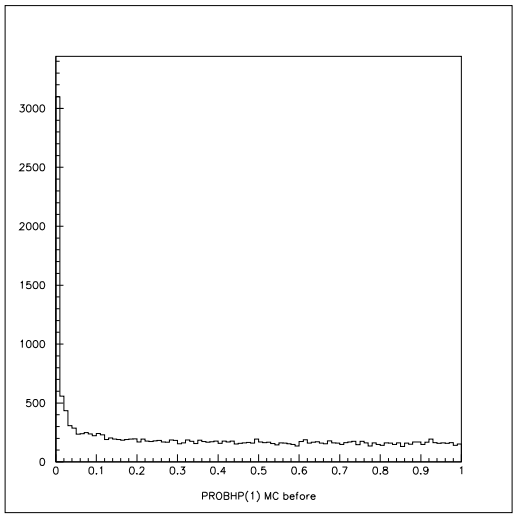

Figure 7.6: P_E^+ *: b tagging event probability as built by the b tagging algorithm in the DATA sample. In this analysis cuts have been applied at* $P_E^+ < 0.01$ *and* $P_E^+ > 0.6$

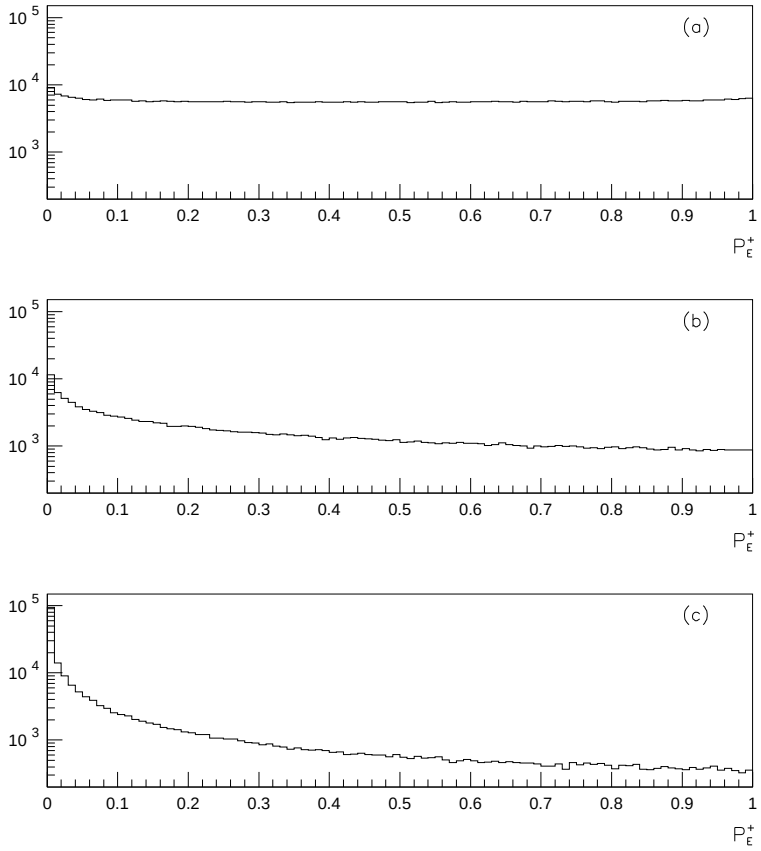

Figure 7.7: *b tagging N-tracks probabilities (for positive significance tracks) for uds quark (above), c quark (middle) and b quark events (bottom). (Montecarlo)*

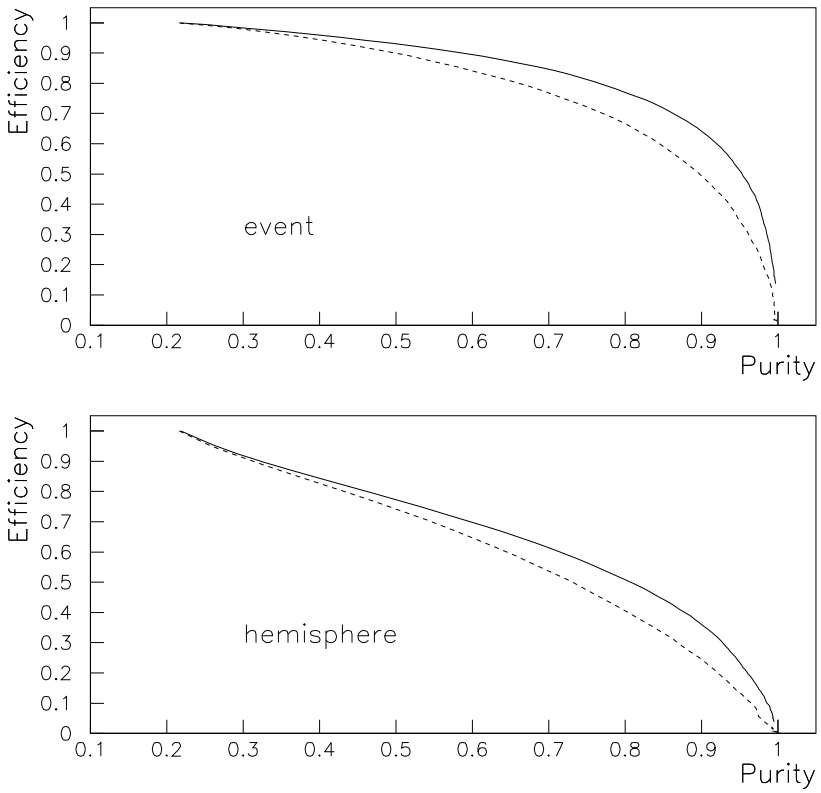

Figure 7.8: *b tagging efficiencies as a function of the purity of the tagged sample for different values of the cut on the event probability (upper) and on the hemisphere probability (lower) for the 3-coordinates VD providing Rz information (full line) and the 2-coordinates VD that provided only R phi information (dashed line).*

Chapter 8

Results

8.1 Introduction

In this chapter the results of the inclusive charged π^+, K^+ and p production analysis are reported, the measured observables are defined, the error analysis is described.
The differential production spectra versus momentum, the transversal momenta inside and outside the event plane (p_t^{in}, p_t^{out}), the rapidity ($|y|$), the charged π^+, K^+ and p multiplicities have been measured in $Z \to u\overline{u}, d\overline{d}, s\overline{s}$ events and in $Z \to b\overline{b}$ events and the position of the peak position of the ξ_p variable has been determined according to a modified (distorted) Gaussian fit.

Next section (section 2) shows the results. It deals with the ξ_p and ξ_E distributions for π^+, K^+ and p, and the average charge multiplicities in light quark and b-quark tagged events. It also shows the momentum inclusive production spectra,
rapidity, p_t^{in}, p_t^{out} and x_p spectra for both classes of events.

Last section gives a global description of the treatment of the systematic error in the analysis, concerning the inclusive spectra tagging systematics and the one induced by the b-tagging for heavy and light quarks.

8.2 Results

In this section the results of the analysis are reported. Subsection 8.2.1 shows the fits of the $\xi_p \equiv ln(1/x_p)$ and $\xi_E \equiv ln(1/x_E)$ distributions to extract the ξ_p^* value for π^+, K^+ and p in uds quark and b quark events and the particle multiplicities.
Subsection 8.2.2 deals with the production cross section versus the kinematical variables studied, like rapidity, the normalized momentum x_p, $|p_t^{in}|$, $|p_t^{out}|$. The last subsection, 8.2.3, reports the values of multiplicities in b events and in light quark events.

8.2.1 ξ_p^* values and ξ_E distributions for π^+, K^+, p in b and uds quark events

An important point of interest for the test of fragmentation models is their prediction on the spectra of identified hadrons.
In particular, in the MLLA+LPHD model approach (Modified Leading Log Approximation in the Local Parton-Hadron Duality ansatz) ([33], [34]) to the description of hadronization and fragmentation, one can follow numerically the whole process of the e^+e^- annihilation into hadrons and make direct quantitative predictions for the final states. It is interesting to check its predictions on ξ_p^* with respect to the hadron mass spectra, in particular the prediction for baryons and mesons to have the same behaviour (with respect to the ξ_p^* position)

$$\xi_p^* \simeq max_{\ln(1/x_p)}\left(\frac{dN}{d\ln(1/x_p)}\right) \tag{8.1}$$

where x_p is the normalized momentum p/p_{beam} and N is the produced number of particles.
For primary produced hadrons the expected behavior is $\xi_p^* \propto -log(M^{hadron})$.
Moreover MLLA+LPHD makes predictions on the behaviour of ξ_p^* versus the centre of mass energy $\sqrt{s}$.
In particular ξ_p^* is foreseen to be linear in $ln(\sqrt{s})$.
A suggested [35] modified gaussian fit to the ξ_p distribution taking into account high order corrections to the raw level QCD diagrams underlying hadron production is given by the function

$$D = \frac{N}{\sigma\sqrt{2\pi}} e^{\left(\frac{1}{8}k - \frac{1}{2}s\delta - \frac{1}{4}(2+k)\delta^2 + \frac{1}{6}s\delta^3 + \frac{1}{24}k\delta^4\right)} \tag{8.2}$$

In this formula δ is relative deviation from the mean $\delta = (\xi - \overline{\xi})/\sigma)$, s is the skewness of the distribution, k is its kurtosis.
The fitting procedure was applied to the data and to the three generated distributions of JETSET, HERWIG and ARIADNE. The fits are shown in figures 8.4 to 8.6. The fit results are listed in table 8.1.
They are summarized by picture 8.3.
The ξ_E distribution ($\xi_E \equiv ln(1/x_E)$, where x_E is the normalized energy $x_E \equiv E^{particle}/E^{beam}$) distributions have been fitted to the expression

$$f(\xi_E) = -a(1 - e^{-\xi_E})^b \cdot (\xi_E - \log(\frac{\sqrt{s}}{2m})) \cdot \sum_{i=1}^{5} c_i \xi^i \tag{8.3}$$

where m is the hadron mass, the parameters a, b, c_i are fitted, and from the fit a value for the particle multiplicity has been extracted.
Figures 8.5 and 8.6 show the fit and the corresponding parameters in light (above) and heavy (below) quark events.

Previous analysis [67] have investigated the dependence of ξ_p^* on the available centre of mass energy $\sqrt{s}$ to check the prediction of $MLLA+LPHD$ on this subject. It has been found that the dependence is the same for K^+ and p, ξ_p^* increasing linearly with $ln(\sqrt{s})$. The results of this analysis are shown by picture 8.1.

(uds)	data	JETSET 7.4	HERWIG 5.8	ARIADNE 4.08
π^+	3.88 ± 0.08	3.86 ± 0.03	3.86 ± 0.03	3.90 ± 0.03
K^+	2.86 ± 0.09	2.94 ± 0.05	3.18 ± 0.06	3.04 ± 0.05
p	2.77 ± 0.09	2.72 ± 0.05	2.75 ± 0.05	2.79 ± 0.05
(b)	data	JETSET 7.4	HERWIG 5.8	ARIADNE 4.08
π^+	3.71 ± 0.08	3.75 ± 0.03	3.78 ± 0.03	3.75 ± 0.04
K^+	2.54 ± 0.16	2.52 ± 0.04	2.66 ± 0.04	2.58 ± 0.05
p	2.95 ± 0.16	3.02 ± 0.07	2.45 ± 0.05	2.76 ± 0.06

Table 8.1: *ξ^* position for π, K and p according to the modified gaussian fit. Above: for light quarks (enriched uds sample). Below: heavy quarks (enriched b sample).*

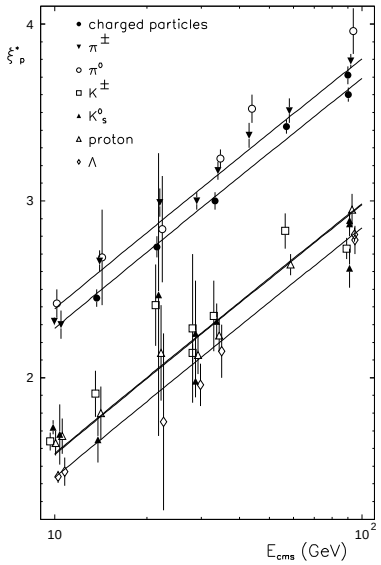

Figure 8.1: *Dependence of ξ_p^* values for π^+, K^+, p on the centre of mass energy $\sqrt{s}$. The proton and kaon lines happen to lay on top of each other. (from reference [67])*

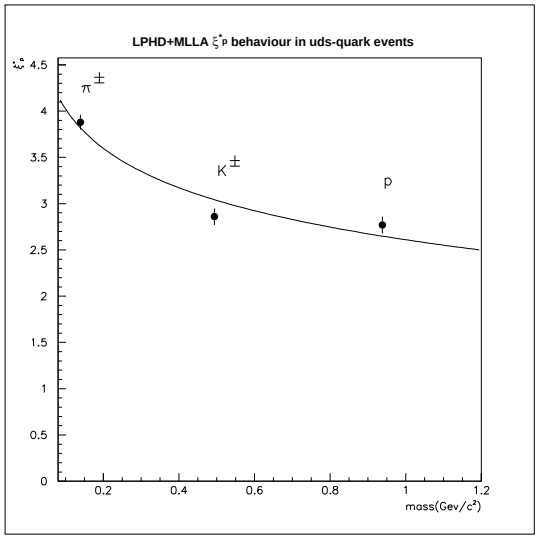

Figure 8.2: *Dependence of ξ_p^* values for π^+, K^+, p on the hadron mass for uds quark events. Superimposed is the fitted function $\xi_p^* = 2.61 + 0.61 * (-log(mass))$.*

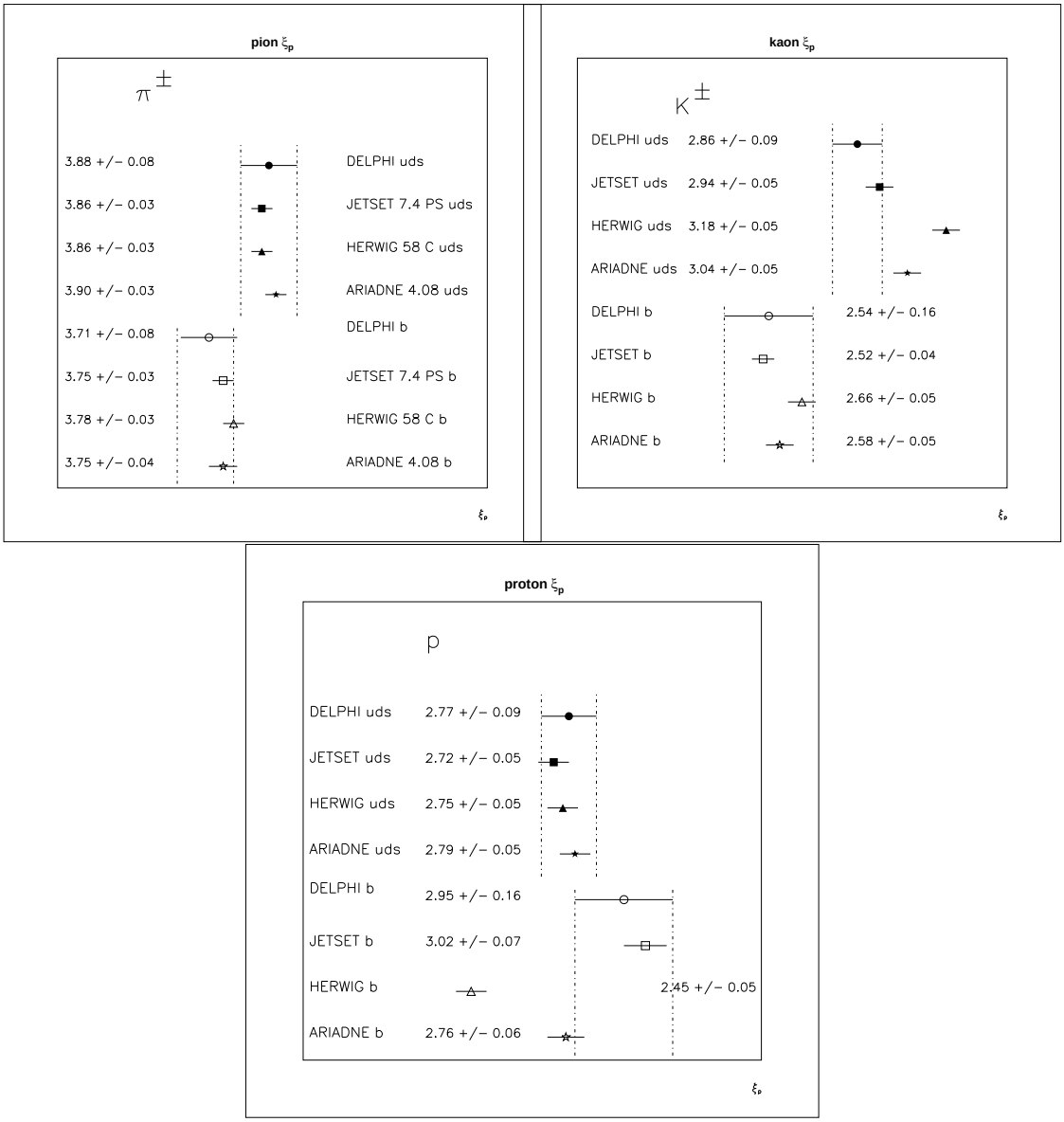

Figure 8.3: *measured ξ_p^* values for π^+,K^+ and p for data and Montecarlo, uds (above) and b (below) events for each box.*

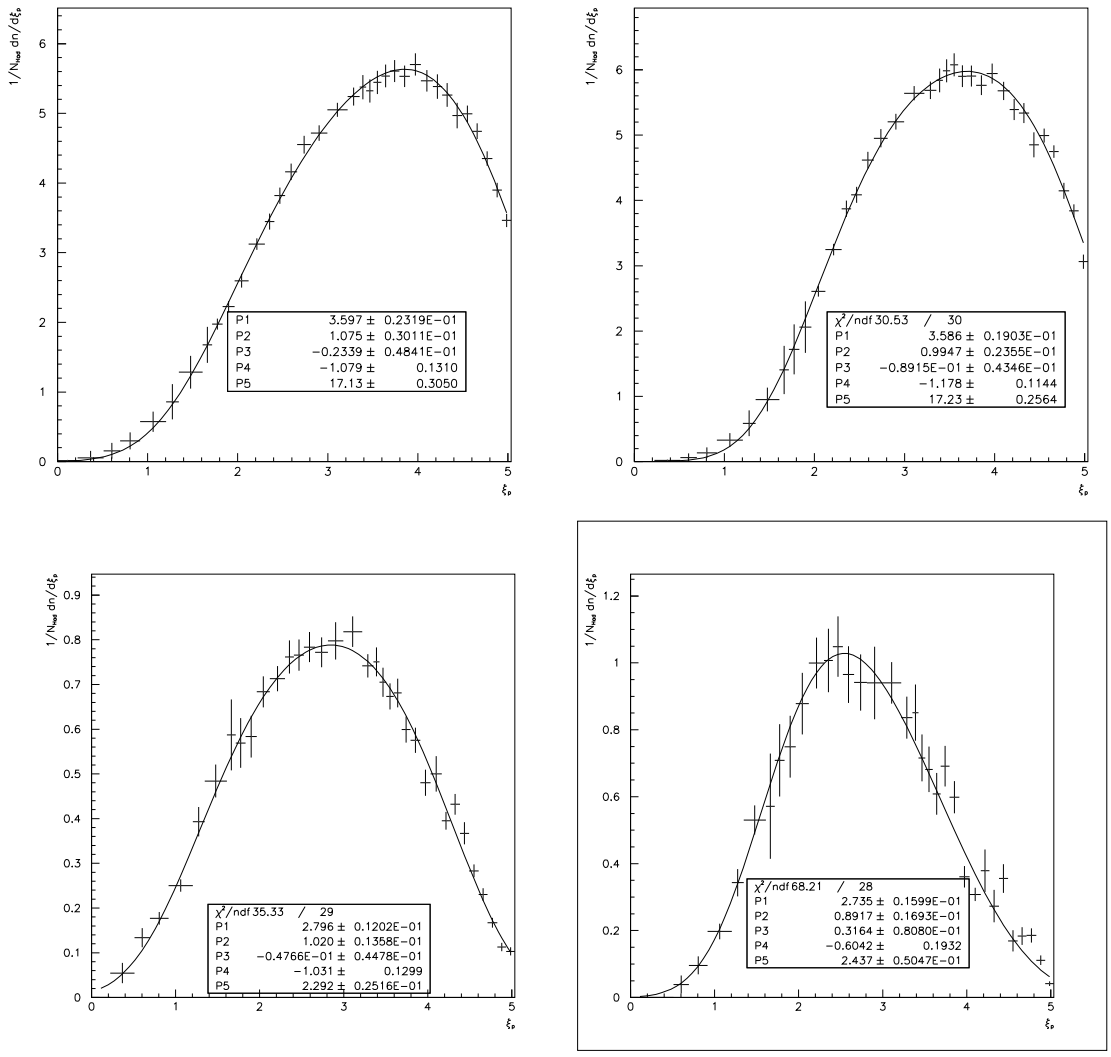

Figure 8.4: *Above: Fit of the ξ_p distribution for π^+ in light (left) and heavy (right) quark Z decay events. Below: Fit of the ξ_p distribution for K^+ in light (left) and heavy (right) quark Z decay events*

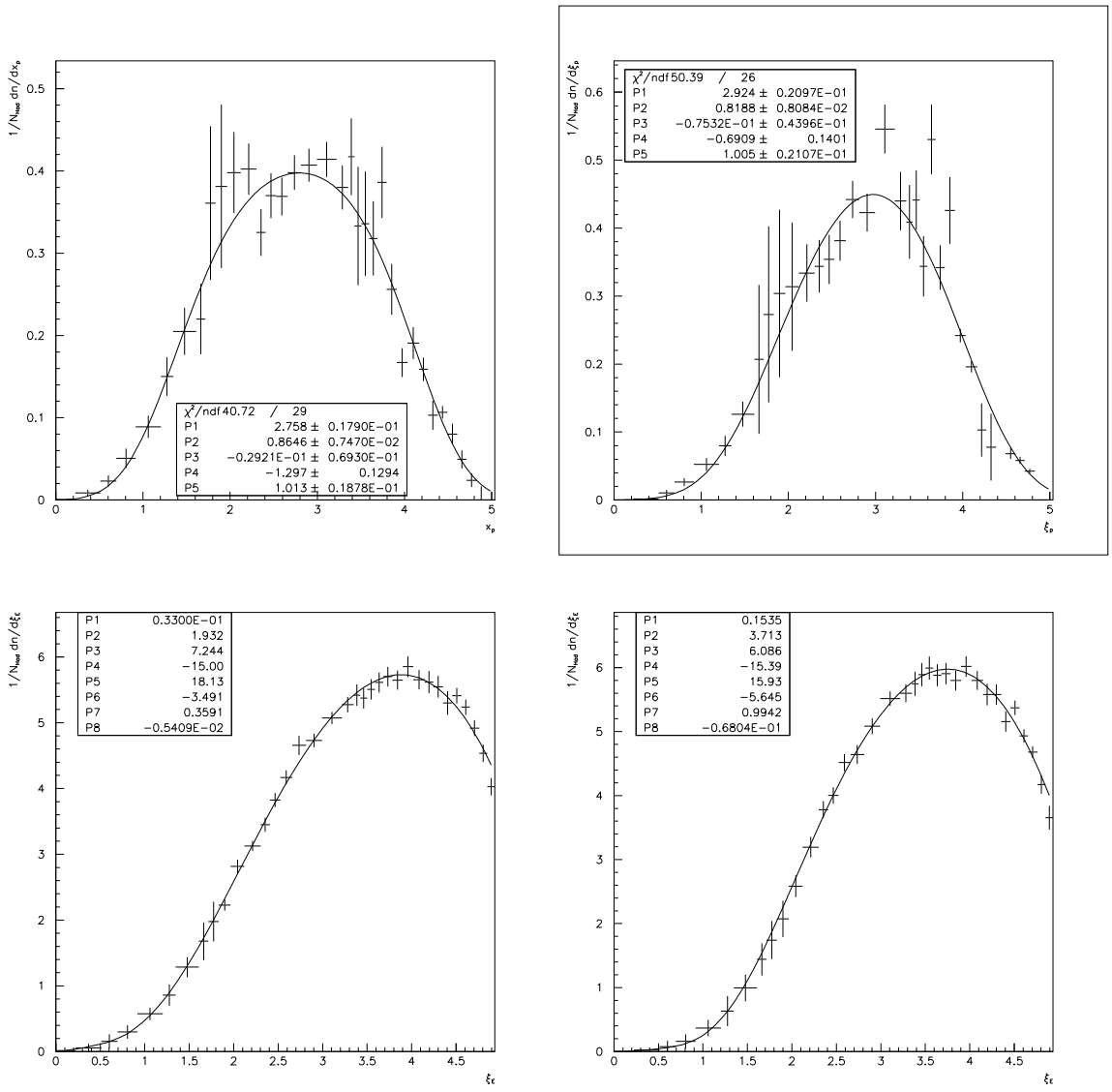

Figure 8.5: *Above: Fit of the ξ_p distribution for p in light (left) and heavy (right) quark Z decay events Below: Fit of the ξ_E distribution for π^+ in light (left) and heavy (right) quark Z decay events*

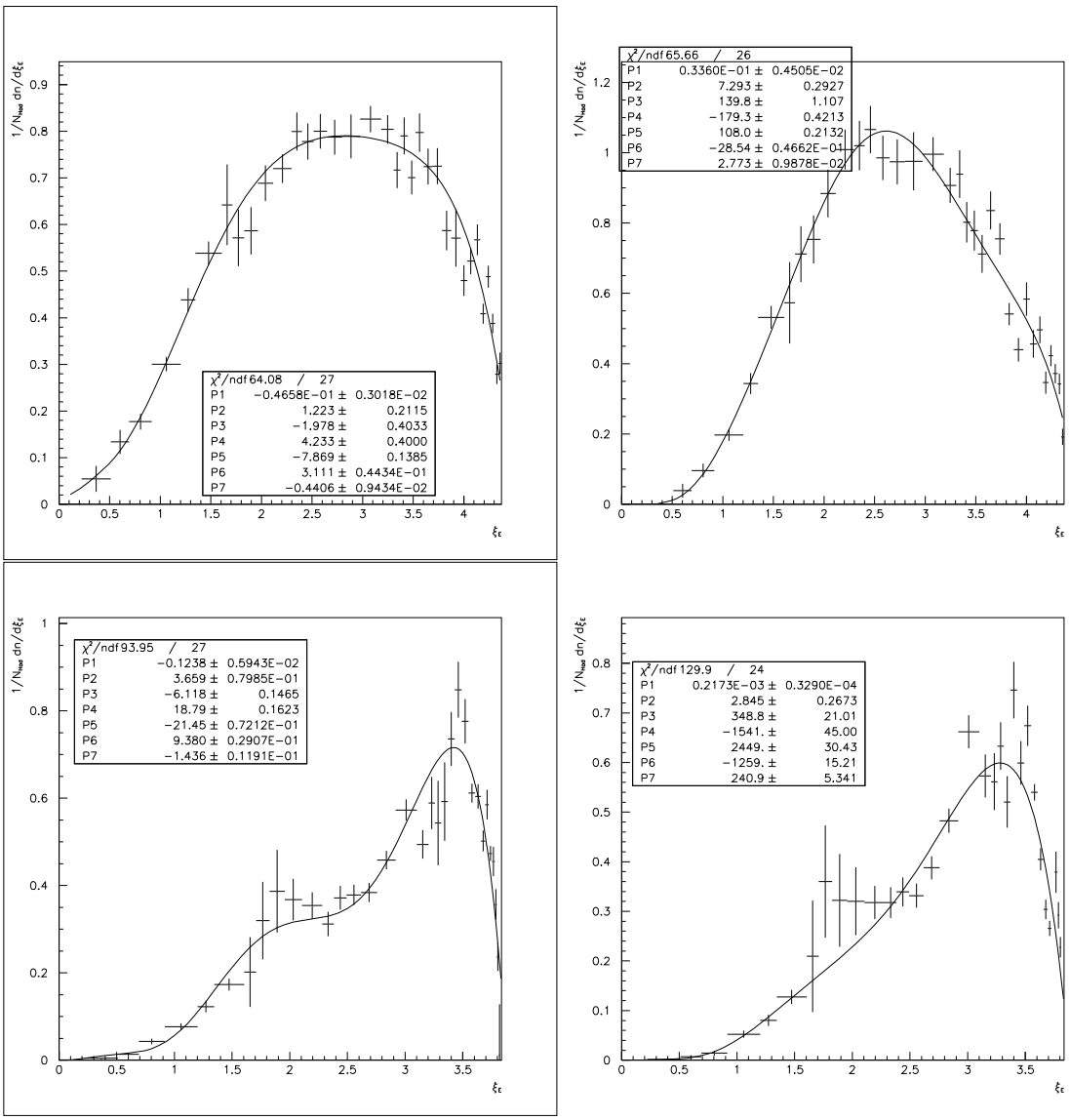

Figure 8.6: *Above: Fit of the ξ_E distribution for K^+ in light (left) and heavy (right) quark Z decay events Below: Fit of the ξ_E distribution for p in light (left) and heavy (right) quark Z decay events*

ξ_p range	$< \xi_p >$	$1/N\ dN/d\xi_p$	$\Delta(1/N\ dN/d\xi_p)^{stat.+syst.}$
0.000 – 0.223	0.111	0.014	± 0.012
0.223 – 0.511	0.366	0.055	± 0.016
0.511 – 0.693	0.601	0.158	± 0.015
0.693 – 0.916	0.804	0.300	± 0.017
0.916 – 1.203	1.060	0.578	± 0.019
1.203 – 1.347	1.275	0.865	± 0.035
1.347 – 1.609	1.478	1.289	± 0.038
1.609 – 1.714	1.662	1.682	± 0.059
1.714 – 1.832	1.773	1.979	± 0.059
1.832 – 1.966	1.899	2.231	± 0.059
1.966 – 2.120	2.043	2.596	± 0.060
2.120 – 2.302	2.211	3.121	± 0.061
2.302 – 2.407	2.355	3.440	± 0.085
2.407 – 2.525	2.466	3.814	± 0.086
2.525 – 2.659	2.592	4.155	± 0.088
2.659 – 2.813	2.736	4.637	± 0.095
2.813 – 2.995	2.904	4.707	± 0.083
2.995 – 3.218	3.107	5.039	± 0.075
3.218 – 3.352	3.285	5.233	± 0.095
3.352 – 3.426	3.389	5.367	± 0.130
3.426 – 3.506	3.466	5.313	± 0.124
3.506 – 3.593	3.550	5.435	± 0.123
3.593 – 3.688	3.641	5.532	± 0.120
3.688 – 3.794	3.741	5.604	± 0.117
3.794 – 3.912	3.853	5.529	± 0.114
3.912 – 4.034	3.973	5.699	± 0.118
4.034 – 4.166	4.100	5.466	± 0.115
4.166 – 4.268	4.217	5.384	± 0.130
4.268 – 4.382	4.325	5.264	± 0.126
4.382 – 4.491	4.436	4.969	± 0.135
4.491 – 4.605	4.548	4.994	± 0.088
4.605 – 4.710	4.657	4.744	± 0.083
4.710 – 4.828	4.769	4.353	± 0.076
4.828 – 4.933	4.880	3.901	± 0.076
4.933 – 5.035	4.984	3.098	± 0.070

Table 8.2: *differential pion production cross section versus ξ_p for uds events with statistical+systematic errors.*

ξ_p range	$< \xi_p >$	$1/N\ dN/d\xi_p$	$\Delta(1/N\ dN/d\xi_p)^{stat+syst}$
0.223 – 0.511	0.366	0.054	± 0.022
0.511 – 0.693	0.601	0.133	± 0.021
0.693 – 0.916	0.804	0.177	± 0.014
0.916 – 1.203	1.060	0.250	± 0.014
1.203 – 1.347	1.275	0.393	± 0.033
1.347 – 1.609	1.478	0.484	± 0.036
1.609 – 1.714	1.662	0.587	± 0.079
1.714 – 1.832	1.773	0.569	± 0.055
1.832 – 1.966	1.899	0.583	± 0.046
1.966 – 2.120	2.043	0.683	± 0.034
2.120 – 2.302	2.211	0.712	± 0.028
2.302 – 2.407	2.355	0.761	± 0.037
2.407 – 2.525	2.466	0.765	± 0.034
2.525 – 2.659	2.592	0.783	± 0.033
2.659 – 2.813	2.736	0.772	± 0.033
2.813 – 2.995	2.904	0.797	± 0.041
2.995 – 3.218	3.107	0.818	± 0.034
3.218 – 3.352	3.285	0.741	± 0.025
3.352 – 3.426	3.389	0.750	± 0.032
3.426 – 3.506	3.466	0.705	± 0.032
3.506 – 3.593	3.550	0.673	± 0.029
3.593 – 3.688	3.641	0.680	± 0.032
3.688 – 3.794	3.741	0.599	± 0.029
3.794 – 3.912	3.853	0.575	± 0.028
3.912 – 4.034	3.973	0.480	± 0.029
4.034 – 4.166	4.100	0.500	± 0.039
4.166 – 4.268	4.217	0.395	± 0.019
4.268 – 4.382	4.325	0.432	± 0.023
4.382 – 4.491	4.436	0.367	± 0.024
4.491 – 4.605	4.548	0.283	± 0.014
4.605 – 4.710	4.657	0.230	± 0.014
4.710 – 4.828	4.769	0.167	± 0.010
4.828 – 4.933	4.880	0.113	± 0.009
4.933 – 5.035	4.984	0.103	± 0.009

Table 8.3: *differential kaon production cross section versus ξ_p for uds events with statistical+systematic error.*

ξ_p range	$< \xi_p >$	$1/N\ dN/d\xi_p$	$\Delta(1/N\ dN/d\xi_p)^{stat.+syst.}$
0.223 – 0.511	0.366	0.008	± 0.0037
0.511 – 0.693	0.601	0.023	± 0.0065
0.693 – 0.916	0.804	0.050	± 0.0117
0.916 – 1.203	1.060	0.089	± 0.0135
1.203 – 1.347	1.275	0.150	± 0.0234
1.347 – 1.609	1.478	0.205	± 0.0286
1.609 – 1.714	1.662	0.220	± 0.0428
1.714 – 1.832	1.773	0.361	± 0.0935
1.832 – 1.966	1.899	0.381	± 0.0993
1.966 – 2.120	2.043	0.398	± 0.0493
2.120 – 2.302	2.211	0.402	± 0.0311
2.302 – 2.407	2.355	0.325	± 0.0284
2.407 – 2.525	2.466	0.370	± 0.0273
2.525 – 2.659	2.592	0.369	± 0.0230
2.659 – 2.813	2.736	0.398	± 0.0210
2.813 – 2.995	2.904	0.407	± 0.0198
2.995 – 3.218	3.107	0.414	± 0.0213
3.218 – 3.352	3.285	0.380	± 0.0267
3.352 – 3.426	3.389	0.417	± 0.0466
3.426 – 3.506	3.466	0.333	± 0.0719
3.506 – 3.593	3.550	0.336	± 0.0634
3.593 – 3.688	3.641	0.318	± 0.0451
3.688 – 3.794	3.741	0.386	± 0.0432
3.794 – 3.912	3.853	0.256	± 0.0310
3.912 – 4.034	3.973	0.167	± 0.0174
4.034 – 4.166	4.100	0.190	± 0.0195
4.166 – 4.268	4.217	0.158	± 0.0143
4.268 – 4.382	4.325	0.103	± 0.0176
4.382 – 4.491	4.436	0.106	± 0.0076
4.491 – 4.605	4.548	0.080	± 0.0125
4.605 – 4.710	4.657	0.049	± 0.0109
4.710 – 4.828	4.769	0.024	± 0.0083

Table 8.4: *differential proton production cross section versus ξ_p for uds events with statistical+systematic errors.*

ξ_p range	$< \xi_p >$	$1/N\ dN/d\xi_p$	$\Delta(1/N\ dN/d\xi_p)^{stat.+syst.}$
0.223 – 0.511	0.366	0.020	± 0.010
0.511 – 0.693	0.601	0.062	± 0.064
0.693 – 0.916	0.804	0.136	± 0.082
0.916 – 1.203	1.060	0.332	± 0.106
1.203 – 1.347	1.275	0.588	± 0.198
1.347 – 1.609	1.478	0.952	± 0.183
1.609 – 1.714	1.662	1.404	± 0.368
1.714 – 1.832	1.773	1.718	± 0.383
1.832 – 1.966	1.899	2.059	± 0.394
1.966 – 2.120	2.043	2.610	± 0.083
2.120 – 2.302	2.211	3.247	± 0.087
2.302 – 2.407	2.355	3.872	± 0.124
2.407 – 2.525	2.466	4.087	± 0.122
2.525 – 2.659	2.592	4.616	± 0.127
2.659 – 2.813	2.736	4.952	± 0.140
2.813 – 2.995	2.904	5.206	± 0.119
2.995 – 3.218	3.107	5.641	± 0.109
3.218 – 3.352	3.285	5.686	± 0.135
3.352 – 3.426	3.389	5.838	± 0.183
3.426 – 3.506	3.466	5.984	± 0.176
3.506 – 3.593	3.550	6.077	± 0.175
3.593 – 3.688	3.641	5.901	± 0.167
3.688 – 3.794	3.741	5.903	± 0.160
3.794 – 3.912	3.853	5.764	± 0.151
3.912 – 4.034	3.973	5.943	± 0.153
4.034 – 4.166	4.100	5.677	± 0.141
4.166 – 4.268	4.217	5.392	± 0.159
4.268 – 4.382	4.325	5.337	± 0.152
4.382 – 4.491	4.436	4.851	± 0.192
4.491 – 4.605	4.548	4.992	± 0.106
4.605 – 4.710	4.657	4.748	± 0.096
4.710 – 4.828	4.769	4.146	± 0.121
4.828 – 4.933	4.880	3.841	± 0.101
4.933 – 5.035	4.984	3.062	± 0.109

Table 8.5: *differential pion production cross section versus ξ_p for b events together with statistical+systematic errors.*

ξ_p range	$< \xi_p >$	$1/N\ dN/d\xi_p$	$\Delta(1/N\ dN/d\xi_p)^{stat.+syst.}$
0.511 – 0.693	0.601	0.039	± 0.027
0.693 – 0.916	0.804	0.096	± 0.027
0.916 – 1.203	1.060	0.197	± 0.023
1.203 – 1.347	1.275	0.343	± 0.041
1.347 – 1.609	1.478	0.530	± 0.044
1.609 – 1.714	1.662	0.571	± 0.157
1.714 – 1.832	1.773	0.709	± 0.108
1.832 – 1.966	1.899	0.749	± 0.092
1.966 – 2.120	2.043	0.878	± 0.092
2.120 – 2.302	2.211	0.999	± 0.076
2.302 – 2.407	2.355	1.007	± 0.095
2.407 – 2.525	2.466	1.049	± 0.090
2.525 – 2.659	2.592	0.965	± 0.085
2.659 – 2.813	2.736	0.941	± 0.084
2.813 – 2.995	2.904	0.940	± 0.108
2.995 – 3.218	3.107	0.940	± 0.062
3.218 – 3.352	3.285	0.837	± 0.063
3.352 – 3.426	3.389	0.851	± 0.084
3.426 – 3.506	3.466	0.716	± 0.070
3.506 – 3.593	3.550	0.682	± 0.068
3.593 – 3.688	3.641	0.608	± 0.062
3.688 – 3.794	3.741	0.691	± 0.061
3.794 – 3.912	3.853	0.599	± 0.048
3.912 – 4.034	3.973	0.361	± 0.032
4.034 – 4.166	4.100	0.308	± 0.020
4.166 – 4.268	4.217	0.379	± 0.063
4.268 – 4.382	4.325	0.273	± 0.048
4.382 – 4.491	4.436	0.356	± 0.043
4.491 – 4.605	4.548	0.169	± 0.032
4.605 – 4.710	4.657	0.184	± 0.027
4.710 – 4.828	4.769	0.185	± 0.021
4.828 – 4.933	4.880	0.111	± 0.014
4.933 – 5.035	4.984	0.041	± 0.007

Table 8.6: *differential kaon production cross section versus ξ_p for b events with statistical+systematic errors.*

ξ_p range	$< \xi_p >$	$1/N\ dN/d\xi_p$	$\Delta(1/N\ dN/d\xi_p)^{stat.+syst.}$
0.511 – 0.693	0.601	0.010	± 0.004
0.693 – 0.916	0.804	0.026	± 0.006
0.916 – 1.203	1.060	0.052	± 0.009
1.203 – 1.347	1.275	0.080	± 0.015
1.347 – 1.609	1.478	0.126	± 0.018
1.609 – 1.714	1.662	0.207	± 0.109
1.714 – 1.832	1.773	0.273	± 0.129
1.832 – 1.966	1.899	0.304	± 0.123
1.966 – 2.120	2.043	0.314	± 0.094
2.120 – 2.302	2.211	0.334	± 0.042
2.302 – 2.407	2.355	0.344	± 0.038
2.407 – 2.525	2.466	0.354	± 0.036
2.525 – 2.659	2.592	0.381	± 0.030
2.659 – 2.813	2.736	0.442	± 0.028
2.813 – 2.995	2.904	0.423	± 0.028
2.995 – 3.218	3.107	0.546	± 0.036
3.218 – 3.352	3.285	0.440	± 0.043
3.352 – 3.426	3.389	0.409	± 0.054
3.426 – 3.506	3.466	0.441	± 0.043
3.506 – 3.593	3.550	0.344	± 0.045
3.593 – 3.688	3.641	0.530	± 0.051
3.688 – 3.794	3.741	0.342	± 0.033
3.794 – 3.912	3.853	0.426	± 0.049
3.912 – 4.034	3.973	0.242	± 0.010
4.034 – 4.166	4.100	0.196	± 0.008
4.166 – 4.268	4.217	0.103	± 0.039
4.268 – 4.382	4.325	0.078	± 0.049
4.382 – 4.491	4.436	0.000	± 0.000
4.491 – 4.605	4.548	0.068	± 0.008
4.605 – 4.710	4.657	0.058	± 0.005
4.710 – 4.828	4.769	0.042	± 0.003

Table 8.7: *differential proton production cross section versus ξ_p for b events with statistical+systematic errors.*

8.2.2 Rapidity, x_p, p, p_t^{in} and p_t^{out} production spectra

Some relevant track kinematical quantities have been measured for identified π^+ $K^\pm$ and p in light quarks and heavy quark samples. For hadronic events one normally defines the main event-shape variables to characterize the final states produced after the Z decay and fragmentation.
The *Thrust* is defined as

$$T \equiv max_{\vec{t_1}} \frac{\sum_{i=1}^{N} |\vec{p_i} \cdot \vec{t_1}|}{\sum_{i=1}^{N} |\vec{p_i}|} \tag{8.4}$$

where the sum is intended on all tracks in the event.
A perfect spherically symmetrical events has $T = 1/2$, while a totally back-to-back event has $T = 1$. This equation defines at the same time therefore a geometrical direction in space (given by the unit vector $\vec{t_1}$) and a corresponding scalar number between 0 and 1 measuring the directionality of the event itself.

The *Sphericity Tensor* is given by the equation

$$S^{ij} \equiv \frac{\sum_{k=1}^{N} p_k^i \, p_k^j}{\sum_{k=1}^{N} |p_k|^2} \tag{8.5}$$

where i, j are the x, y, z components of the particle ($k = 1, ..N$ momentum. The eigenvalues of the sphericity tensor are usually indicated as $\lambda_1 \geq \lambda_2 \geq \lambda_3$ and sum up to 1 : $\lambda_1 + \lambda_2 + \lambda_3 = 1$.
The corresponding eigenvectors $\vec{s_1}$, $\vec{s_2}$ and $\vec{s_3}$ are such that $\vec{s_1}$ and $\vec{s_2}$ define the *event plane*, respectively along the *event axis* and the *in-axis*.
The third eigenvector $\vec{s_3}$ direction defines the *out-axis*.
The *Sphericity* of the event is a scalar quantity defined starting from them as

$$S \equiv \frac{1}{2}(\lambda_2 + \lambda_3) \tag{8.6}$$

Sphericity is always $0 \leq S \leq 1$, with $S = 0$ for a perfect "back-to-back" event and $S = 1$ for a completely symmetrical event.

- The *rapidity* $|y|$ (with respect to the Thrust axis direction) is used to describe the longitudinal momentum distribution with respect to the event axis. It is defined as

$$y \equiv \frac{1}{2} ln(\frac{E + p_{\|}}{E - p_{\|}}) \tag{8.7}$$

- The *major* is defined as

$$M_{Major} \equiv max_{\vec{t2} \perp \vec{t1}} \frac{\sum_{i=1}^{N} |\vec{p_i} \cdot \vec{t_2}|}{\sum_{i=1}^{N} |\vec{p_i}|} \tag{8.8}$$

- Orthogonal to the Thrust and Major axis lays the *Minor* axis, given by

$$M_{Minor} \equiv \frac{\sum_{i=1}^{N} |\vec{p_i} \cdot \vec{t_3}|}{\sum_{i=1}^{N} |\vec{p_i}|} \tag{8.9}$$

The two momentum variables p_t^{in} and p_t^{out} are defined as the track momentum in the direction of the Major and Minor axis respectively.
They are used to further describe the track momentum distribution, outside the Thrust direction.

The result of this analysis relative on the production normalized momentum spectra are shown by figures 8.9 to 8.12 for π^+ $K^\pm$ and p in light quark and b quark events (for the observable p_t^{in}) and 8.13 to 8.16 (for the observable p_t^{out}).

The relative amount of π^+ $K^\pm$ and p with respect to all charged particles versus momentum is shown by figures 8.8 for uds and b tagged events.
The total production cross sections are shown by picture 8.7.

8.2.3 π^+, $K^\pm$ and p multiplicities

The average multiplicities of π^+, $K^\pm$ and p have been measured through a fit of various kinematical variables in the available measured range and the result have been compared with the predictions of the Montecarlo generators JETSET 7.4, ARIADNE 4.08, HERWIG 58 C.
The three variables ξ_p, ξ_E and rapidity have been fitted and the integral of the fitted function on the allowed kinematical range provided the particle multiplicities.
As above mentioned, ξ_p has been fitted to a modified gaussian function, ξ_E to a polynomial (order 5 for pion, 4 for kaons and protons) multiplied by an exponential factor.
The Rapidity distributions have been fitted to a polynomial expression of order 9.
The result of the inverse error weighted averages are reported in table 8.9.

(uds)	data (ξ_p fit)	JETSET fit	JS	HERWIG fit	HW	ARIADNE fit	AR
π^+	16.8 ± 0.4	16.3 ± 0.2	16.5	15.7 ± 0.3	16.1	16.4 ± 0.4	16.8
K^+	2.30 ± 0.08	2.20 ± 0.03	2.15	1.76 ± 0.03	1.80	1.94 ± 0.03	1.97
p	1.01 ± 0.05	1.06 ± 0.01	1.06	0.68 ± 0.04	0.70	1.01 ± 0.02	1.03
(b)	data (ξ_p fit)	JETSET fit	JS	HERWIG fit	HW	ARIADNE fit	AR
π^+	17.9 ± 0.6	19.2 ± 0.5	19.6	18.8 ± 0.3	19.05	17.85 ± 0.3	18.31
K^+	2.62 ± 0.11	2.77 ± 0.06	2.85	2.83 ± 0.07	2.85	2.39 ± 0.04	2.42
p	0.84 ± 0.05	0.82 ± 0.02	0.80	0.61 ± 0.02	0.61	0.96 ± 0.02	0.94
(uds)	data (ξ_E fit)	JETSET fit	JS	HERWIG fit	HW	ARIADNE fit	AR
π^+	16.7 ± 0.5	16.8 ± 0.4	16.5	16.3 ± 0.4	16.1	16.8 ± 0.7	16.8
K^+	2.21 ± 0.09	2.23 ± 0.07	2.15	1.78 ± 0.05	1.80	1.93 ± 0.05	1.97
p	1.00 ± 0.06	1.06 ± 0.05	1.06	0.76 ± 0.04	0.70	1.01 ± 0.04	1.03
(b)	data (ξ_E fit)	JETSET fit	JS	HERWIG fit	HW	ARIADNE fit	AR
π^+	18.1 ± 0.7	19.2 ± 0.7	19.6	18.7 ± 0.6	19.05	18.1 ± 0.6	18.31
K^+	2.67 ± 0.10	2.84 ± 0.08	2.85	2.84 ± 0.04	2.85	2.37 ± 0.05	2.42
p	0.91 ± 0.10	0.087 ± 0.08	0.80	0.63 ± 0.04	0.61	0.97 ± 0.05	0.94
(uds)	data ($\|y\|$ fit)	JETSET fit	JS	HERWIG fit	HW	ARIADNE fit	AR
π^+	16.9 ± 0.5	16.4 ± 0.4	16.5	15.6 ± 0.5	16.1	16.8 ± 0.3	16.8
K^+	2.16 ± 0.08	2.24 ± 0.06	2.15	1.92 ± 0.05	1.80	2.20 ± 0.06	1.97
p	1.06 ± 0.08	1.04 ± 0.06	1.06	0.72 ± 0.04	0.70	1.01 ± 0.05	1.03
(b)	data ($\|y\|$ fit)	JETSET fit	JS	HERWIG fit	HW	ARIADNE fit	AR
π^+	18.5 ± 0.5	19.2 ± 0.4	19.6	18.9 ± 0.4	19.05	18.8 ± 0.5	18.31
K^+	2.70 ± 0.11	2.83 ± 0.06	2.85	2.89 ± 0.06	2.85	2.45 ± 0.06	2.42
p	0.88 ± 0.12	0.86 ± 0.07	0.80	0.62 ± 0.06	0.61	0.90 ± 0.06	0.94

Table 8.8: *multiplicities for π, K and p from the modified gaussian fit of the ξ_p distributions, the exponential-polynomial fit of the ξ_E distributions and the polynomial fit of the rapidity ($|y|$) distributions. On the right of each MC generator fit result, the generated original value is shown.*

(uds)	DATA AVERAGE	JETSET 7.4 PS	HERWIG 58C	ARIADNE 4.08
π^+	16.8 ± 0.4	16.5	16.1	16.8
K^+	2.22 ± 0.07	2.15	1.80	1.97
p	1.02 ± 0.05	1.06	0.70	1.03
(b)	DATA AVERAGE	JETSET 7.4 PS	HERWIG 58C	ARIADNE 4.08
π^+	18.2 ± 0.5	19.6	19.05	18.31
K^+	2.66 ± 0.10	2.85	2.85	2.42
p	0.87 ± 0.10	0.80	0.61	0.94

Table 8.9: *multiplicities for π, K and p from the inverse-error weighted average of the data and for the each MC generators*

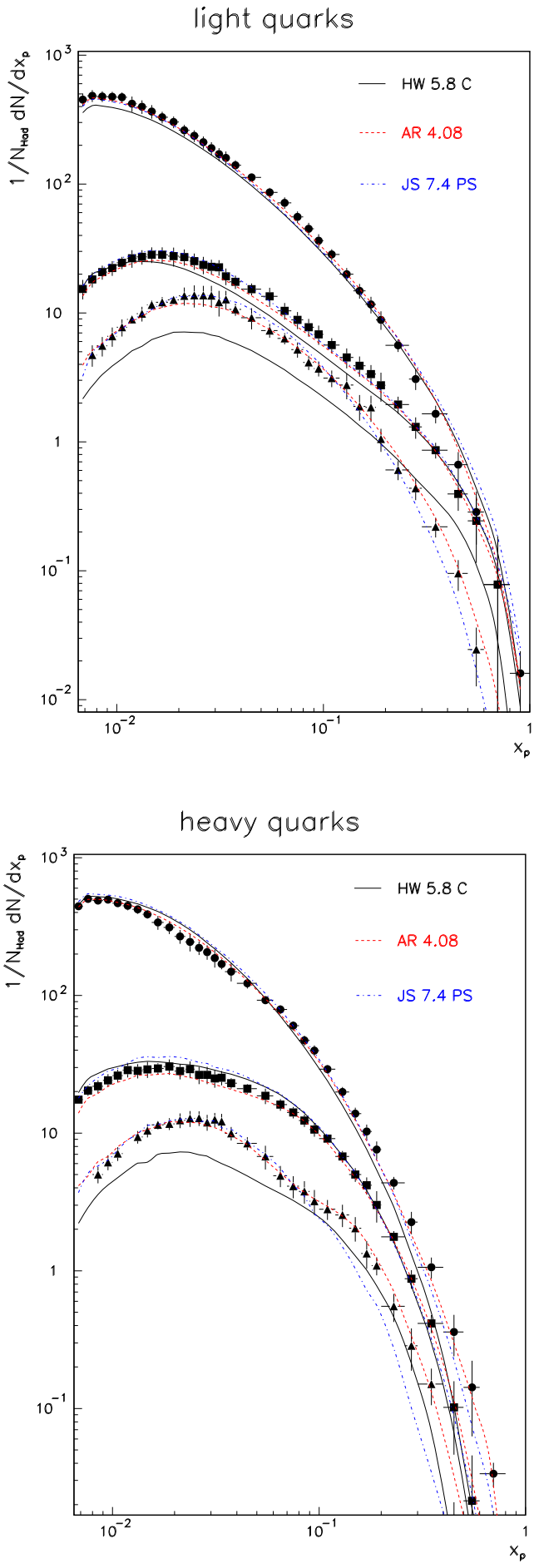

Figure 8.7: *Differential production rates for pion, kaon and proton in uds (above) and b (below) tagged events.*

8.3 Systematic Error Analysis

The following sources of systematic errors on the measurements relative to the hadronic identification and b tagging analysis have been investigated:

- Error on the tagging efficiencies
- Error on the secondary tracks correction factor
- Error on the Leptonic contribution (e^-,μ^-) correction factor
- Error induced by the sphericity angle cut
- Error induced by the acceptance corrections
- Error on the ghost tracks correction factor
- Error on the global tag-acceptance correction factor
- Error on the b tagging purities (P^{uds} and P^b)

In this section each of these contributions is discussed, focusing on the order of magnitude of the systematic error and its origin.

- **Tagging efficiency** For each bin, the systematic error due to the (statistic and systematic) uncertainty on the tagging efficiencies (ϵ_k^i) in the bin has been taken into account. The statistic error is the Poissonian error deriving from the given tagged and total samples of tracks, and an indication on the systematic error has been obtained by the use of selected samples (in particular Λ and K^0), who provided a minimal constant error of about 3% on the whole range for all the 9 efficiencies.
  The tag efficiency error represents generally the biggest contribution to the whole systematic error, even if it is very momentum dependent. Its relative fluctuations are of the order of 80 % depending on the tag and the given observable bin.
  On average roughly 50 % of the systematic error alone comes from the tag efficiency uncertainty.

- **Secondary tracks correction factor** The error due to the secondary tracks correction factor has been included into the systematic error. This error is coming on the uncertainty on the corresponding correction factor, that is a systematic uncertainty (data/MC disagreement) and a statistical uncertainty. The systematics has been assumed to be of the order of 0.5 %, as suggested by the global tag acceptance efficiency disagreement in data-Montecarlo.

- **Leptonic contribution (e^-,μ^-) correction factor** The systematic error due to the uncertainty in the electronic and muonic background is very momentum dependent.
  In the momentum region around 0.5 GeV/c for kaons and 0.8 GeV/c for protons, the corrections factor is relatively big (up to some percent). Its effects on the total systematic error however never exceed 1 %.

- **Sphericity Angle** the Sphericity angle cuts have been varied of $\pm$ 4°, to see the effects of the global event shape influence on the hadronic measured samples. Due to the fact that the efficiency matrix has been calculated twice for uds and b events, the event shape effects possibly related to the original quark flavour contribute very little to the systematic error, of the order of $2-3$ % of the total systematic error.

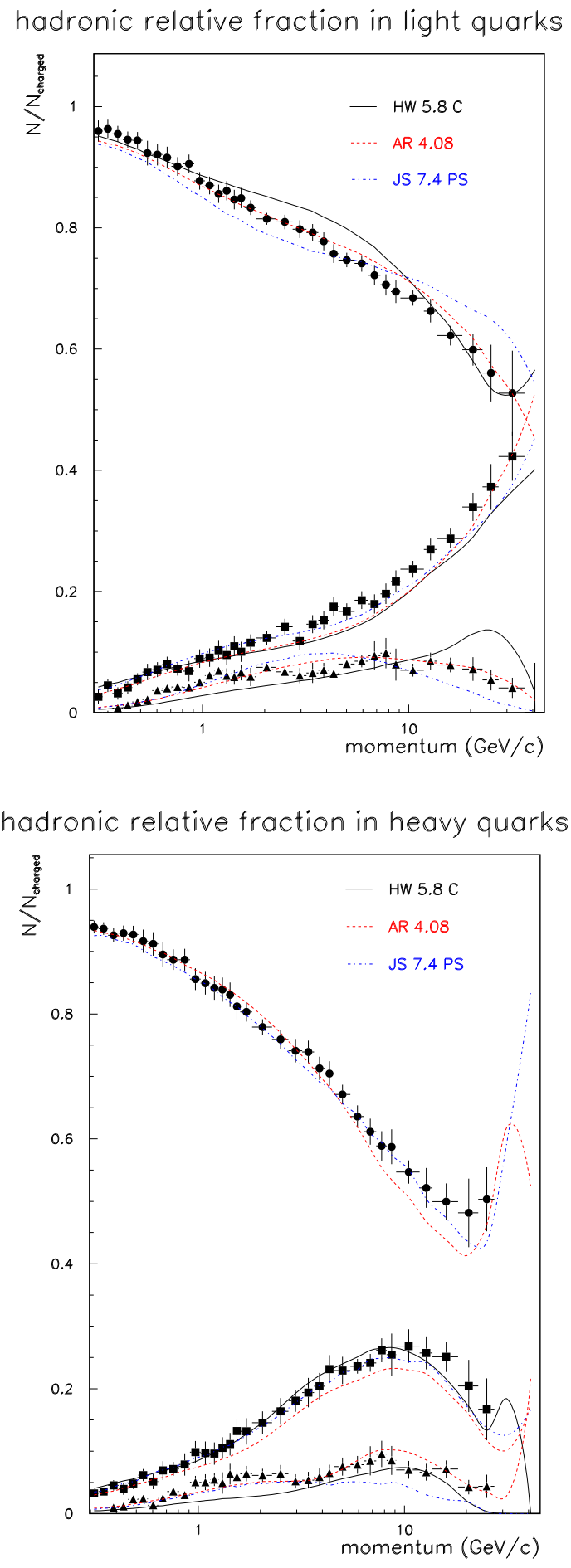

Figure 8.8: *Charged fraction of pion, kaon and proton in uds (above) and b (below) tagged events*

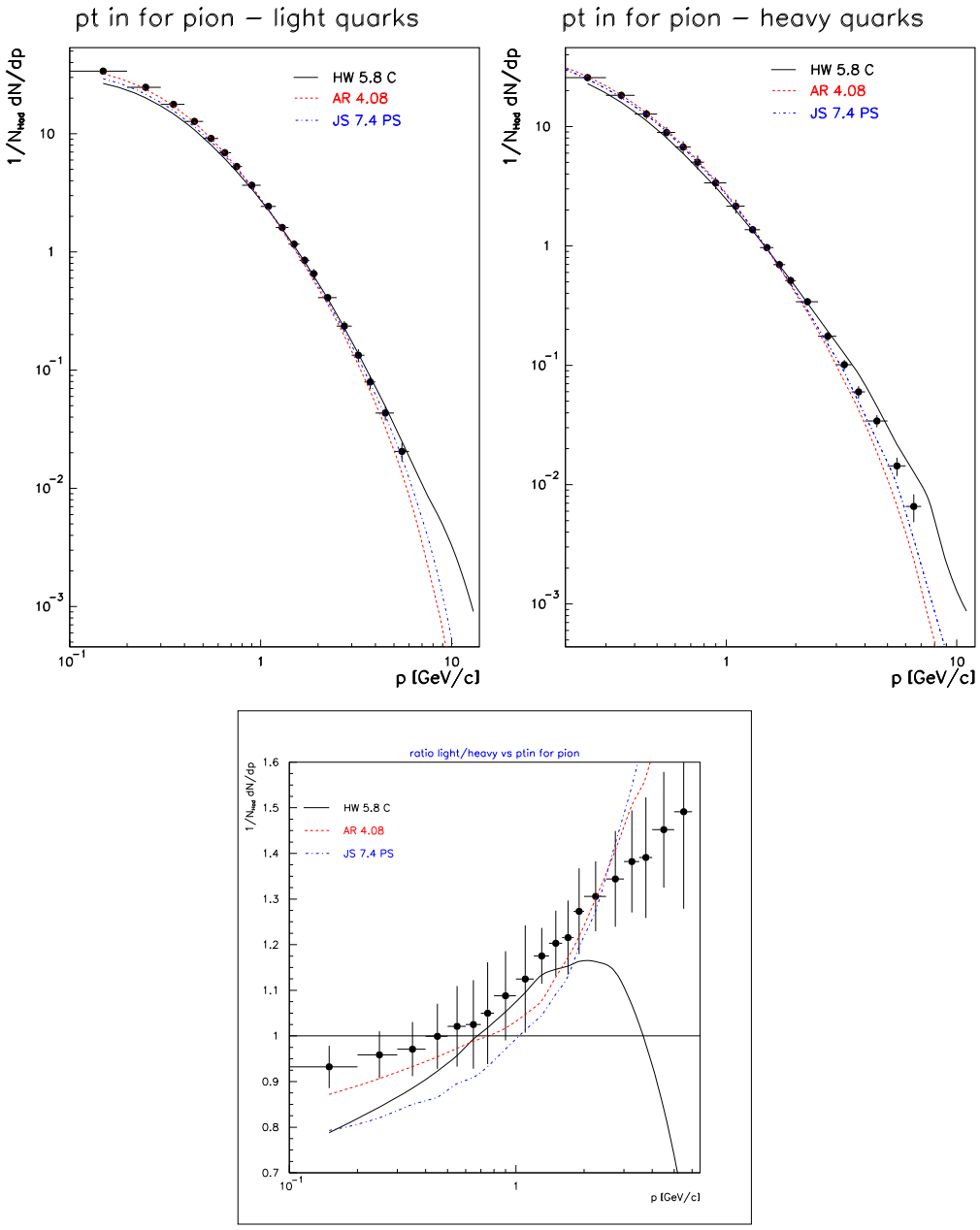

Figure 8.9: *p_t^{in} spectrum for π^+ in light (left) and heavy (right) quark Z decay events. Below the ratio light to heavy is shown*

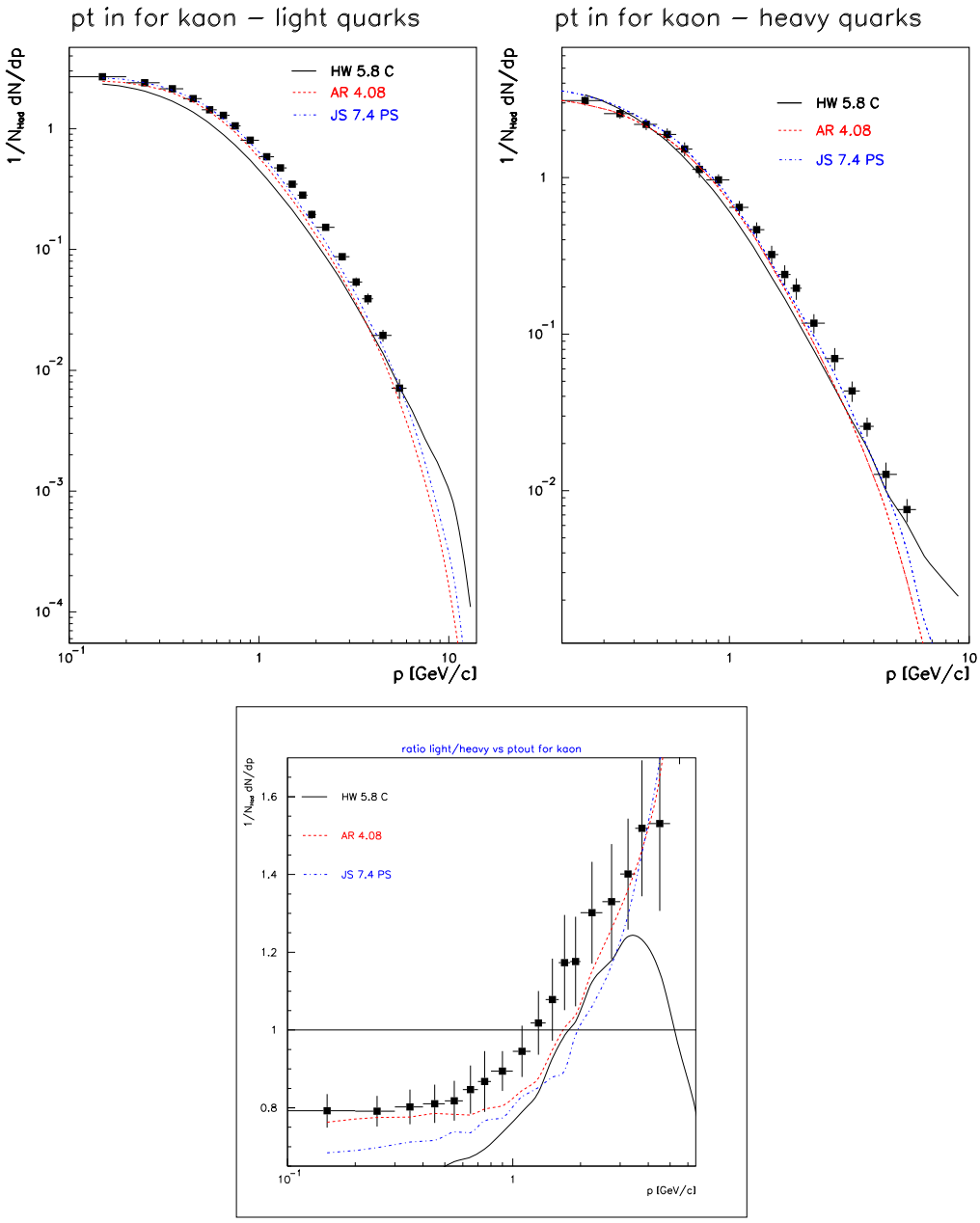

Figure 8.10: *p_t^{in} spectrum for K^+ in light (left) and heavy (right) quark Z decay events. Below the ratio light to heavy is shown*

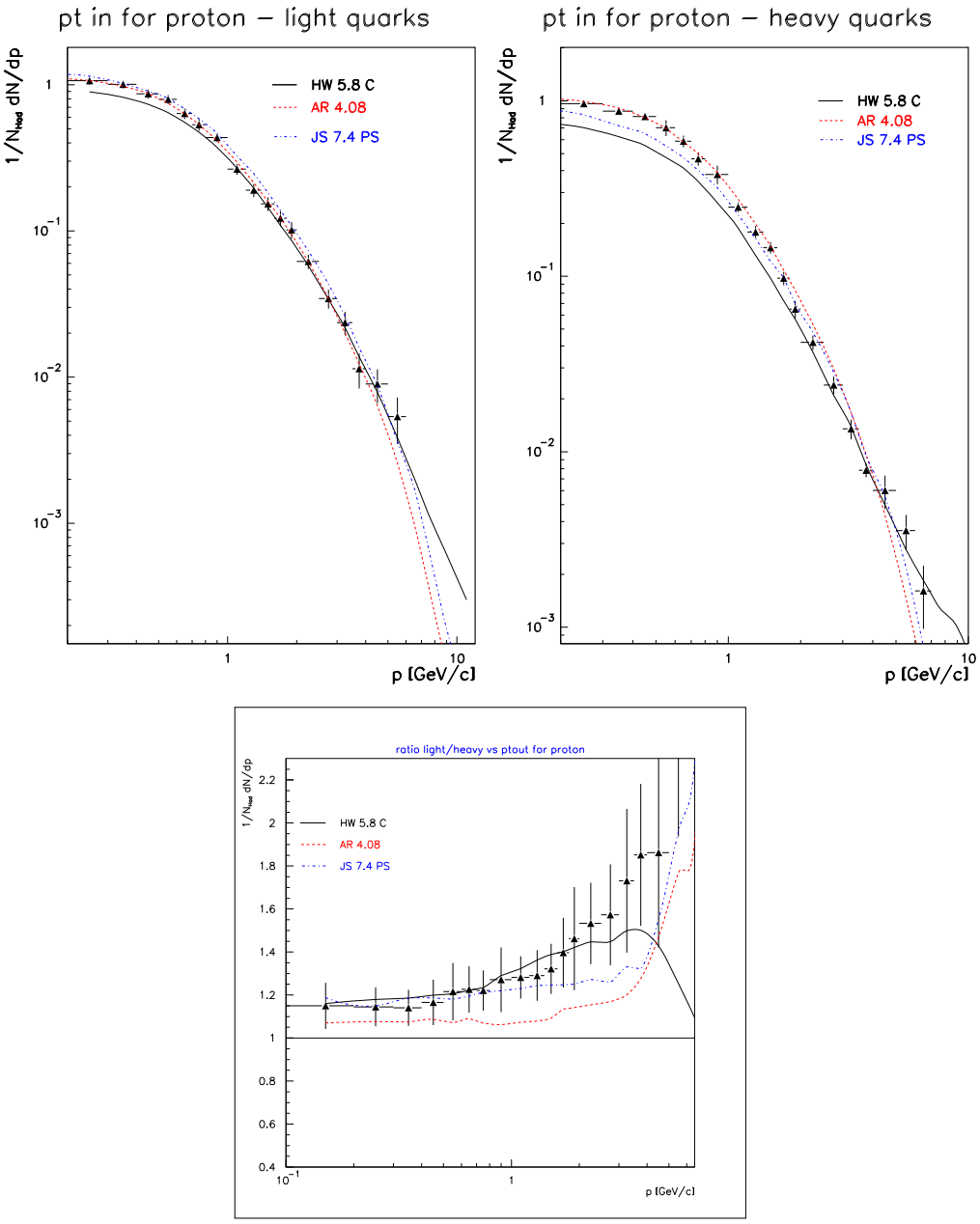

Figure 8.11: *p_t^{in} spectrum for p in light (left) and heavy (right) quark Z decay events. Below the ratio light to heavy is shown*

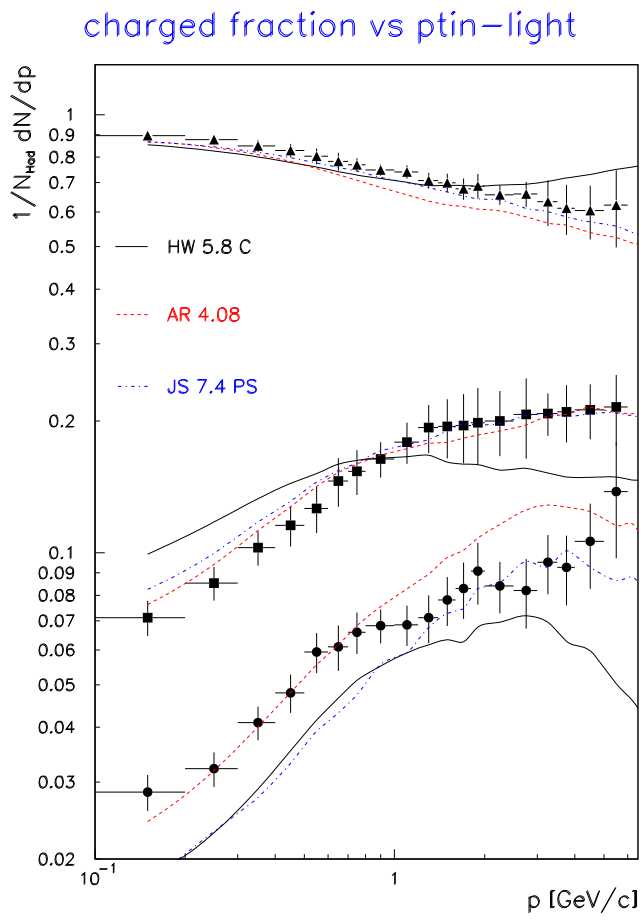

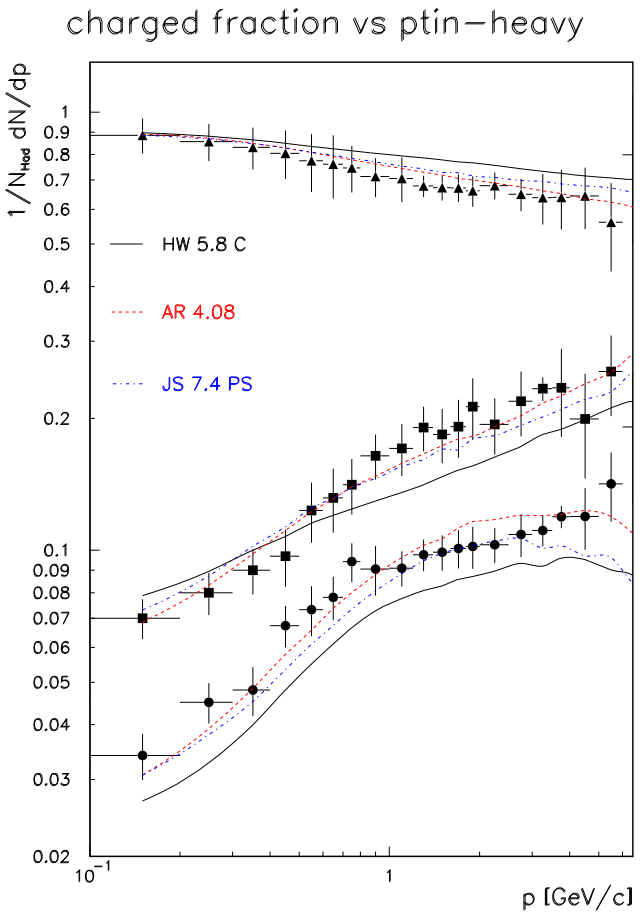

Figure 8.12: *relative fraction with respect to all charged versus p_t^{in} for π^+, K^+ and p in light (above) and heavy (below) quarks*

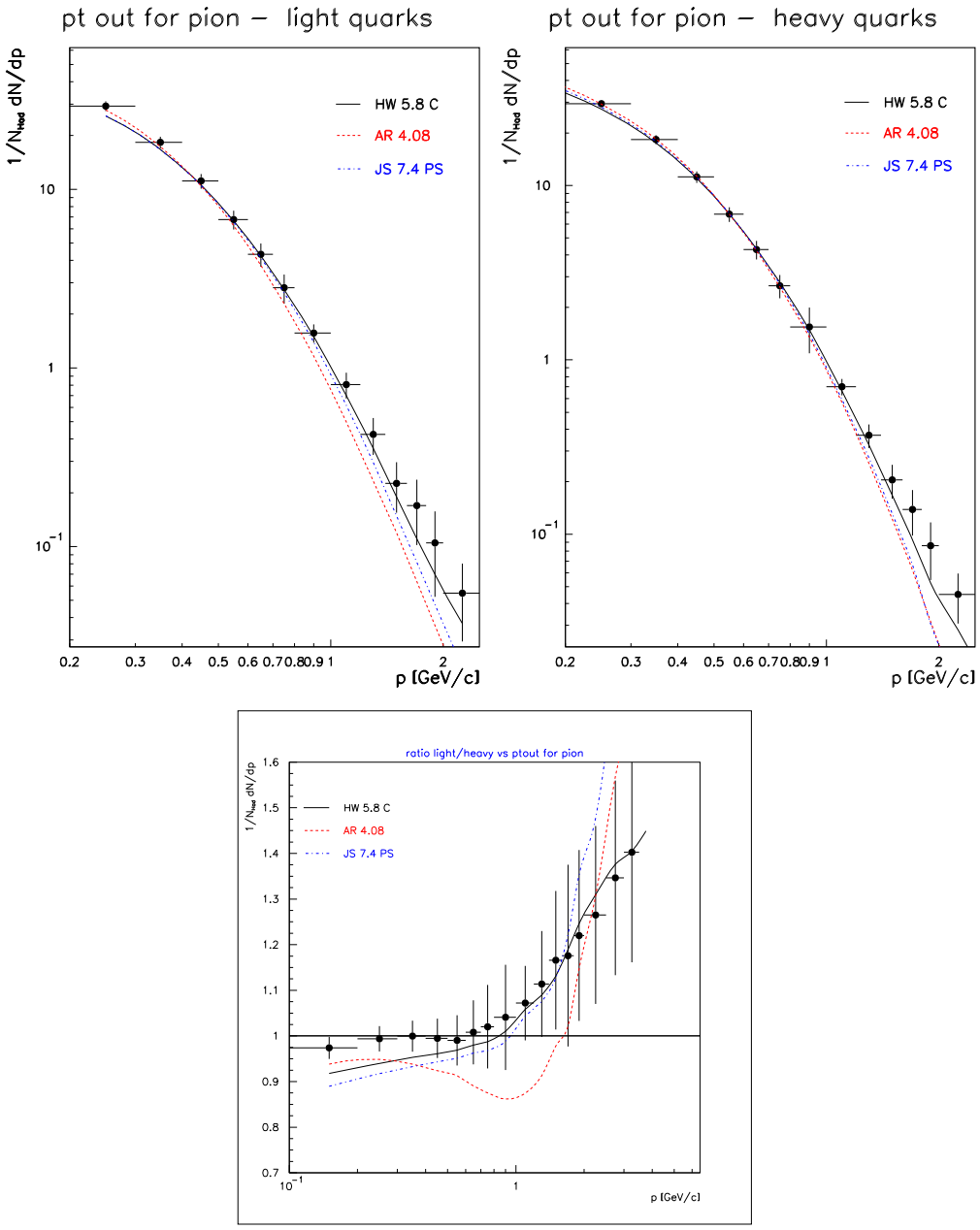

Figure 8.13: *p_t^{out} spectrum for π^+ in light (left) and heavy (right) quark Z decay events. Below the ratio light to heavy is shown*

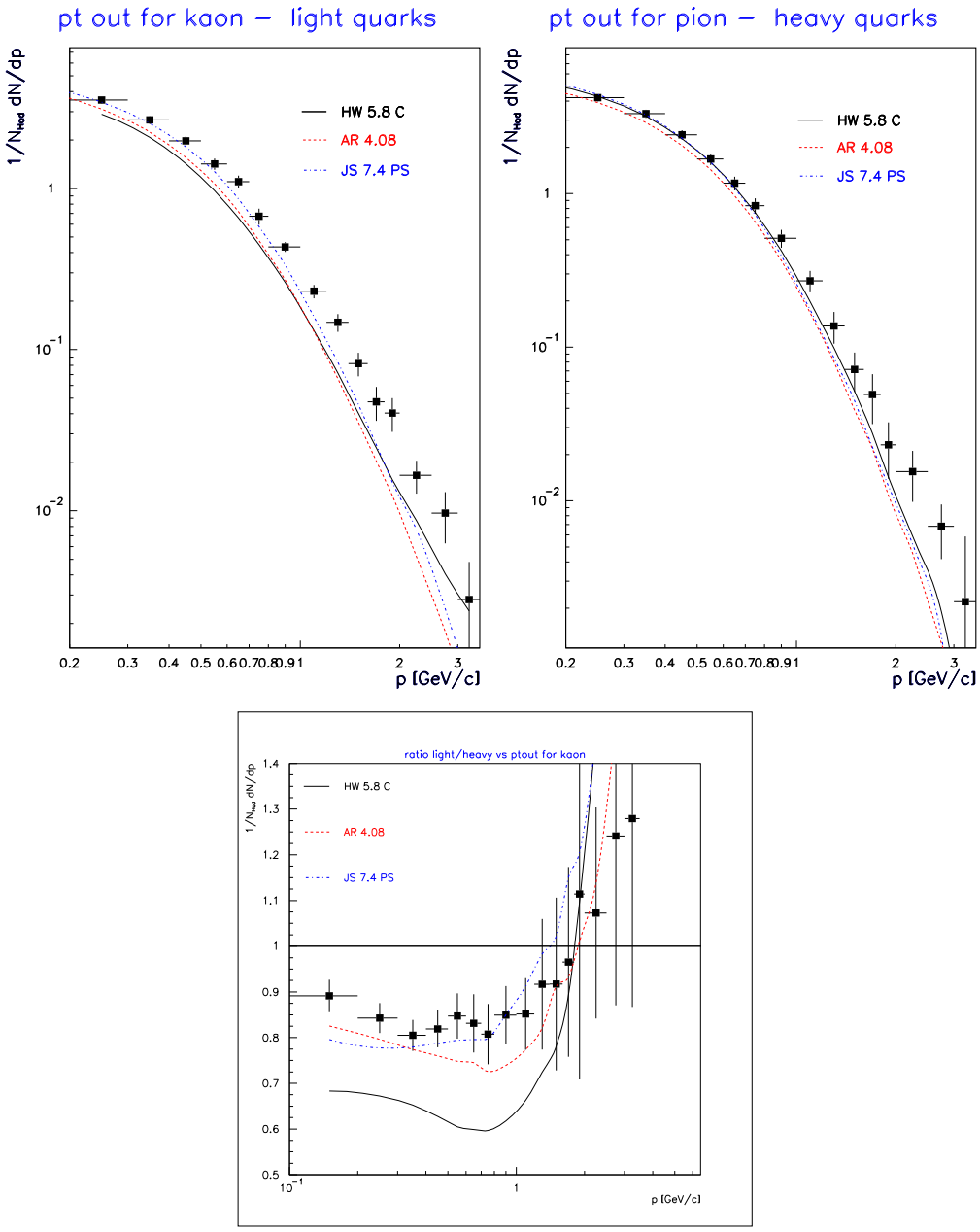

Figure 8.14: *p_t^{out} spectrum for K^+ in light (left) and heavy (right) quark Z decay events. Below the ratio light to heavy is shown*

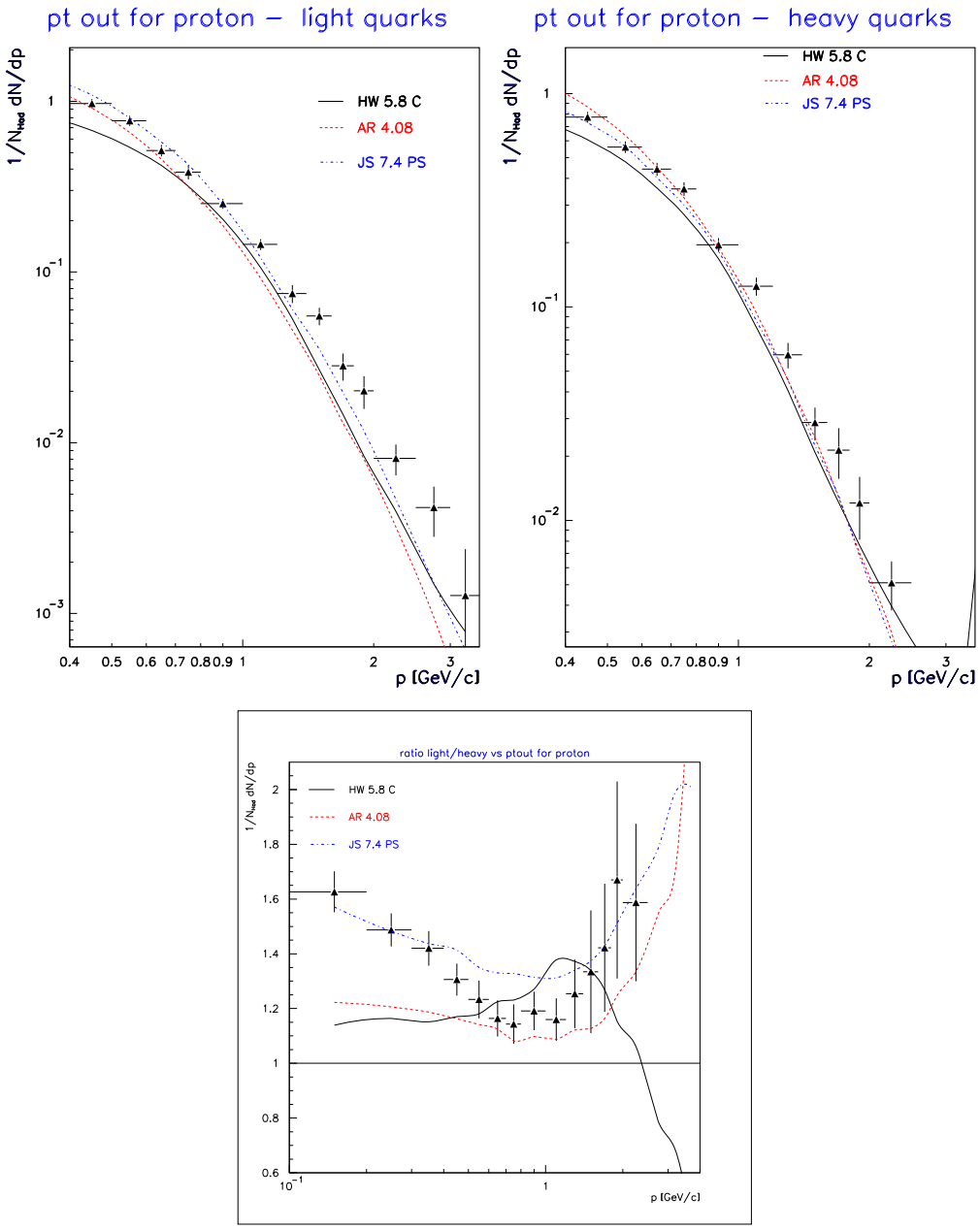

Figure 8.15: *p_t^{out} spectrum for p in light (left) and heavy (right) quark Z decay events. Below the ratio light to heavy is shown*

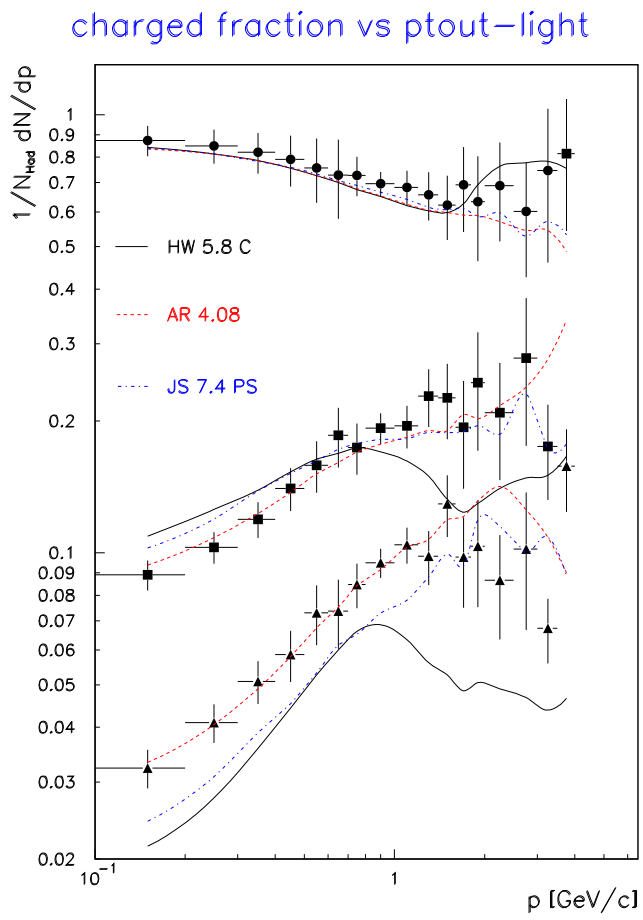

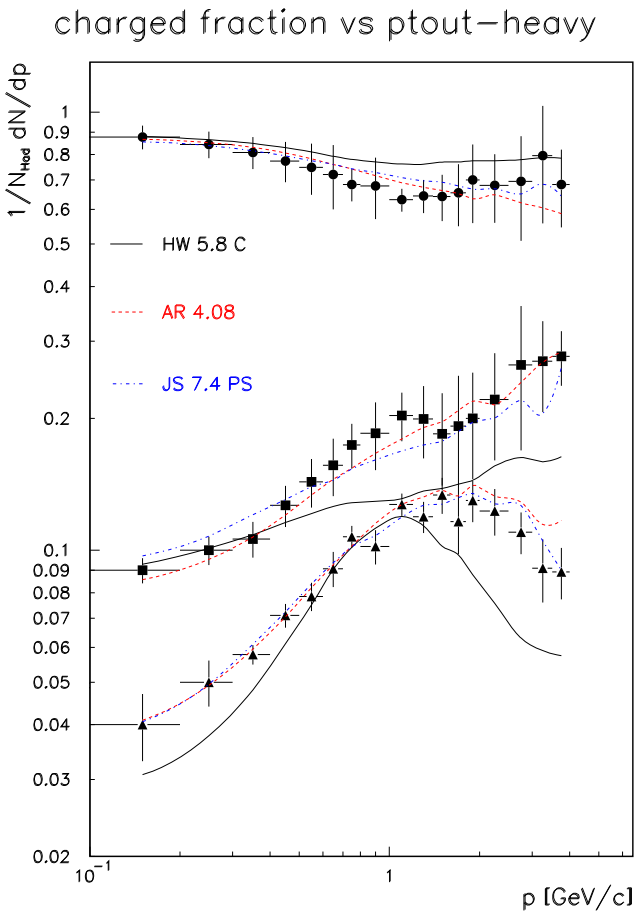

Figure 8.16: *relative fraction with respect to all charged versus p_t^{out} for π^+, K^+ and p in light (above) and heavy (below) quarks*

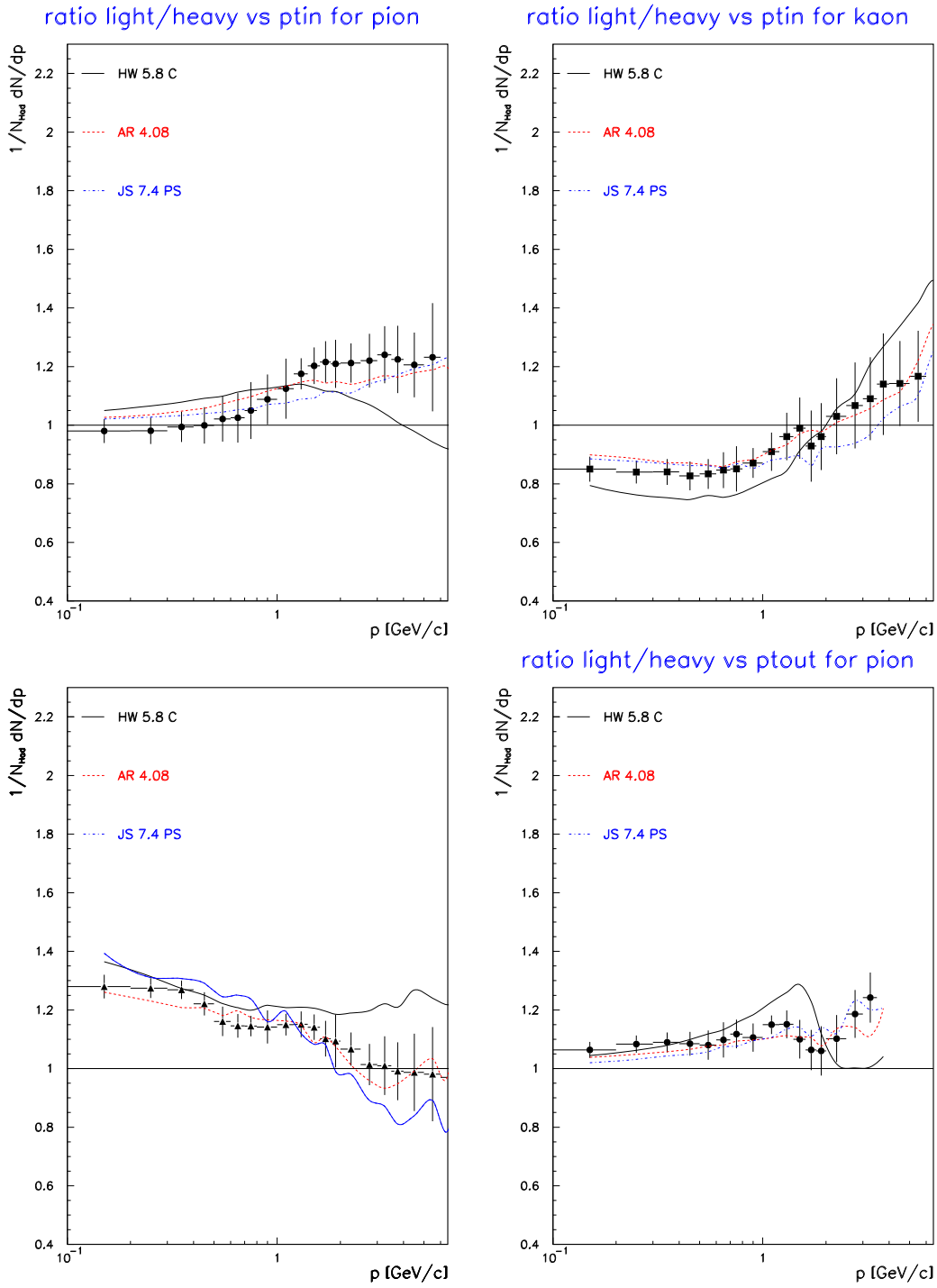

Figure 8.17: *Above: relative fraction with respect to all charged versus p_t^{in} for π^+ (left) and K^+ (right) : ratio light to heavy quarks. Below: Ratio light to heavy quarks for the relative fraction with respect to all charged versus p_t^{in} for p (left) and versus p_t^{out} for π^+ (right)*

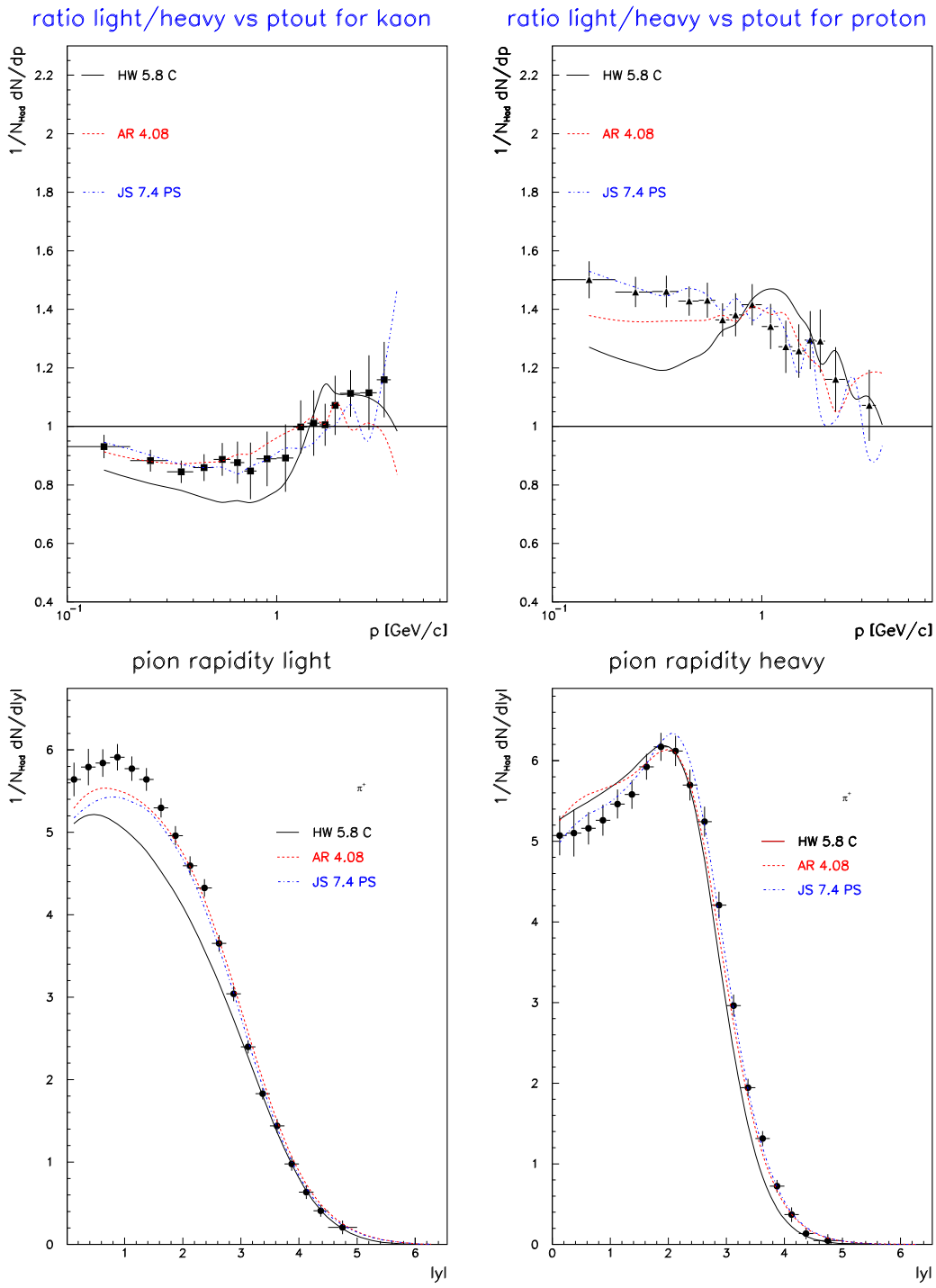

Figure 8.18: *Above: ratio light to heavy for the relative charged fraction vs p_t^{out} for K^+ (left) and p (right). Below: Rapidity distributions for π^+ in light (left) and heavy (right) quark Z decay events. (points are data).*

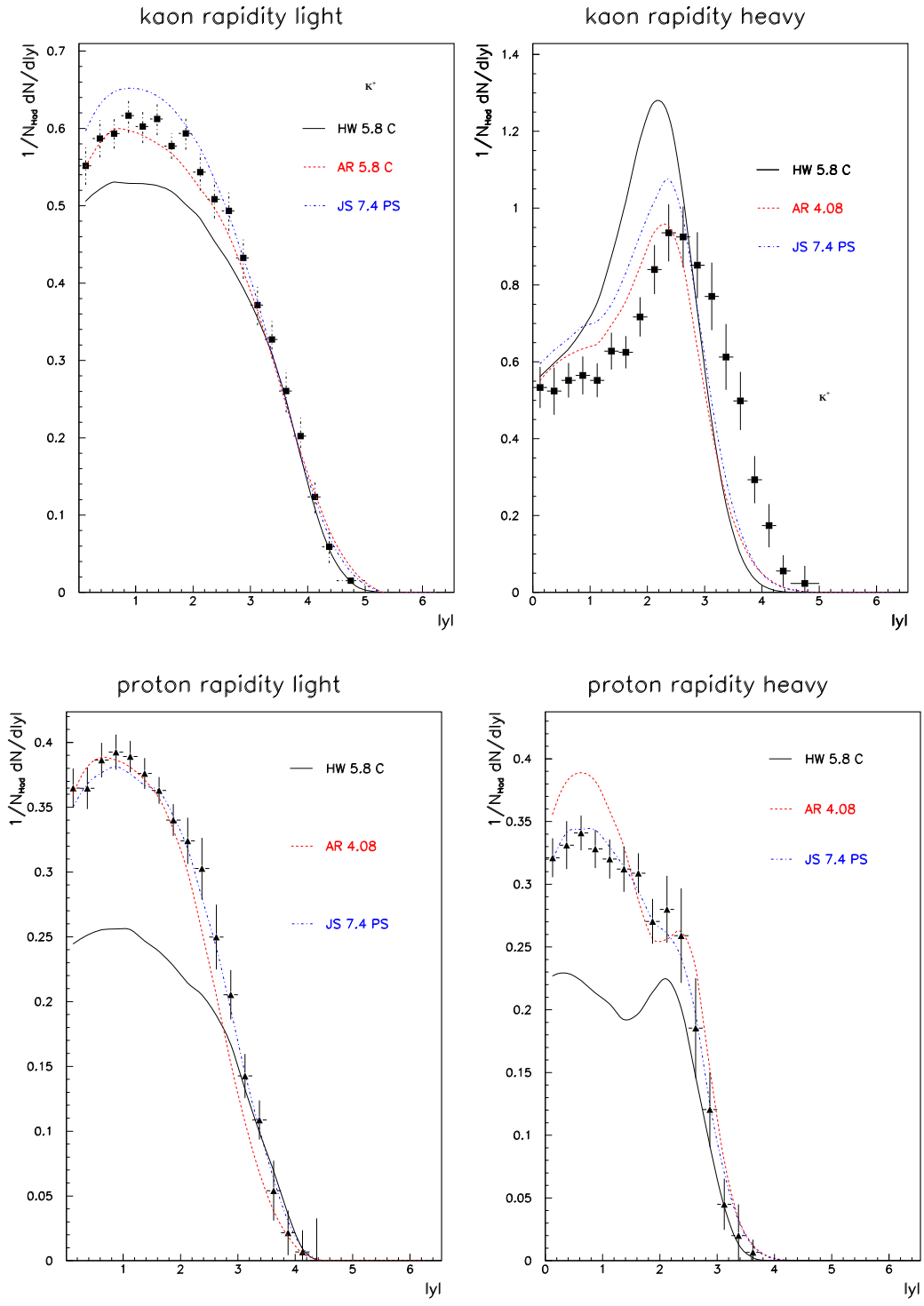

Figure 8.19: *rapidity spectrum for K^+ (above) and p (below) in light (left) and heavy (right) quark Z decay events.*

- **Acceptance corrections** The Error induced by the acceptance corrections has been evaluated by propagation of the corresponding correction factor statistical error and by considering a relative error on the acceptance correction factor given by $\pm$ 5 % of its value.

- **Ghost tracks** Ghost tracks are the badly reconstructed tracks by the DELANA (DELPHI tracking) program. The effect of the ghost tracks on the systematic error is on average of the order of 1 % of the total systematic error.

- **Global tag acceptance** To cope with slight differences between the DATA and MONTECARLO efficiency measurements due to different tag acceptance behaviour in both samples, a global contribution error of $\pm$ 5% has been taken into consideration, since of this order or magnitude is the global acceptance disagreement and the necessary corrections applied. This errors reflected therefore in the systematic contribution brought by the error on the correction factor applied bin by bin

$$f = \frac{(tot.n.charg.tracks\ in\ input\ to\ the\ tag)/(tot.n.tagged\ tracks)_{DATA}}{(tot.n.charg.\ tracks\ in\ input\ to\ the\ tag)/(tot.n.tagged\ tracks)_{MC}} \qquad (8.10)$$

- **b-tagging** The possible source of systematic errors on the measurements due to the b tagging has been summarized into an error on the b tagging purities for the two samples. The error on the b-tagging purity in the two samples has been measured by varying the b-probability cut from the central values $P_{uds}^{cut} = 0.6$ to 0.5 and 0.7 and $P_b^{low} = 0.01$ to 0.007 and 0.015 and performing the fraction analysis again, to measure the change in the production spectra.
  These values have been chosen to be compatible with the uncertainty on the Purity given by the data-montecarlo disagreement on tracking, impact parameter and track perigee parameters.

Chapter 9

Summary and Conclusions

9.1 Summary

In This Analysis the inclusive production spectra for charged pion, charged kaon and protons have been measured in a u, d, s quark enriched sample and a b quark enriched sample of $e^+e^- \rightarrow Z \rightarrow hadrons$ decays.
The combined use of the DELPHI Cherenkov detector, the Time Projection Chamber and the MicroVertex detector allowed the investigation of the effects of the originary quark flavour on the fragmentation process and the final states spectra.

The average particle multiplicities for $\pi^{\pm}$, $K^{\pm}$ and $p\overline{p}$ per hadronic event have been measured in light quark events to be $< n_{\pi^{\pm}} >_{uds} = 16.8 \pm 0.4$, $< n_{K^{\pm}} >_{uds} = 2.22 \pm 0.07$ and $< n_{p/\bar{p}} >_{uds} = 1.02 \pm 0.05$, and in heavy quark events to be $< n_{\pi^{\pm}} >_b = 18.2 \pm 0.5$, $< n_{K^{\pm}} >_b = 2.66 \pm 0.10$ and $< n_{p/\bar{p}} >_b = 0.87 \pm 0.10$.
The ξ_p^* values were found to be $\xi_{\pi^{\pm}}^{*,uds} = 3.88 \pm 0.08$, $\xi_{K^{\pm}}^{*,uds} = 2.86 \pm 0.09$ and $\xi_{p\bar{p}}^{*,uds} = 2.77 \pm 0.09$ in light quark events and $\xi_{\pi^{\pm}}^{*,b} = 3.71 \pm 0.08$, $\xi_{K^{\pm}}^{*,b} = 2.54 \pm 0.16$ and $\xi_{p\bar{p}}^{*,b} = 2.95 \pm 0.16$ in b quark events.
The transverse momentum spectra inside and outside the event plane have been measured for $\pi^{\pm}$, $K^{\pm}$ and $p\overline{p}$ for both classes of events. HERWIG does not describe correctly the high momentum part of the p_t^{in} spectra and all generators have problems to describe the p_t^{out} spectra, in both classes of events. The rapidity spectra have been measured, showing that HERWIG (cluster fragmentation) is the generator with the most problems in describing them correctly.

9.2 Conclusions

Given the results of this analysis, the following considerations are possible:

- On average b events show higher multiplicities for pions (+8.3 %) and kaon (+19.8 %) and lower multiplicity for proton (−15 %) with respect to light uds quark events. The increase in the pion and kaon multiplicities in b events is expected because of the B and D hadrons decay chains.

- Increase in the kaon production can clearly be observed in the inclusive kaon fraction in all charged tracks versus momentum and in the differential cross section plots.

- Due to particle decays, the rapidity spectra look very different for the two categories of events. The b tagged events tend to peak at higher rapidity, and this effect is mostly visible in the kaon spectra, due to B hadrons decays. HERWIG is not able to describe correctly the spectra, apart in the case of the pion in b events, around the peak region. Its deviation from the measured values ranges from few percent (in general in the high rapidity region) up to almost 60-70 percent in the lower rapidity region, corresponding sometimes up to 3 or 4 standard deviations away from the measured value. This could reflect a lack in the cluster model, not taking correctly enough into account the longitudinal momentum distributions of the generated stable hadrons. The kaon rapidity in b quark events shows that the B hadrons decay products have somewhat higher rapidities than the one simulated by the models in the MonteCarlo generators.

- The p_t^{in} spectra are in general agreement with the generators, even though HERWIG has the tendency to underestimate the spectra and is unable to describe the ratio uds to b. The distribution of p_t^{in} for proton shows that HERWIG underestimates the rates at low momentum by $\simeq$ 20 %, whereas in the same region ARIADNE is in best agreement with the data.

- The p_t^{out} spectra show a general disagreement between the data and the generators in both categories of events in the high momentum region, the measured spectra being on average harder than the predictions of the models.
  In the low momentum region JETSET and ARIADNE are compatible with the data, while HERWIG systematically underestimates them. The fact that the disagreement effects both classes of events suggests that this is a limit of the models themselves, instead of a lack in the simulation of the effects of B hadrons decays on the p_t^{out} spectra. Soft gluon radiation and fragmentation effects could cause the measured p_t^{out} values to be different from the simulated ones by the generators.

- The measured ξ_p^* positions are compatible with all the models predictions, apart from the case of kaon in light quark and proton in heavy quark events. In both these cases HERWIG is not compatible, and ARIADNE has also problems, being outside the experimental measured range for kaons in light quarks.

  In the light quark sample, where the effects of the particle decays are in general smaller than in the b quark sample (and therefore it is easier to test the prediction of LPHD+MLLA, who relates the partonic to the primary produced hadronic spectra), the behavior of the measured ξ_p^* versus the hadron mass is decreasing with the hadron mass. ($(\xi_p^{*,uds})_{K^+} = 2.86 \pm 0.09 > (\xi_p^{*,uds})_p = 2.77 \pm 0.09$).

  This is anyhow not enough to support the MLLA+LPHD prediction of a $\simeq -log(M^{hadron})$-like unique behaviour for mesons and baryons, as it is shown by figure 8.2.

  The LPHD+MLLA predictions on the ξ_p^* dependence versus the centre of mass energy $\sqrt{s}$ found by the analysis in [67] cannot be confirmed neither excluded since they refer

to all-quark flavors samples, and it is therefore not possible to compare the results. The only thing emerging here about this subject is that the proton-kaon shift found by the DELPHI all-flavors analysis ([66]) is confirmed in both *uds* and *b* events. This shift seems to be inconsistent with the results of the fit reported in [67].

The measured values in *b* quark events clearly show that the effects of hadron decays do not allow the investigation of the naive LPHD+MLLA predictions on ξ_p^* for primary produced (fragmentation) hadrons in presence of large heavy decay products.

- The measured multiplicities are better described by JETSET. JETSET has problems only by the π^+ in *b* events, where is seems to overestimate the measured value. HERWIG is always underestimating the measured multiplicities, apart from π^+ and K^+ in *b* events, where it overestimates them. ARIADNE has problems with kaons in both cases, where it underestimates the multiplicity.
- The fraction of p with respect to all charged stable particles shows that HERWIG does not describe correctly the high momentum proton spectra in light quark events. In *b* quark events, again HERWIG has problem to describe the proton spectrum and ARIADNE the pion spectrum.

9.3 Aknowledgments

I would like to start by thanking sincerely Professor Jürgen Drees, who gave me the possibility to work in this group. Then I need to thank Dr.Jochen Dahm. Jochen wrote a part of the code I used for the inclusive part of the analysis.
I also want to thank the people who helped me during the development of this analysis in many small daily problems. In particular I would like to thank Professor Becks, Dr.Wahlen and Dr.Hamacher for their professional attention.
Among the people who helped me I need to thank :
Ferdinand Hahn, Angelika Drees, Stefan Haider, Patrick Sponholz, Alexander Grefrath, Patrick Langefeld, Frank Glege, Ralf Reinhardt, Matthias Blume, Markus Elsing, Torsten Student, Rolf Lindner, Horand Staek, Abdellah Malek, Uwe Flagmeyer, Klaus Munich. Thanks to Alberto De Min for providing me with pictures and references I needed. Thanks also to Lorenzo Vitale, Alessandro de Angelis, Fabio Cossutti, Olof Barring, Nicol Brummer, Ulrich Schwickerath for their help and attention. Thanks to Alexander Grefrath for having let me discover the beauty of Wuppertal and its region, initially unknown to me. Finally, last but not least, Herzlichen Dank an Frau Verena Offermann. Sie hat mir oft und freundlich geholfen bei vielen kleinen, grossen und täglichen Problemen.

References

[1] C.N.Yang and R.L.Mills, Phys.Rev. **95** (1954) 631

[2] S.L.Glashow, Nucl.Phys.**22** (1961) 579

[3] A.Salam and JC Ward, Phys.Lett.**13** (1964) 168

[4] S.Weinberg, Phys.Rev.Lett., **19** (1967) 1264

[5] J.Goldstone, Nuovo Cimento **19** (1961) 154

[6] P.W.Higgs, Phys.Lett.**12** (1964) 132;
Phys.Rev.Lett **13** (1964) 508

[7] F.J.Hsert et al, Phys.Lett.**46B** (1973) 138

[8] G.Arnison et al., Phys.Lett.**122B** (1983) 103
P.Bagnaia et al., Phys.Lett.**129B** (1983) 130
M.Banner et al., Phys Lett.**122B** (1983) 476

[9] M.Gell-Mann, Phys.Lett. **8** (1964) 214

[10] G.Zweig, CERN preprint TH **401** (1964) (unpubl.)

[11] E.D.Bloom et al., Phys.Rev. **23** (1969) 930
M.Breitenbach et al., Phys.Rev Lett. **23** (1969) 935

[12] V.N.Gribov and L.N.Lipatov, Yad.Fiz.**15** (1972) 781-1218.
Soviet Jour.N.Phys.**15** (1972) 438-675.

[13] M.Y.Han and Y.Nambu, Phys.Rev.139 (1965) 1806.

[14] G.C.Callan and D.Gross, Phys.Rev.Lett. **22** (1969) 156

[15] O.W. Greenberg, Phys.Rev.Lett. **13** (1964) 598

[16] H.J. Behrend et al., Phys.Lett.**144** B (1984) 297

[17] H.D. Politzer, Phys.Rev.Lett.**30** (1973) 1346

[18] Phys.Rew.**50 D** N.3, Particles and Fields (1994)1288-89.

[19] D.J.Gross and F. Wilczek , Phys.Rev D **8** (1973) 3633

[20] R.Brandelik et al., Phys.Lett. **B83** (1979) 261
D.P. Barber et al., Phys Rev.Lett. **43** (1979) 830
C. Berger et al., Phys.Lett. **B86** (1979) 418

[21] X.Banner et al., Phys.Lett. **118B** (1982) 203

[22] G. Arnison et al., Phys.Lett. **123B** (1983) 115

[23] J.Drees, Workshop on QCD,Aachen, June9-13, (1992) Vol.1 pag.106

[24] T.Hebbeker, "Test of Quantum Chromodynamics in Hadronic decays of Z^0 bosons produced in e^+e^- annihilations, Phys.Rep.217 (1992) 19.

[25] X.Artru and G.Mennessier, Nucl.Phys.**B95** (1980) 133.
X.Artru, Phys.Rep.**97** (1983) 147.

[26] V.N.Gribov and L.N.Lipatov, Sov.J.Nucl.Phys.**15** (1972) 438,675.

[27] B.Andersson, G.Gustafson and T.Sjöstrand, Z.Phys.**C6** (1980) 235.

[28] "Z Physics at LEP1", CERN 89-08, pg.164 CERN, Geneva, 1989.

[29] C.Peterson, D.Schlatter, I.Schmitt, P.Zerwas, Phys.Rew.**D27** (1983) 105.

[30] G.Marchesini and B.Webber, Nucl.Phys.**B310** (1988) 461.
G.Marchesini *et al.*,Comput.Phys.Comm.**67**(1992)465.

[31] G.Altarelli and G.Parisi, Nucl.Phys. **B126** (1977) 298.

[32] G.C.Fox and S.Wolfram, Nucl.Phys.**B168** (1980) 285.

[33] Y.L.Dokshitzer, V.A.Dyakonov and S.Troyan, Phys.Rep.**58C** (1980) 269.
A.Bassetto, M.Ciafaloni and G.Marchesini, Phys.Rep.**100C** (1983) 201.

[34] Y.I.Azimov, V.A.Khoze, Y.L.Dokshitzer, S.I.Troyan, Z.Phys.**C27** (1985) 65-72
Y.I.Azimov, V.A.Khoze, Y.L.Dokshitzer, S.I.Troyan, Z.Phys.**C31** (1986) 213-218.

[35] Y.L.Dokshitzer,V.A.Khoze, A.H.Mueller, S.I.Troyan "Basics of perturbative QCD (1991) , Editions Frontieres.

[36] V.S.Fadin, Sov.Jour.N.Phys.**37**(1983) 245.

[37] Z.Coba, H.B.Nielsen, P.Olesen, Nucl.Phys.**B40**(1972) 317.

[38] C.P.Fong and B.Webber, Phys.Lett.**B229** (1989) 289.

[39] Y.I.Azimov, Y.Dokshitzer, V.A.Khoze and S.I.Troyan, Z.Physik.**C27** (1985) 65.
N.Brümmer, Z.Phys.**C66** (1995) 367.

[40] Dokshitzer, Khoze, Troyan, Z.Phys.**C55** (1992) 107.

[41] "Performance of the DELPHI detector", CERN PPE 95-194,21 December 1995.

[42] "DELANA User's guide", DELPHI 89-44/PROG 137, 1989.

[43] Tz.Spassoff "DELPHI DST Content" Version 1.02, DELPHI 95-43 PROG 178

[44] P.Charpentier et al.,"The DELPHI fastbus Data Acquisition System", Proc.Int.Conf.on Compting in High Energy Physics(1991) CHEP91, Tsukuba, Japan,
Y.Watase and F.Abe editors, Univ.Academy Press, Tokio 1991,pg.643

[45] "DELSIM, Delphi event generation and detector simulation"
User's Guide 22 February 1989 DELPHI 89-15 PROG 130

[46] G.Smith, "DELPHI slow controls G64 microcomputers skeleton program"
DELPHI 94-13/DAS-150, rev.1994.

[47] Costruzioni Apparecchiature Elettroniche Nucleari (CAEN) S.p.A.
Via Vetraia, 11 - I-55049 Viareggio, Italy.

[48] DELPHI 94-14 DAS 151 17 October 1994.

[49] R.Brun and J.Zoll, "Zebra User guide", CERN Program Library 1994.

[50] M.Adams et al. Nucl.Instr.Meth. **A 217** (1983) 237.
R.L.McCarthy et al., Nucl.Instr.Meth. **A 248** (1986)69.

[51] P.A.Cherenkov , Phys.Rev 52 (1937) 378-379

[52] I.Frank and I.Tamm, Dokl.Akad.Nauk. SSSR (1938)14-107 (in russian)

[53] P.Baillon et al., NIM **A277** (1989) 338.

[54] E.G.Annassontzis et al., IEEE Trans on .Nucl.Sc. **38** N.2 (1991) 417-423.

[55] Stefan Haider "B_s^0 mixing at the Z resonance determined with the RICH Technique"
Ph.D.Thesis, NIKHEF, Amsterdam, 8 June 1995

[56] Ferdinand Hahn "Inklusive Messung der $K^{\pm}$ und $p\overline{p}$ Produktion in Z^0-Zerfaellen"
Ph.D.Thesis, Universität Wuppertal, WUB-DIS 95-2,February 1995.

[57] DELPHI Collaboration, "Inclusive measurement of the $K^{\pm}$ and $p\overline{p}$ production in Z decays,

CERN/PPE 95-28, March 14, 1995.

[58] J.Seguinot and T.Ypsilantis NIM 142 (1977) 377-391

[59] Proceedings of the Second International Workshop on Ring Imaging Detectors (RICH95),
Uppsala, Sweden, June 12-16 1995, T.Ekelöf ed., North-Holland (1995)
A.Breskin, NIM **A 371** (1996) 116-136.

[60] M.Berggren, "ERA, The RICH alignment software package", DELPHI 89-81/PROG 146 (1989).

[61] M.Dracos, NIM **A 371** (1996) 236-239.

[62] IEEE, Trans. Nucl. Science, Vol.36, N.1, Feb.89, The DELPHI Time Projection Chamber.

[63] Paul Baillon, "Cherenkov Ring Search using a Maximum Likelihood Technique"
CERN EP 84-171 , 21 december 1984

[64] Emile Schyns, "NEWTAG,π, K, p Tagging for Delphi RICHes"
DELPHI 96-103 RICH 89, 1 July 1996

[65] G.V.Borisov "Lifetime Tag of events $Z \to b\bar{b}$" with the DELPHI detector, AABTAG program"
DELPHI 94-125 PROG 208

[66] Jochen Dahm, "Messung der π^+, $K^\pm$, $p\overline{p}$-Produktion
in hadronischen Z^0-Zerfällen", Ph.D.Thesis,
University of Wuppertal, August 1996, WUB-DIS 96-13

[67] N.Brümmer, "Experimental momemtum spectra of identified hadrons at e^+e^- colliders compared to QCD calculations"
Z.Phys.**C** 66, 367-373 (1995).